Efficient Design Strategies for Passive Microwave Components

By
Rambabu Karumudi

A Dissertation Submitted in Partial Fulfillment of the
Requirements for the Degree of

Doctor of Philosophy

in the Department of Electrical & Computer Engineering

We accept this thesis as conforming to the required standard

UNIVERSITY OF VICTORIA

Supervisor: Dr. J.Bornemann

ABSTRACT

The development of modern communication systems is challenged by increasing demands on overall performance and decreasing turn-around times. Therefore, a fast and reliable component design process is at the center of a timely system prototyping concept. This thesis focuses on developing design methodologies for passive microwave components. They are derived from the coupling between various parts of a microwave circuit and take into account the physics of electromagnetic interactions between elements.

A generalized coupling theory is presented which can consider the effects of external fields on the coupling between circuit structures. Different circuit technologies are combined to achieve a microstrip-stripline coupler design with power handling capabilities and small components size. A slot coupler design methodology is presented which uses field averaging concepts to account for coupling through large apertures. A relatively small yet high power waveguide rotary joint design is presented for X-band radar systems. An innovative topology and design concept is demonstrated for filters fabricated in LTCC technology. A theoretical model for signal tapping pads is developed and applied to a novel low pass filter design including capacitive pads and lumped inductors. A broadband equivalent circuit model for electromagnetic band gap structures is presented and its application for a printed circuit GPS antenna is illustrated.

The initial design techniques, methodologies and strategies developed in this thesis are validated by comparison with measurements or other independently obtained results, e.g., from commercially available software packages.

Examiners:

Table of Contents

Bibliography

List of Tables

List of Figures

Acknowledgements

I wish to express my gratitude to my supervisor, Prof. J. Bornemann for his tireless dedication in helping me to achieve the objectives of my career. His caring attitude, both technically and personally, not only contributed to this success, but also to my personal development. The timely completion of my thesis would not have been possible without his support and inspiration. Working with him has been a valuable experience.

I would like to express my acknowledgement to Prof. W.J.R Hoefer, whose presence throughout the tenure of my studies has been of great value. I highly regard his abilities as a scientist and as a teacher.

I sincerely acknowledge the friendship, help and technical discussions of Mr. H.A. (Albie) Thiart, Mr. M.Z. Alam, Mr. A. Tennent, Mr. Seng Yong Yu, Ms. D. Huilian, Mr. Deepak Sarkar, Dr. Poman So, Dr. K.Caputa and Ms. M. Mokhtaari.

Last but not least, acknowledgement is due to all my roommates for making my home away from home pleasurable and memorable.

Dedication

To my Parents

List of Symbols

$\overline{E}$	Electric field
$\overline{H}$	Magnetic field
V	Voltage
I	Current
z_i	Self impedance
y_i	Self admittance
z_m	Mutual impedance
y_m	Mutual admittance
γ	Propagation constant
$[Z]$	Impedance matrix
ε_r	Dielectric constant
λ_g	Guided wavelength
β	Phase constant
ε_0	Dielectric constant of free space
p_e	Electric polarization current
α_e	Electric polarizability of an aperture
p_m	Magnetic polarization current
α_m	Magnetic polarizability of an aperture
$\delta(z)$	Delta (impulse) function
$\overline{J}$	Electric current density
$\overline{M}$	Magnetic current density
μ_0	Permeability of free space
$\overline{e}$	Modal electric field vector
$\overline{h}$	Modal magnetic field vector
W	Width of the stripline
W_m	Width of microstrip line
b	Thickness of stripline
h	Thickness of microstrip line
Z_c	Characteristic impedance of microstrip line
k_c	Cutoff wave number
$\mathrm{Z}_{\mathrm{e/o}}$	Even/Odd mode impedance

Common abbreviations

RF	Radio Frequency
LTCC	Low Temperature Co-fired Ceramics
EBG	Electromagnetic Band Gap
TEM	Transverse Electromagnetic
CAD	Computer Aided Design
MMT	Mode Matching Technique
SIR	Stepped Impedance Resonator
EM	Electromagnetic
MOM	Method of Moments
rpm	Revolutions per minute

Electromagnetic Simulation Software

IE3D	Zeland Software, Inc. (zeland.com)
HFSS	Ansoft Corporation (ansoft.com)
Ansoft Designer	Ansoft Corpoartion (ansoft.com)
MEFiSTO-3D	Faustus Corporation (faustcorp.com)
ADS	Agilent Technologies (agilent.com)
Ensemble	Now part of Ansoft Designer

Chapter-I

1 Introduction

1.1 Motivation

Microwave communication systems require different types of passive and active components. The important passive components are antennas, filters, couplers, multiplexers etc. In passive component design, miniaturization (size) and performance (bandwidth) are the main features to be achieved while keeping the cost of the design as low as possible. These desired features can be achieved by choosing suitable technology and innovative technical designs. Optimal component design is possible by choosing the design techniques that take advantage of the physics of a component. The cost of the microwave component and, subsequently, the cost of the microwave system is decreased by reducing the design cycle of the component.

Over the past decade, many techniques have been developed to reduce the computational effort of numerical methods, e.g. [53]. New algorithms have been devised for improving the optimization process [54]. However, very little effort went into the development of synthesis mechanisms based on physical concepts.

The design of microwave components/antennas in a given time frame is a challenging task for an engineer. In the modern competitive world, the design cycle of a product must be very short. This is not just because of product competition, but also due to competitive intellectual race. The industrial hierarchy of a product design starts with a base design followed by accurate analysis using numerical methods and optimization to meet the required specifications. It is well known that the design of a component based on optimization alone takes huge computer resources and time [55]; sometimes this process might not even converge to a meaningful design at all. Therefore, the development of accurate basic-circuit equivalents for the quick initial design of a microwave product is in high demand.

The motivation of this work is to develop innovative and accurate base models for the synthesis of passive components. The aim is to miniaturize component size and reduce the design cost. These targeted design procedures will aid the RF/wireless/microwave engineer in the initial design of a wide range of passive components.

1.2 Contributions

Electromagnetic interference of external fields on printed circuit boards is a well-known problem in microwave/RF technology [56]. As the demand for high-density packaging increases, so does the necessity of measuring and evaluating the influence of external fields. Modeling techniques for such phenomena have evolved only recently and are mainly based on time-domain approaches and transient analysis [57], [58]. In this thesis, an effective frequency-domain analysis, which accounts for the entire external electromagnetic field is developed.

One of the important aspects of component design is the tradeoff between miniaturization and power handling capability. Although miniaturization has been generally achieved by utilizing microstrip technology, the main application-oriented difference between microstrip and stripline circuits is their power handling capability. By combining the technologies of stripline for main signal path and microstrip line for monitoring purposes, it is possible to attain both miniaturization and power handling capability. A standard proximity coupler at UHF and VHF bands yields relatively large component size due to the required quarter wavelength coupling section [14]. In this thesis, a new design is proposed, which reduces the component size to less than one fifth of a wavelength. Coupling between the stripline and the microstrip line is achieved through apertures in the common ground plane.

Coupling between two waveguides play an important role in the design of directional couplers and filters. An initial waveguide coupler design usually involves Bethe's coupling theory [4], [23]. However, this approach is applicable only for small apertures and only for aperture shapes with well-known expressions for their electric and magnetic polarizabilities. One of the important apertures in coupler, filter and antenna feed systems design is the cross slot [16], [17], [18]. Its analysis and initial design, however, is hampered by the lack of expressions for its electric and magnetic polarizabilities. In this thesis, a novel analysis and initial design concept for cross-slot couplers is presented. To facilitate a speedy design process, the measured data for the polarizabilities of the cross-slot have been curve fitted by a least squares method, and large cross-slots are analyzed by field averaging. This approach includes the effects of the orientation of the slot and allows coupling between asymmetric waveguides.

In tracking radar applications, rotary joints form the link between the stationary and movable parts of the microwave communication system. Their essential characteristics are high-power carrying capability, low insertion loss and good impedance matching [25]. In this thesis, a new design for single channel waveguide rotary joints for high power applications is presented. In order to obtain correct signal phase conditions along the ring and at the same time, reduce the diameter of the rotary joint, tapered ridged waveguide sections are introduced.

RF and microwave system-on-chip modules for wireless communication are increasingly fabricated in low temperature co-fired ceramic (LTCC) technology due to the possible scope of miniaturization [30]. In this thesis, a new LTCC filter configuration, which improves the stopband behavior, is proposed. Attenuation poles on either side of the passband can be achieved through capacitively coupled strips with two stripline impedance resonators. The simplified analysis introduced in this thesis permits the design engineer to perform a fast initial design of this class of LTCC filters.

Microstrip circuits invariably incorporate transmission line discontinuities of one type or another. The effect of these discontinuities is predominant at microwave frequencies [12].

In high-density RF circuits, it is important to estimate the influence of the discontinuities so that RF noise can be controlled. In this thesis, analytical expressions for the capacitance of signal tapping pads are derived using a quasi-static analysis. A new lowpass filter design is proposed, which combines the signal tapping pads with lumped inductors.

Recent advances and applications of electromagnetic bandgap (EBG) structures have proven that the excitation of surface waves can be considerably reduced [40], [44]. Especially with respect to patch antennas, it is demonstrated that their performance can be improved by utilizing additional printed periodic structures, which create a stopband within the particular frequency range of operation [43]. In this thesis, equivalent-circuit methods are developed in order to quickly design EBG structures for desired pass- and stopbands.

1.3 Overview of the thesis

After this introduction, Chapter 2 will give a brief description of coupling analysis for planar transmission lines in the presence of external RF fields, and coupling between various forms of waveguides and/or transmission lines.

Chapter 3 presents a novel stripline to microstrip line coupler design. In this design, coupling is achieved through apertures in the common ground plane. This design yields miniaturization and relatively high power handling capability.

Chapter 4 will describe analysis and design techniques for rectangular waveguide cross-slot couplers. Coupling due to large apertures is calculated using field averaging over individual apertures. All scattering parameters for the coupler are presented in terms of simple analytical expressions.

Chapter 5 presents the design of a single channel waveguide rotary joint for high power applications. In this design, miniaturization is achieved through the introduction of tapered ridges into the center waveguide rings.

Chapter 6 proposes a new LTCC filter configuration, which improves the stopband behavior of previous designs. Moreover, a simplified analysis technique is presented to aid filter engineers in the initial design of capacitively coupled LTCC resonators.

Chapter 7 presents the analytical solution for calculating the capacitance of signal tapping pads in the RF circuits. It also presents a novel lowpass filter design using signal tapping pads and lumped inductors.

Chapter 8 presents the improved equivalent circuit model to the analysis of electromagnetic bandgap structures. Few examples are presented to validate the proposed model.

Chapter 9 presents the conclusions and future research directions for the development of design methods for various miniaturized passive microwave components.

Throughout the thesis, the initial design techniques are validated by comparison with results obtained from measurements or independently developed or commercially available software packages.

Chapter-II

2 Coupling in Microwave Circuits

Introduction

Electromagnetic coupling plays a very important role in the design and development of microwave circuits and integrated antenna arrays. Proper characterization and analysis of this phenomenon will lead to quick and accurate design. Microwave circuits may contain planar transmission-line or waveguide components. Analysis of coupling between these structures is the key for good design. Analysis for coupling between planar components in the presence of external RF fields is presented in section 2.1. The coupling analysis for various waveguide circuits is presented in section 2.2.

2.1 Coupled Lines in the Presence of External RF Fields

In modern high-density microwave/RF circuits, the necessity of taking into account the fields generated in a circuit becomes greater as the demand for high-density packaging increases. In this case, the electromagnetic fields may affect other circuits so that the required performance of the circuit may be unsatisfactory. The formulation for the induced current in the transmission line excited by external electromagnetic fields is based on Maxwell's equations. Here, the mode of propagation in the line can be approximated as a transverse-electromagnetic (TEM) mode or at least as a quasi-TEM mode. Therefore, line voltage and line current can be defined as being similar to those of static fields in the transverse plane. In case of symmetric lines, the coupling can be estimated by using a technique known as even/odd mode analysis whereas for asymmetric lines, it is C/Π-mode technique [1].

2.1.1 Formulation

Fig. 2.1 shows the generalized proximity coupled lines. The external fields $\overline{E}$ and $\overline{H}$ can be regarded as interference from the near by circuit. The interfering fields can be calculated from currents (via potential functions) flowing on a nearby circuit. In this section a generalized coupling theory is proposed to estimate the influence of external interference.

The behavior of two coupled lines in the presence of external electromagnetic fields can be described by the set of equations:

$$-\frac{dV_1}{dx} = z_1\left[I_1 - \int_{p_1} \overline{H} \cdot \overline{dl}\right] + z_m I_2 \tag{2.1}$$

$$-\frac{dV_2}{dx} = z_2\left[I_2 - \int_{p_2} \overline{H} \cdot \overline{dl}\right] + z_m I_1 \tag{2.2}$$

$$-\frac{dI_1}{dx} = y_1\left[V_1 + \int_0^d \overline{E} \cdot \overline{dl}\right] + y_m V_2 \tag{2.3}$$

$$-\frac{dI_2}{dx} = y_2\left[V_2 + \int_0^d \overline{E} \cdot \overline{dl}\right] + y_m V_1 \tag{2.4}$$

where $z_j(j=1,2)$ and $y_j(j=1,2)$ are self-impedance and admittance per unit length of the line. z_m, y_m are mutual impedance and admittance per unit length. Note that the coupling between the lines, which is represented by z_m, y_m, is not affected by the interfering fields. For vanishing external fields, (2.1) to (2.4) reduce to the well-known coupled line equations [1].

Eliminating I_1 and I_2 from (2.1) to (2.4) gives the following set of coupled equations for voltages V_1 and V_2:

$$\frac{d^2V_1}{dx^2} - a_1V_1 - b_1V_2 - \left((z_m y_2 + y_1 z_1) \int_0^d \overline{E} \cdot \overline{dy} + z_1 \int_{p_1} \frac{d\overline{H}}{dx} \cdot \overline{dl} \right) = 0 \tag{2.5}$$

$$\frac{d^2V_2}{dx^2} - a_2V_2 - b_2V_1 - \left((z_m y_1 + y_2 z_2) \int_0^d \overline{E} \cdot \overline{dy} + z_2 \int_{p_2} \frac{d\overline{H}}{dx} \cdot \overline{dl} \right) = 0 \tag{2.6}$$

where

$a_1 = y_1 z_1 + z_m y_m$; $b_1 = z_1 y_m + z_m y_2$; $a_2 = y_2 z_2 + z_m y_m$; $b_2 = y_1 z_m + z_2 y_m$

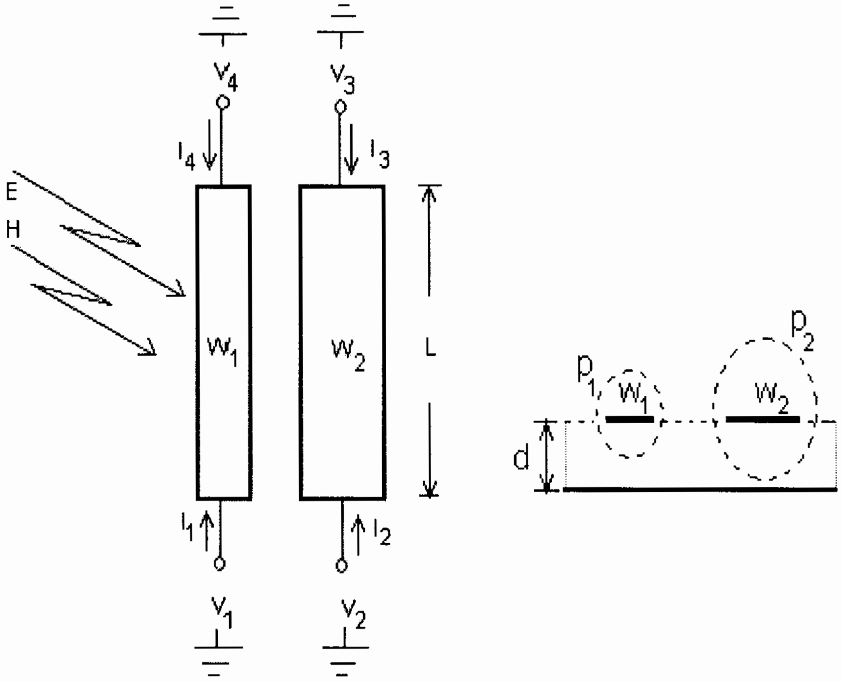

Figure 2.1 Schematic of the coupled lines in the presence of external RF fields

Using (2.5) and (2.6) we can write

$$\frac{d^4V_2}{dx^4} - (a_2 + a_1)\frac{d^2V_2}{dx^2} + (a_1a_2 - b_1b_2)V_2 + (a_1c_2 - b_2c_1) = 0 \tag{2.7}$$

where $c_1 = \left(\left(z_m y_2 + y_1 z_1\right) \int_0^d \overline{E} \cdot \overline{dy} + z_1 \int_{p_1} \frac{d\overline{H}}{dx} \cdot \overline{dl} \right)$;

$$c_2 = \left(\left(z_m y_1 + y_2 z_2\right) \int_0^d \overline{E} \cdot \overline{dy} + z_2 \int_{p_2} \frac{d\overline{H}}{dx} \cdot \overline{dl} \right)$$

By assuming a variation of type $e^{-\gamma x}$ for the voltages $V_1, V_2, \overline{E}$ and $\overline{H}$, we can write the characteristic equation using (2.7)

$$\gamma^4 - \left(a_1 + a_2\right)\gamma^2 + a_1\left(a_2 + c_2\right) - b_2\left(b_1 + c_1\right) = 0 \qquad (2.8)$$

The four solutions to equation (2.8)

$$\gamma_{c,\pi}^2 = \frac{a_1 + a_2}{2} \pm \frac{1}{2}\sqrt{\left(a_1 + a_2\right)^2 - 4\left(a_1\left(a_2 + c_2\right) - b_2\left(b_1 + c_1\right)\right)} \qquad (2.9)$$

represent the forward and backward traveling waves of C and Π modes for asymmetrical coupled lines with propagation constants γ_c and γ_Π, respectively. For symmetrical lines these modes become even and odd modes.

The relationship between the voltages on the two lines for each one of these waves may be determined from (2.5) and (2.6)

$$\frac{d^2 V_1}{dx^2} - a_1 V_1 - b_1 V_2 - c_1 = 0 \qquad (2.10)$$

$$\frac{d^2 V_2}{dx^2} - a_2 V_2 - b_2 V_1 - c_2 = 0 \qquad (2.11)$$

so that the voltage ratio can be written in terms of the propagation constant (2.9)

$$\frac{V_2}{V_1} = \frac{c_2\left(\gamma^2 - a_1\right) + b_2 c_1}{c_1\left(\gamma^2 - a_2\right) + b_1 c_2} \tag{2.12}$$

Let $\frac{V_2}{V_1} = R_c\{\gamma = \gamma_c\}, R_\pi\{\gamma = \gamma_\pi\}$, the general solutions for the voltages on the two lines in terms of all four waves are given by

$$V_1 = A_1 e^{-\gamma_c x} + A_2 e^{\gamma_c x} + A_3 e^{-\gamma_\pi x} + A_4 e^{\gamma_\pi x} \tag{2.13}$$

$$V_2 = R_c A_1 e^{-\gamma_c x} + R_c A_2 e^{\gamma_c x} + R_\pi A_3 e^{-\gamma_\pi x} + R_\pi A_4 e^{\gamma_\pi x} \tag{2.14}$$

Substitution of (2.13), (2.14) into (2.1), (2.2) and solving for port currents I_1, I_2 yields

$$I_{c2} = \frac{\gamma_c\left(z_m - R_c z_1\right)}{R_c\left(z_m^2 - z_1 z_2\right)} R_c A_1 e^{-\gamma_c x} - \frac{\gamma_c\left(z_m - R_c z_1\right)}{R_c\left(z_m^2 - z_1 z_2\right)} R_c A_2 e^{\gamma_c x} + \frac{z_1 z_m \int_{p_1} \overline{H} \cdot \overline{dl} - z_2 z_1 \int_{p_2} \overline{H} \cdot \overline{dl}}{z_m^2 - z_1 z_2} \tag{2.15}$$

$$I_{c1} = \frac{\gamma_c\left(z_2 - R_c z_m\right)}{\left(z_1 z_2 - z_m^2\right)} A_1 e^{-\gamma_c x} - \frac{\gamma_c\left(z_2 - R_c z_m\right)}{\left(z_1 z_2 - z_m^2\right)} A_2 e^{\gamma_c x} + \frac{z_1 z_2 \int_{p_1} \overline{H} \cdot \overline{dl} - z_2 z_m \int_{p_2} \overline{H} \cdot \overline{dl}}{z_1 z_2 - z_m^2} \tag{2.16}$$

$$I_{\pi 2} = \frac{\gamma_\pi\left(z_m - R_\pi z_1\right)}{R_\pi\left(z_m^2 - z_1 z_2\right)} R_\pi A_3 e^{-\gamma_\pi x} - \frac{\gamma_\pi\left(z_m - R_\pi z_1\right)}{R_\pi\left(z_m^2 - z_1 z_2\right)} R_\pi A_4 e^{\gamma_\pi x} + \frac{z_1 z_m \int_{p_1} \overline{H} \cdot \overline{dl} - z_2 z_1 \int_{p_2} \overline{H} \cdot \overline{dl}}{z_m^2 - z_1 z_2} \tag{2.17}$$

$$I_{\pi 1} = \frac{\gamma_\pi\left(z_2 - R_\pi z_m\right)}{\left(z_1 z_2 - z_m^2\right)} A_3 e^{-\gamma_\pi x} - \frac{\gamma_\pi\left(z_2 - R_\pi z_m\right)}{\left(z_1 z_2 - z_m^2\right)} A_4 e^{\gamma_\pi x} + \frac{z_1 z_2 \int_{p_1} \overline{H} \cdot \overline{dl} - z_2 z_m \int_{p_2} \overline{H} \cdot \overline{dl}}{z_1 z_2 - z_m^2} \tag{2.18}$$

Equations (2.15) - (2.18) can be rearranged as follows

$$i_{c1} = I_{c1} - I_{s1} = Y_{c1} A_1 e^{-\gamma_c x} - Y_{c1} A_2 e^{\gamma_c x} \tag{2.19}$$

$$i_{c2} = I_{c2} - I_{s2} = Y_{c2}R_cA_1e^{-\gamma_c x} - Y_{c2}R_cA_2e^{\gamma_c x} \tag{2.20}$$

$$i_{\pi 1} = I_{\pi 1} - I_{s1} = Y_{\pi 1}A_3e^{-\gamma_\pi x} - Y_{\pi 1}A_4e^{\gamma_\pi x} \tag{2.21}$$

$$i_{\pi 2} = I_{\pi 2} - I_{s2} = Y_{\pi 2}R_\pi A_3e^{-\gamma_\pi x} - Y_{\pi 2}R_\pi A_4e^{\gamma_\pi x} \tag{2.22}$$

where

$$Y_{c1} = \frac{\gamma_c\left(z_2 - R_c z_m\right)}{z_1 z_2 - z_m^2}\ ;\ Y_{c2} = \frac{\gamma_c\left(z_m - R_c z_1\right)}{R_c\left(z_m^2 - z_1 z_2\right)};$$

$$Y_{\pi 1} = \frac{\gamma_\pi\left(z_2 - R_\pi z_m\right)}{z_1 z_2 - z_m^2};\ Y_{\pi 2} = \frac{\gamma_\pi\left(z_m - R_\pi z_1\right)}{R_\pi\left(z_m^2 - z_1 z_2\right)}$$

$$I_{s1} = \frac{z_1 z_2 \int_{p_1} \overline{H}\cdot\overline{dl} - z_2 z_m \int_{p_2} \overline{H}\cdot\overline{dl}}{z_1 z_2 - z_m^2}$$

$$I_{s2} = \frac{z_1 z_m \int_{p_1} \overline{H}\cdot\overline{dl} - z_2 z_1 \int_{p_2} \overline{H}\cdot\overline{dl}}{z_m^2 - z_1 z_2}$$

The impedance matrix for the four-port is found by solving for port voltages in terms of port currents. Since the port voltages and currents are given

$$\begin{bmatrix} V_1 \\ V_2 \\ V_3 \\ V_4 \end{bmatrix} = \begin{bmatrix} 1 & 1 & 1 & 1 \\ R_c & R_c & R_\pi & R_\pi \\ R_c e^{-\gamma_c l} & R_c e^{\gamma_c l} & R_\pi e^{-\gamma_\pi l} & R_\pi e^{\gamma_\pi l} \\ e^{-\gamma_c l} & e^{\gamma_c l} & e^{-\gamma_\pi l} & e^{\gamma_\pi l} \end{bmatrix} \begin{bmatrix} A_1 \\ A_2 \\ A_3 \\ A_4 \end{bmatrix} \tag{2.23}$$

$$\begin{bmatrix} i_1 \\ i_2 \\ -i_3 \\ -i_4 \end{bmatrix} = \begin{bmatrix} Y_{c1} & -Y_{c1} & Y_{\pi 1} & -Y_{\pi 1} \\ R_c Y_{c2} & -R_c Y_{c2} & R_\pi Y_{\pi 2} & -R_\pi Y_{\pi 2} \\ R_c Y_{c2} e^{-\gamma_c l} & -R_c Y_{c2} e^{\gamma_c l} & R_\pi Y_{\pi 2} e^{-\gamma_\pi l} & -R_\pi Y_{\pi 2} e^{\gamma_\pi l} \\ Y_{c1} e^{-\gamma_c l} & -Y_{c1} e^{\gamma_c l} & Y_{\pi 1} e^{-\gamma_\pi l} & -Y_{\pi 1} e^{\gamma_\pi l} \end{bmatrix} \begin{bmatrix} A_1 \\ A_2 \\ A_3 \\ A_4 \end{bmatrix} \tag{2.24}$$

the impedance matrix follows as

$$[Z]=\begin{bmatrix} 1 & 1 & 1 & 1 \\ R_c & R_c & R_\pi & R_\pi \\ R_c e^{-\gamma_c l} & R_c e^{\gamma_c l} & R_\pi e^{-\gamma_\pi l} & R_\pi e^{\gamma_\pi l} \\ e^{-\gamma_c l} & e^{\gamma_c l} & e^{-\gamma_\pi l} & e^{\gamma_\pi l} \end{bmatrix} \begin{bmatrix} Y_{c1} & -Y_{c1} & Y_{\pi 1} & -Y_{\pi 1} \\ R_c Y_{c2} & -R_c Y_{c2} & R_\pi Y_{\pi 2} & -R_\pi Y_{\pi 2} \\ R_c Y_{c2} e^{-\gamma_c l} & -R_c Y_{c2} e^{-\gamma_c l} & R_\pi Y_{\pi 2} e^{-\gamma_\pi l} & -R_\pi Y_{\pi 2} e^{-\gamma_\pi l} \\ Y_{c1} e^{-\gamma_c l} & -Y_{c1} e^{-\gamma_c l} & Y_{\pi 1} e^{-\gamma_\pi l} & -Y_{\pi 1} e^{-\gamma_\pi l} \end{bmatrix}^{-1} \qquad (2.25)$$

The above derived Z-matrix can be used to derive the coupling between two asymmetrical coupled lines in the presence of external RF fields. Given the line impedance of the connected lines, the four-port scattering matrix [S] of a coupled line section can be deduced from the impedance matrix, e.g. [2].

To validate the proposed model for coupling in the presence of external field, we consider an asymmetrical coupled line of dimensions shown in Fig. 2.1: $W_1 = 0.8mm$, $W_2 = 1.2mm$, $d = 0.8mm$, dielectric constant $\varepsilon_r = 7.5$, gap between the lines $s = 0.4mm$. For simplicity, external fields are assumed to arrive from the topside of the board.

Fig. 2.2 shows the coupling from port 1 to port 3 without external fields. Good agreement with commercial field solver IE3D is observed. Upon arrival of the external field, the relative field strengths at the ports change as shown in Fig. 2.3 to Fig. 2.7. While the field strength at port 3 remains relatively unaffected compared to Fig. 2.2, the strengths at port 1 and 2 increase with stronger external RF fields, thus demonstrating their influence on the circuit. As the external RF field increases to 200 mV/mm, its added power appears as gain at the circuit ports (c.f. Fig. 2.7). Note that the frequencies of the external field and that of the circuit are assumed identical here. RF noise at other frequencies can be considered by incorporating the respective distributions into (2.1) to (2.4).

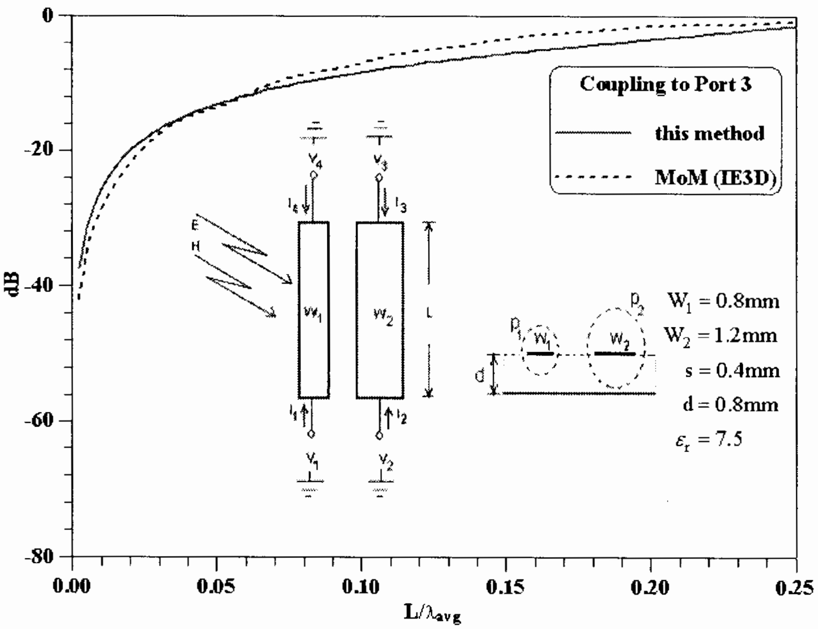

Figure 2.2 Coupling to port 3 without external fields and comparison with the Method of Moments (MOM)

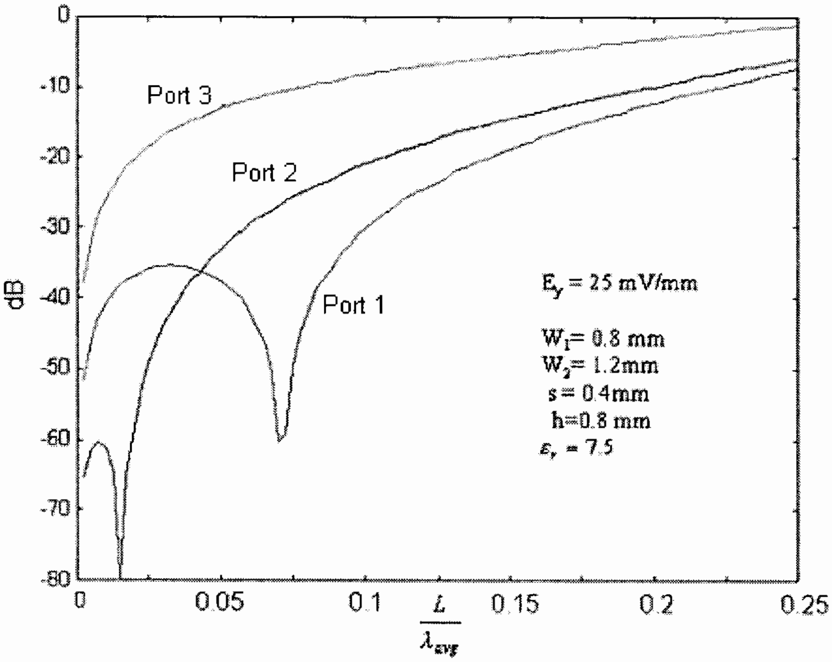

Figure 2.3 Relative signal strength at ports 1, 2 and 3 in the presence of external fields: 25 mV/mm

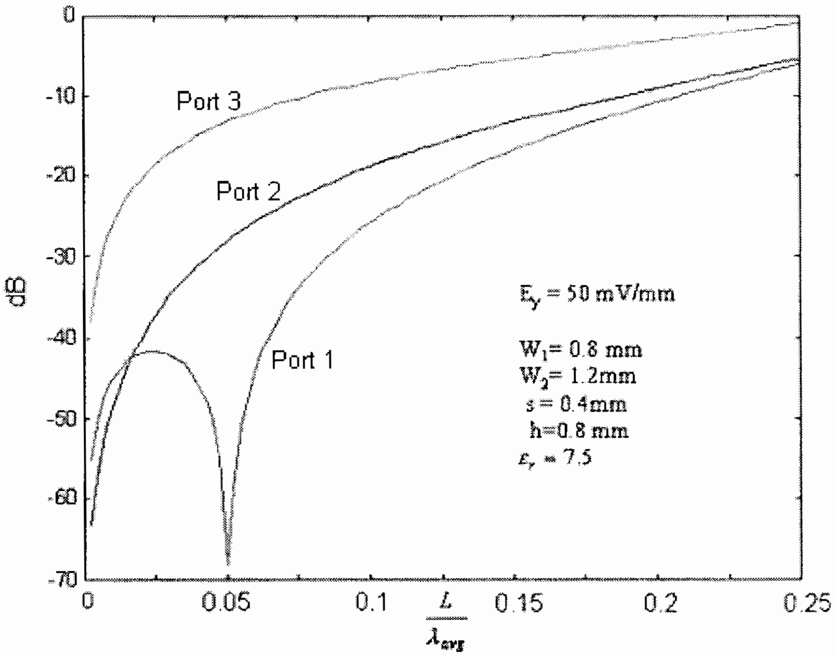

Figure 2.4 Relative signal strength at ports 1, 2 and 3 in the presence of external fields: 50 mV/mm

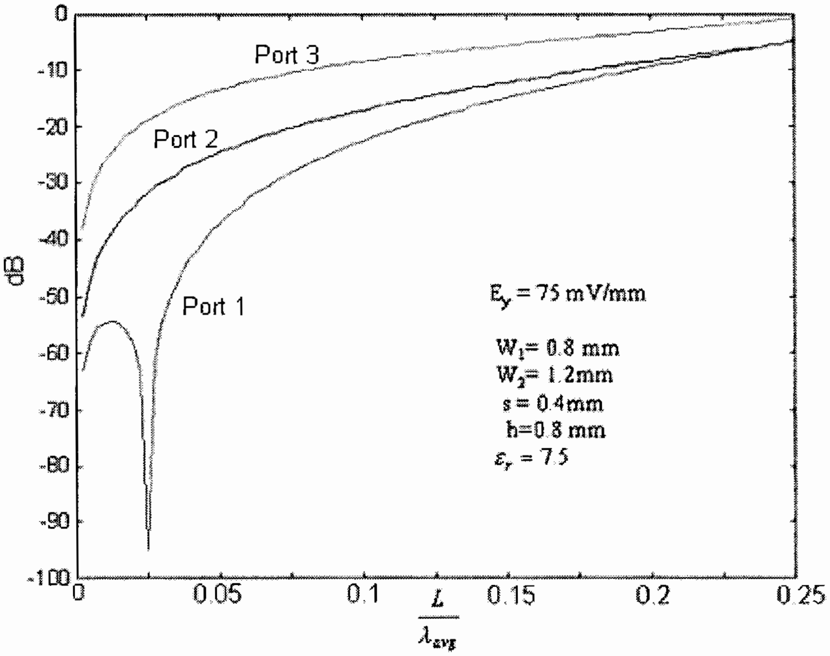

Figure 2.5 Relative signal strength at ports 1, 2 and 3 in the presence of external fields: 75 mV/mm

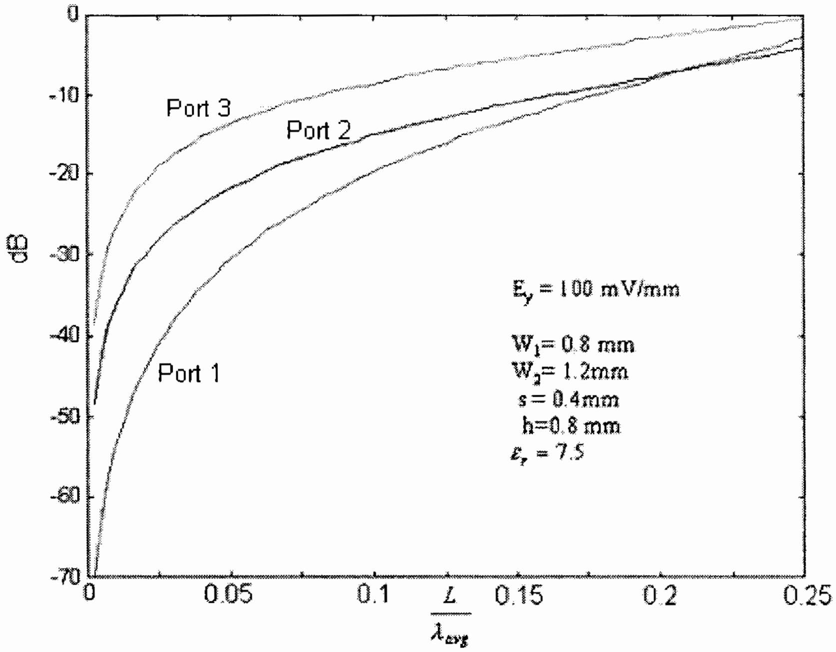

Figure 2.6 Relative signal strength at ports 1, 2 and 3 in the presence of external fields: 100 mV/mm

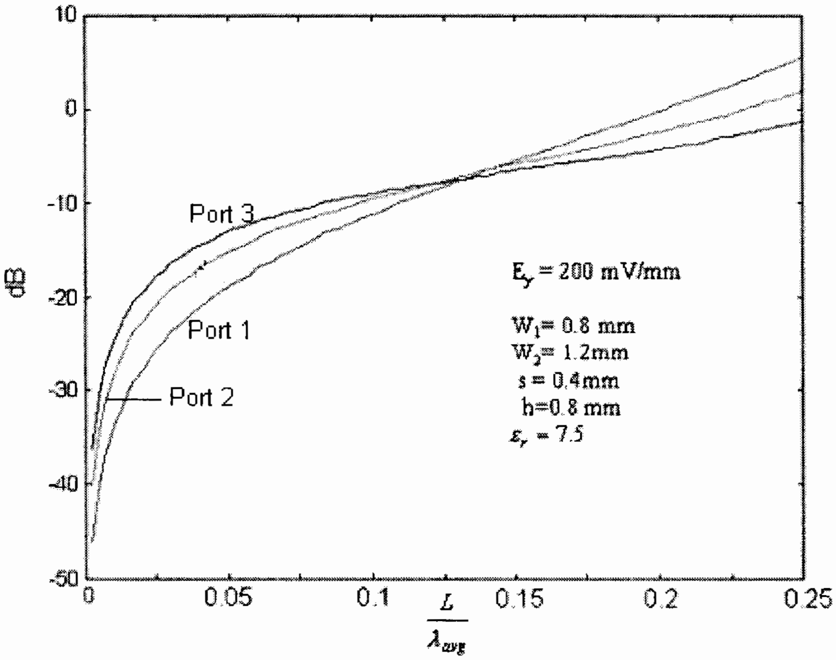

Figure 2.7 Relative signal strength at ports 1, 2 and 3 in the presence of external fields: 200 mV/mm

2.2 Aperture Coupling Theory

Aperture coupling theory assumes a uniform field over a small aperture and infinitesimally thin shielding between the coupled regions. A simple analysis technique for calculating the coupling between two single port sections was proposed by Wheeler [3}. In this approach the field coupling or polarizabilities of any aperture have been expressed in terms of an effective volume. The coupling coefficient (k) between resonant cavities and coupling reactance (x) between two transmission lines and loading power factor (p) between cavity and transmission line are expressed in terms of a volume ratio. To this end, each field region and each coupling aperture will be evaluated in terms of its effective volume or area with reference to the kind of field that is instrumental in effecting a certain amount of coupling. In calculating the coupling coefficient, the rule of "one half" plays a critical role, although it applies strictly to a symmetrical structure only. The rule of "one half" says that the field intensity at the center of the coupling aperture will average the field intensities in the regions on either side of the aperture.

2.2.1 Wheeler's Approach

(a) Coupling between two identical resonant cavities

Fig. 2.8 shows the principle of coupling between two resonant cavities. They are separated by a common wall and are coupled through a hole in the wall. The coupling coefficient (k) is defined as

$$k = \frac{1}{4}\frac{V_c}{V} \tag{2.26}$$

V - Effective volume of each cavity

V_c - Effective volume of the coupling aperture

The factor ¼ is introduced based on the concept of the "rule of one half".

The effective volume of a resonant cavity is defined as the volume, which would contain the same amount of energy, either electric or magnetic, depending on the coupling field, if filled with uniform intensity equal to the reference field. The reference field is the field at the location of the aperture, when the aperture is not opened. The effective volume of the coupling aperture is $4/\pi$ times the circumscribed volume of the aperture.

(b) Coupling between two identical waveguides

The waveguides may be coupled in various ways through a hole in a common wall. The amount of coupling between the waveguides may be expressed in terms of the normalized reactance (x) across the waveguide depending on the type of coupling.

$$x = \frac{1}{4}\frac{V_c}{V} \tag{2.27}$$

V_c - Effective volume of the coupling aperture

V- Effective volume of the waveguide

The effective volume of the waveguide will be evaluated like the resonant cavity case, with radian length in the waveguide. So the length of the region is $\left(\frac{1}{2\pi}\right)\lambda_g$

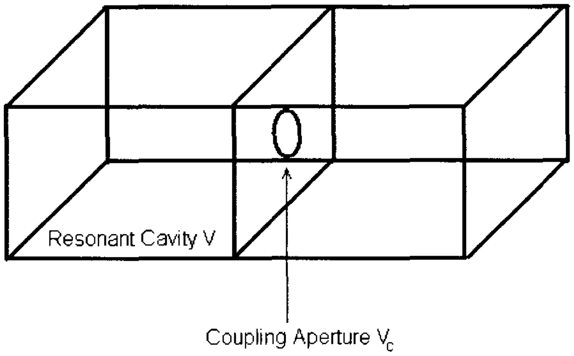

Figure 2.8 Coupling between two resonators

(c) Coupling between resonant cavity and waveguide

The evaluation of the coupling between two identical cavities or waveguides is simplified by symmetry. This symmetry is lost in the coupling between a resonant cavity and a waveguide. Therefore, this coupling is usually expressed by the loading power factor (p), which can be represented by

$$p = kx \tag{2.28}$$

The resonator and aperture can be imaged to form two identical waveguides coupled by the same aperture. This symmetric arrangement is used for defining and evaluating a *coupling coefficient* (k).

Similarly, the waveguide and aperture can be imaged to form two like waveguides coupled by the same aperture, but the symmetric arrangement is used for defining and evaluating the *normalized reactance* (x). With the coupling coefficient and normalized reactance so defined, their product becomes equal to the loading power factor.

As soon as the coupled media are distinctively different, Wheeler's approach, which is accurate for symmetric structures only, will fail. Therefore, a modified theory is presented in the next section, which will describe the general procedure for the coupling analysis of single, and multiple apertures between different line media.

2.2.2 Coupling Between Two Different Transmission Lines

(a) Coupling through a single aperture

Two transmission lines with symmetric or asymmetric geometry may be coupled through an aperture. Let the input power be fed to line 1 and coupled to line 2. Let the dielectric constant of the medium in line 1 and line 2 be ε_{r1} and ε_{r2}. The propagation constant of the lines are β_1 and β_2, respectively. The coupled power from line 1 into line 2, both in forward and backward direction, can be calculated using Bethe's small coupling theory [4]. Although Bethe's theory has been shown to neglect diffracted fields in the immediate vicinity of the aperture [59], the distant fields are unaffected. Therefore, Bethe's coupling theory can be usually applied in RF/Microwave circuitry. The incident normal electric and tangential magnetic fields at the center of the aperture are crucial in calculating the coupled fields. The fields scattered back into line1 by the aperture can be estimated by the small-hole coupling theory.

Let $\overline{E}_1$ and $\overline{H}_1$ be the normal electric and tangential magnetic fields at the center of the coupling aperture in the line 1. The electric and magnetic polarization currents into line 2 can be represented as [2]

$$\overline{P}_e = \varepsilon \alpha_e \frac{\int\!\!\int_s \overline{E}_1 ds}{\int\!\!\int_s ds} \tag{2.29}$$

$$\varepsilon = \varepsilon_0 \left(\frac{2\varepsilon_{r1}\varepsilon_{r2}}{\varepsilon_{r1} + \varepsilon_{r2}} \right)$$

$$\overline{P}_m = -\alpha_m \frac{\int\!\!\int_s \overline{H}_1 ds}{\int\!\!\int_s ds} \tag{2.30}$$

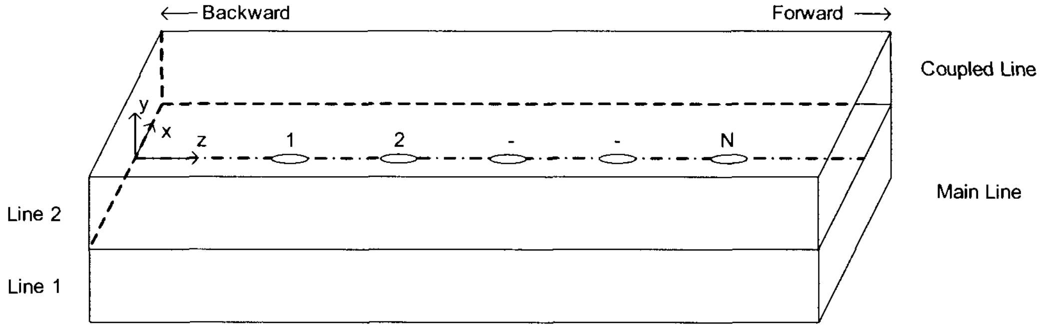

Figure 2.9 Coupling between two waveguides

The polarizability of an aperture can be defined as the quotient of the equivalent dipole moment over the incident field intensity [10]. It depends on the size and shape of the aperture. Using Maxwell's equations, one can relate $\overline{P}_e$ and $\overline{P}_m$ to the electric and magnetic current sources $\overline{J}$ and $\overline{M}$.

$$\overline{J} = j\omega\overline{P}_e \tag{2.31}$$

$$\overline{M} = j\omega\mu_0\overline{P}_m \tag{2.32}$$

(i) Calculation of coupling coefficients

Let the fields radiated by the electric and magnetic current sources be represented in terms of the modal field vectors $\overline{e}_2$, $\overline{h}_2$ of the line. Then the total coupled fields can be represented as

$$\overline{E}^+ = \left(C_{ec}^+ + C_{mc}^+\right)\overline{e}_2 e^{-j\beta_2 z} \qquad z > 0 \tag{2.33}$$

$$\overline{H}^+ = \left(C_{ec}^+ + C_{mc}^+\right)\overline{h}_2 e^{-j\beta_2 z} \qquad z > 0 \tag{2.34}$$

$$\overline{E}^- = \left(C_{ec}^- + C_{mc}^-\right)\overline{e}_2 e^{-j\beta_2 z} \qquad z < 0 \tag{2.35}$$

$$\overline{H}^- = -\left(C_{ec}^- + C_{mc}^-\right)\overline{h}_2 e^{-j\beta_2 z} \qquad z < 0 \tag{2.36}$$

where z is the direction of propagation.

$C_{ec,mc}^+$, $C_{ec,mc}^-$ are the coupling coefficients due to electric and magnetic current sources in forward and backward directions.

Let the fields coupled due to the electric current source be represented by

$$\overline{E}_c = C_{ec}^{\pm}\overline{e}_2 e^{\mp j\beta_2 z} \tag{2.37}$$

$$\overline{H}_c = \pm C_{ec}^{\pm}\overline{h}_2 e^{\mp j\beta_2 z} \tag{2.38}$$

Let $\overline{E}_2$, $\overline{H}_2$ be the source-free fields, which are traveling in −z direction.

$$\overline{E}_2 = \overline{e}_2 e^{j\beta_2 z} \tag{2.39}$$

$$\overline{H}_2 = -\overline{h}_2 e^{j\beta_2 z} \tag{2.40}$$

By applying the reciprocity theorem, we can show that

$$\int\!\!\int_s \left[\left(\overline{E}_c \times \overline{H}_2\right) - \left(\overline{E}_2 \times \overline{H}_c\right)\right] \cdot \overline{ds} = \int\!\!\int\!\!\int_v \overline{E}_2 \cdot \overline{J}\delta(y)dv \tag{2.41}$$

where the surface current density in the *xz* plane is located at *y*=0.

The volume of integration is between the waveguide walls and the transverse cross-section planes z_1, z_2. These planes can be anywhere on either side of the coupling aperture, e.g. in forward and backward direction (c.f. Fig. 2.9). The tangential electric field on the waveguide walls is zero. So (2.41) can be written as

$$\int\!\!\int_{z_1, z_2} \left[\left(\overline{E}_c \times \overline{H}_2\right) - \left(\overline{E}_2 \times \overline{H}_c\right)\right] \cdot \bar{z}dz = \int\!\!\int\!\!\int_v \overline{E}_2 \cdot \overline{J}\delta(y)dv \tag{2.42}$$

Equation (2.42) can be expanded using (2.37-2.40); then

$$C_{ec}^{+} = -\frac{\int\!\!\int\!\!\int_v \overline{e}_2 \cdot \overline{J}\delta(y)dv}{2\int\!\!\int_{s_1} \left(\overline{e}_2 \times \overline{h}_2\right) \cdot \hat{z}ds_0} = -\frac{1}{P_{l2}} \int\!\!\int\!\!\int_v \overline{e}_2 . \overline{J}\delta(y)dv \tag{2.43}$$

where P_{l2} is the normalized power flow in line 2.

Similarly, the coupling coefficient in the –z direction can be calculated.

$$C_{ec}^{-} = -\frac{1}{P_{l2}} \iiint_{v} \bar{e}_2 \cdot \bar{J}\delta(y)dv \tag{2.44}$$

The coupling due to the magnetic current source follows analogously.

$$C_{mc}^{+} = -\frac{1}{P_{l2}} \iiint_{v} \bar{h}_2 \cdot \bar{M}\delta(y)dv \tag{2.45}$$

$$C_{mc}^{-} = \frac{1}{P_{l2}} \iiint_{v} \bar{h}_2 \cdot \bar{M}\delta(y)dv \tag{2.46}$$

(ii) Scattered fields into line1

The normal displacement fields and tangential magnetic fields are continuous on the aperture.

$$\varepsilon_{r1}\bar{E}_{l1} = \varepsilon_{r2}\bar{E}_{l2} \tag{2.47}$$

$$\bar{H}_{l1} = \bar{H}_{l2} \tag{2.48}$$

The source currents into line 1 can be written as

$$\bar{J}_s = -\frac{\varepsilon_{r1}}{\varepsilon_{r2}}\bar{J} \tag{2.49}$$

$$\bar{M}_s = -\bar{M} \tag{2.50}$$

The scattered fields can be represented in terms of the modal vectors $\overline{e}_1, \overline{h}_1$ of line 1

$$\overline{E}_s^+ = \left(S_{ec}^+ + S_{mc}^+\right)\overline{e}_1 e^{-j\beta_1 z} \tag{2.51}$$

$$\overline{H}_s^+ = \left(S_{ec}^+ + S_{mc}^+\right)\overline{h}_1 e^{-j\beta_1 z} \tag{2.52}$$

$$\overline{E}_s^- = \left(S_{ec}^- + S_{mc}^-\right)\overline{e}_1 e^{+j\beta_1 z} \tag{2.53}$$

$$\overline{H}_s^- = -\left(S_{ec}^- + S_{mc}^-\right)\overline{h}_1 e^{+j\beta_1 z} \tag{2.54}$$

and the scattered coefficients can be written as

$$S_{ec}^+ = \frac{\varepsilon_{r1}}{\varepsilon_{r2} P_{l1}} \iiint_v \overline{e}_1 \cdot \overline{J} dv \tag{2.55}$$

$$S_{ec}^- = \frac{\varepsilon_{r1}}{\varepsilon_{r2} P_{l1}} \iiint_v \overline{e}_1 \cdot \overline{J} dv \tag{2.56}$$

$$S_{mc}^+ = \frac{1}{P_{l1}} \iiint_v \overline{h}_1 \cdot \overline{M} dv \tag{2.57}$$

$$S_{ec}^+ = -\frac{1}{P_{l1}} \iiint_v \overline{h}_1 \cdot \overline{M} dv \tag{2.58}$$

$$\text{and} \quad P_{l1} = 2\int_{s_1} \left(\overline{e}_1 \times \overline{h}_1\right) \cdot \overline{z} ds$$

(b) Coupling due to multiple apertures

(i) Without mutual coupling between the apertures

Let $E_1^{CF,CB}, E_2^{CF,CB}$, ---, $E_N^{CF,CB}$ represent the coupling due to apertures 1,2...N in the respective directions, then the total field due to N apertures in forward and backward directions will be

$$E_T^{CF} = \sum_{i=1}^{N} E_i^{CF} \left(e^{-j\beta_2 . d_{iN}} + e^{-j\beta_1 . d_{1i}} \right) \tag{2.59}$$

$$E_T^{CB} = \sum_{i=1}^{N} E_i^{CB} e^{-j(\beta_1 + \beta_2) d_{1i}} \tag{2.60}$$

where d_{in} is the distance from the center of the i^{th} aperture to the center of n^{th} aperture.

Similarly, the scattered fields can be calculated as

$$E_T^{SF} = \sum_{i=1}^{N} E_i^{SF} \tag{2.61}$$

$$E_T^{SB} = \sum_{i=1}^{N} E_i^{SB} e^{-2j\beta_1 d_{1i}} \tag{2.62}$$

(ii) With mutual coupling between the apertures

In a multi-aperture environment, the coupling value of a specific aperture is modified due to the presence of other apertures. Let the coupler have N apertures, and the coupled field due to the ith aperture in the presence of other apertures in forward and reverse direction be $\overline{E}_i^e F_i$ and $\overline{E}_i^e R_i$, respectively. $\overline{E}_i^e$ is the modified incident field on the ith aperture. If the first (Nth) aperture is considered, coupling is effected only by the reverse (forward) coupled fields of the other apertures. The coupling at the ith aperture is effected by the forward coupled fields of (i-1) apertures and the reverse coupled fields of the next (N-i) apertures. Therefore, the effective incident field at the *i*th aperture can be written as

$$\overline{E}_i^e = \overline{E}_{io} - \frac{\varepsilon_{r2}}{\varepsilon_{r1}}\left(\overline{E}_1^e F_1 e^{-j\psi_{1i}} + \ldots + \overline{E}_{i-1}^e F_{i-1} e^{-j\psi_{(i-1)i}} + \overline{E}_{i+1}^e R_{i+1} e^{-j\psi_{(i+1)i}} + \ldots + \overline{E}_N^e R_N e^{-j\psi_{iN}}\right) \quad (2.63)$$

where $\psi_{ij} = \beta_2 d_{ij}$, and $\overline{E}_{io}$ is the original incident field. N apertures in the coupler form N simultaneous equations, which can be solved for effective incident fields. F_i and R_i depend on the dimensions of the aperture. Then the total fields in forward and reverse directions are

$$\overline{E}_T^{CF} = \sum_{i=1}^{N} \overline{E}_i^e F_i e^{-j\psi_{iN}} \quad (2.64)$$

$$\overline{E}_T^{CR} = \sum_{i=1}^{N} \overline{E}_i^e R_i e^{-j\psi_{1i}} \quad (2.65)$$

2.3 Conclusions

The methods discussed in this chapter can be employed in any scenario of proximity or aperture coupled lines. They will be used as a basis for the analysis of waveguide, stripline or microstrip media. The microstrip media can be converted into a parallel plate waveguide model in order to apply above principles, e.g. [5].

Chapter-III

3 Design and Analysis of Strip-To-Microstrip Line Coupler

Introduction

One of the important aspects of component design is the tradeoff between miniaturization and power handling capability. Although miniaturization has been generally achieved by utilizing microstrip technology, the main application-oriented difference between microstrip and stripline circuits is their power handling capability [6]. If the performance of a stripline circuit at moderate power level is to be monitored through signal extraction by a weak coupler, it is often appropriate to design the control circuit in low-power microstrip technology to take advantage of its easier manufacturing and integration process. In many applications, a standard proximity coupler would be appropriate for such a task. In UHF and VHF bands, however, such an approach results in a relatively large component due to the required quarter-wavelength coupling section. In order to eliminate this restriction, a concept built on aperture coupling through a common ground plane has been presented in [7] [8].

This chapter focuses on a new design, which further reduces component size to one fifth of a wavelength. As shown in Fig. 3.1, coupling is achieved through apertures in the common ground plane between the stripline and the microstrip configuration. Since these couplers exhibit generally weak coupling, increasing a single aperture dimension will not extend coupling beyond a certain level, thus saturating the amount of coupling. This property sets the limit for the maximum aperture dimension. Coupling values and bandwidth are improved by utilizing multiple apertures in some sort of a tapered-size arrangement.

This chapter investigates, both theoretically and experimentally, different sets of profiled circular aperture arrangements. Moreover, the current analysis includes mutual interactions of apertures and aperture averaging. It will be demonstrated that this new design results in aperture arrangements of shorter overall component size. One of the important specifications of the coupler is its directivity, which, in aperture couplers, depends on the shape of the aperture. In order for a single aperture to achieve strong backward coupling and minimize forward coupling, the aperture shape must be circular as shown in [9]. In Section 3.1, the analysis of the strip-to-microstrip line coupler including the mutual coupling between the apertures is presented. Section 3.2 demonstrates the design procedure for a desired coupling coefficient with two different types of aperture profiles. Section 3.3 features measured results and comparisons with computations.

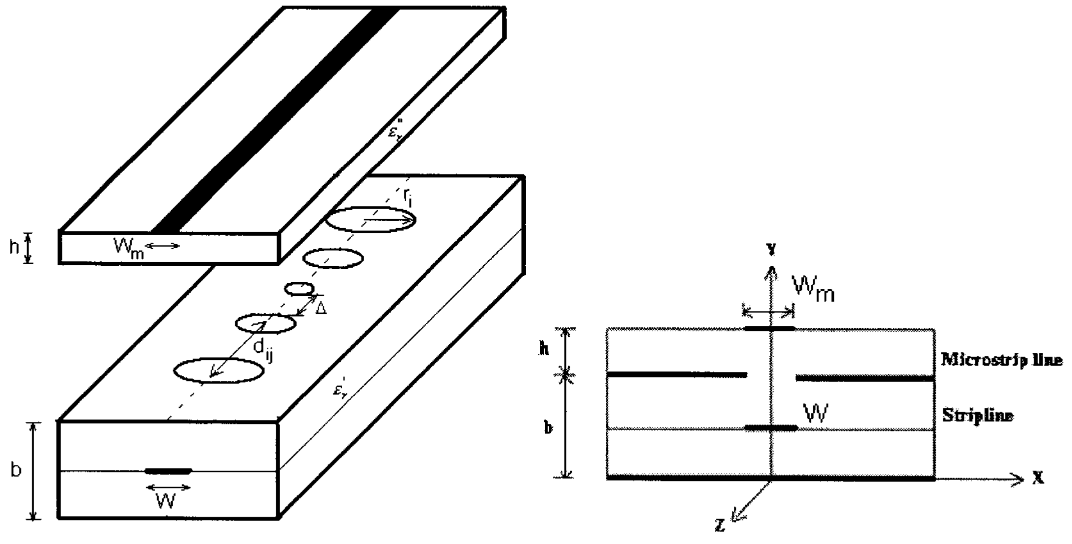

Figure 3.1 Aperture-coupled strip-to-microstrip-line coupler

3.1 Analysis

3.1.1 Single Aperture

As shown in Section 2.2.2, coupling through a small aperture can be accounted for using Bethe's small aperture coupling theory, e.g. [4], [10]. If the normal electric and tangential magnetic fields are not uniform over the coupling aperture, field averaging is required for the calculation of polarization currents. They are assumed at the center of the aperture and, according to (2.29) and (2.30), can be written as

$$\bar{P}_e = \varepsilon_0 \alpha_e \frac{\iint_s E_n ds}{\iint_s ds} \bar{n} \tag{3.1}$$

$$\bar{P}_m = -\alpha_m \frac{\iint_s \bar{H}_t ds}{\iint_s ds} \tag{3.2}$$

$\bar{P}_e$ and $\bar{P}_m$ can be related to electric and magnetic current sources $\bar{J}$ and $\bar{M}$ according to (2.31) and (2.32), which are repeated here for completeness.

$$\bar{J} = j\omega \bar{P}_e \tag{3.3}$$

$$\bar{M} = j\omega \bar{P}_m \tag{3.4}$$

Assuming the quasi-static mode of propagation for the microstrip line, the coupled fields can be represented by forward and backward traveling waves, which are expressed in terms of modal vectors.

$$E^+ = C^+_{ec,mc} \left|\bar{e}_y\right| e^{-j\beta_{gm} z} \qquad z > 0 \tag{3.5}$$

$$H^+ = C^+_{ec,mc} \left|\bar{h}_x\right| e^{-j\beta_{gm} z} \qquad z > 0 \tag{3.6}$$

$$E^{-} = C^{-}_{ec,mc}\left|\bar{e}_{y}\right|e^{j\beta_{gm}z} \qquad z<0 \tag{3.7}$$

$$H^{-} = -C^{-}_{ec,mc}\left|\bar{h}_{x}\right|e^{j\beta_{gm}z} \qquad z<0 \tag{3.8}$$

Here, $C^{\pm}_{ec,mc}$ are the coupling coefficients due to the corresponding sources in their respective directions; $\bar{e}_y$ and $\bar{h}_x$ are modal field vectors, and β_{gm} is the propagation constant in the microstrip line. The coupling coefficients can be determined by using reciprocity theorem and the orthogonal property of the modal vectors. They are

$$C^{+}_{ec} = -\frac{1}{P_{ms}}\int_{v}\bar{e}_{y}\cdot\bar{J}\,dv \tag{3.9}$$

$$C^{-}_{ec} = -\frac{1}{P_{ms}}\int_{v}\bar{e}_{y}\cdot\bar{J}\,dv \tag{3.10}$$

$$C^{+}_{mc} = -\frac{1}{P_{ms}}\int_{v}\bar{h}_{x}\cdot\bar{M}\,dv \tag{3.11}$$

$$C^{-}_{mc} = \frac{1}{P_{ms}}\int\bar{h}_{x}\cdot\bar{M}\,dv \tag{3.12}$$

where $P_{ms} = 2\int_{s_0}\left(\bar{e}_{y}\times\bar{h}_{x}\right)\cdot\bar{z}ds$, and s_0 is the cross section of the microstrip line.

The normalized TEM fields at the ground plane of the stripline can be represented by [11]

$$\bar{E}_{y} = \frac{-V\bar{y}}{b\sqrt{F(m)}}\left(\frac{1}{1+m\sinh^{2}\left(\frac{\pi x}{b}\right)}\right)e^{-j\beta_{gs}z} \tag{3.13}$$

where β_{gs} is the propagation constant in the stripline and

$$m = sech\left(\frac{\pi W}{2b}\right) \tag{3.14}$$

$$F(m) = \frac{8}{\left(\frac{b}{2}\right)^{2}}\int_{-\frac{b}{2}}^{\frac{b}{2}}\int_{-\infty}^{\infty}\frac{dxdy}{\left|1-m^{2}\cosh^{2}\frac{\pi(x+jy)}{b}\right|} \tag{3.15}$$

b is spacing between the ground planes, W the width of the stripline (c.f. Fig 3.1). By using a parallel-plate equivalent model for the microstrip line, the average power flow in the modal fields can be written as

$$P_{ms} = \frac{2h^2}{Z_c} \tag{3.16}$$

where h is the thickness of the dielectric substrate and Z_c the characteristic impedance of the microstrip line.

The total coupling in the microstrip line in positive or negative z direction is the sum of the couplings due to the electric and magnetic currents. Therefore, couplings C^F and C^R in positive and negative z directions, respectively, are

$$C^F = \left(C_{ec}^{+} + C_{mc}^{+}\right)\left|\bar{e}_y\right| e^{-j\beta_{gm} z} \qquad z > 0 \tag{3.17}$$

$$C^R = \left(C_{ec}^{-} + C_{mc}^{-}\right)\left|\bar{e}_y\right| e^{j\beta_{gm} z} \qquad z < 0 \tag{3.18}$$

Applying reciprocity theory [22] for coefficients for C_{ec}^{+}, C_{mc}^{+}, C_{ec}^{-}, C_{mc}^{-} and using (3.13), the coupling coefficients in the forward and reverse direction can be written as

$$C^F = pF = \frac{Z_c A}{120\lambda h^2 b\sqrt{F(m)}}\left(\alpha_e \frac{\varepsilon_r^s \varepsilon_{reff}^m}{\varepsilon_r^s + \varepsilon_{reff}^m} - \alpha_m\sqrt{\varepsilon_r^s \varepsilon_{reff}^m}\right) \tag{3.19}$$

$$C^R = pR = \frac{Z_c A}{120\lambda h^2 b\sqrt{F(m)}}\left(\alpha_e \frac{\varepsilon_r^s \varepsilon_{reff}^m}{\varepsilon_r^s + \varepsilon_{reff}^m} + \alpha_m\sqrt{\varepsilon_r^s \varepsilon_{reff}^m}\right) \tag{3.20}$$

where A is a field averaging factor given by

$$A = \frac{\iint\limits_s \frac{1}{1+m\sinh^2\left(\frac{\pi x}{b}\right)} ds}{\iint\limits_s ds}\ , \tag{3.21}$$

and ε_r^s , ε_r^m are the dielectric constants of stripline and microstrip line, respectively; α_e, α_m are the electric and magnetic polarizabilities of a single aperture.

Since stripline-to-microstrip line couplers exhibit generally weak coupling, increasing a single aperture dimension will not extend coupling beyond a certain level, thus saturating the amount of coupling. This is experimentally verified in Fig. 3.2.

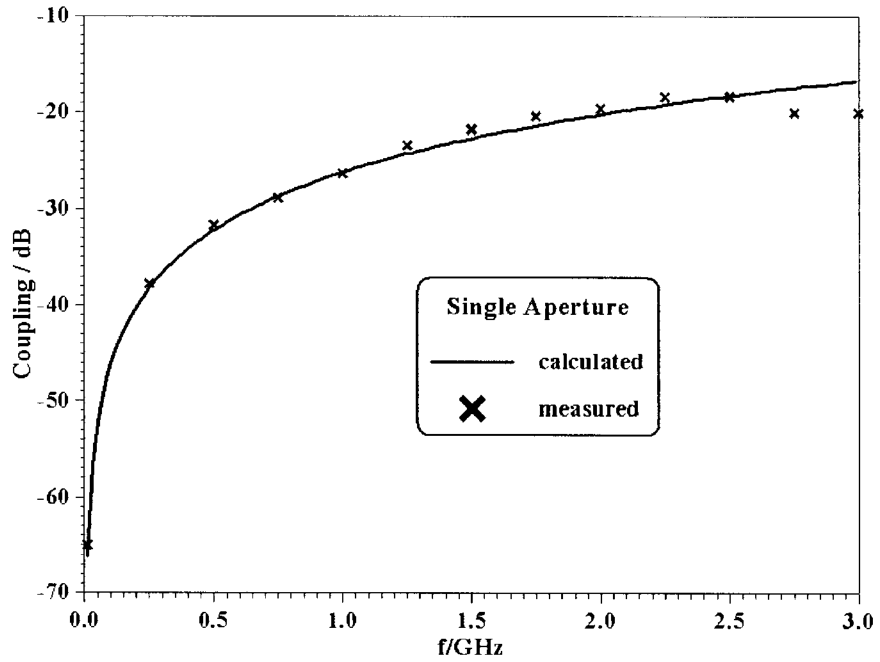

Figure 3.2 Calculated and measured coupling of a single circular aperture(radius=4.1mm) in the common ground plane between stripline and microstrip line according to Fig. 3.1.

3.1.2 Multiple Apertures

In a multi-aperture environment, the coupling value of a specific aperture is modified due to the presence of fields of other apertures. Let the coupler have *N* apertures, and let the coupled field due to the *i*th aperture in the presence of other apertures in forward and reverse direction be $E_i^c F_i$ and $E_i^c R_i$, respectively. If the first (*N*th) aperture is considered, coupling is effected only by the reverse (forward) coupled fields of other apertures. The coupling at the *i*th aperture is effected by the forward coupled fields of *i*-1 apertures and the reverse coupled fields of next the *N-i* apertures. Therefore, the effective coupling at the *i*th aperture can be written as

$$E_i^c = p_i\left\{E_i^s - \left(E_1^c F_1 e^{-j\psi_{1i}} + \ldots + E_{i-1}^c F_{i-1} e^{-j\psi_{(i-1)i}} + E_{i+1}^c R_{i+1} e^{-j\psi_{i(i+1)}} + \ldots + E_N^c R_N e^{-j\psi_{iN}}\right)\right\} \quad (3.22)$$

where $\psi_{ij} = \beta_{gm} l_{ij}$, and l_{ij} are the distances between the *i*th and *j*th apertures. E_i^s is the field at the *i*th aperture in the stripline, and F_i and R_i are obtained from (3.19) and (3.20), respectively.

These simultaneous equations form a matrix equation, which can be solved for effective coupling of an aperture in the presence of other apertures.

Finally, the total coupling of the multi-aperture coupler in forward direction is

$$E_T^F = 20\log\left(\left|\sum_{i=1}^{N} E_i^c F_i e^{-j\psi_{iN}}\right|\right) \quad (3.23)$$

and that in reverse direction

$$E_T^R = 20\log\left(\left|\sum_{i=1}^{N} E_i^c R_i e^{-j\psi_{iN}}\right|\right) \quad (3.24)$$

With these equations, the performance of a profiled multi-aperture strip-to-microstrip line coupler can be analyzed and, for given line parameters, the lengths and aperture diameters synthesized.

3.2 Design

For design simplicity, we assume that the field over the aperture is uniform. In [8] it was found that the maximum aperture diameter, for which the assumption of uniform field holds, is about eight percent of the guided wavelength. If the aperture dimension is too small, the coupling will vary drastically with frequency. Therefore, the ideal dimensions for the aperture are deemed to be between one and eight percent of the guided wavelength. Note that these limits may vary slightly with substrate thickness and dielectric constant.

Now consider a stripline with dielectric constant ε_r^s and ground-to-ground spacing b, and a microstrip line with an effective dielectric constant ε_{reff}^m, e.g. [12], and thickness h, as shown in Fig. 3.1. The characteristic impedance of the microstrip line is Z_c, the width of the stripline is w, and r is the radius of the aperture. Since the polarizabilities of circular apertures are proportional to the third power of the radius [10], we can write the radius of a single aperture for desired coupling C (dB) as

$$r = (\varphi)^{1/3} \tag{3.25}$$

where

$$\varphi = \frac{180\lambda h^2 b\sqrt{F(m)}10^{\frac{-C(dB)}{20}}}{z_C\left[\frac{\varepsilon_r^s \varepsilon_{reff}^m}{\varepsilon_r^s + \varepsilon_{reff}^m} + 2\sqrt{\varepsilon_r^s \varepsilon_{reff}^m}\right]} \tag{3.26}$$

and $F(m)$ and m given by (3.15) and (3.14), respectively.

If the calculated aperture radius exceeds the maximum value, more than one aperture is required to realize the desired coupling. In order to minimize the size of the component, we select a constant minimum distance Δ as the gap between the aperture edges (c.f. Fig. 3.1). If N apertures with radii r_i (i=1...N) are used, then

$$\varphi = \left|\sum_{i=1}^{N} r_i^3 e^{-j(\beta_{gs}+\beta_{gms})d_{1i}}\right| \tag{3.27}$$

where $$d_{1i} = (r_1 + r_i) + 2\sum_{k=2}^{i-1} r_k + (i-1)\Delta \qquad \text{with } d_{11} = 0 \tag{3.28}$$

and $$\beta_{gs} = \frac{2\pi}{\lambda}\sqrt{\varepsilon_r^s} \tag{3.29}$$

$$\beta_{gms} = \frac{2\pi}{\lambda}\sqrt{\varepsilon^{m}_{reff}} \tag{3.30}$$

For uniform apertures, (3.27) can be solved and d_{1_i} gives the spacing of the apertures from the center of the first aperture.

The radii of the apertures need not be identical and can vary according to any functional form. If δr is the minimum radius of the aperture, then we can let the radii follow any functional form f, for instance

$$r_i = R\left[f\left(\frac{\pi(i-1)}{N-1}\right) + \delta r\right] \tag{3.31}$$

By substituting (3.31) in (3.27), the multiplication factor R can be deduced. The distances between aperture centers can then be calculated as described above.

The response of the coupler with frequency is (theoretically) periodic. The bandwidths of individual couplings are variable, and the first coupling band will have larger bandwidth compared to any other band. If the predicted diameter of the apertures is larger than the specified saturation limit, more apertures will be required to realize the desired coupling. The center frequency of the coupling band can be tuned by adjusting the inter-aperture spacing. Coupling can be tuned by slightly modifying the aperture radius. The number of coupling bands within a broadband frequency range will increase with inter-aperture spacing within a band of frequencies.

3.3 Results

To validate the proposed coupling concept a coupler with six identical apertures is designed for 15 dB coupling. The radii of the apertures are 4.1 mm, and center-to-center spacing is 10.2 mm. The other parameters are $Z_c = 50\ \Omega$, $\varepsilon_r^{s} = \varepsilon_r^{m} = 2.32$, $b = 1.6$ mm and $h = 0.8$ mm. Fig 3.3 compares the calculated and measured coupling performance. Excellent agreement is observed, thus validating the analysis and design procedure. Using the above analysis and design guidelines, three couplers with varying profile of the apertures have been designed. Table 3.1 specifies the design parameters and investigations with respect to bandwidth and component size. As can be seen from Table 3.1, the sinusoidal profile of aperture radii (conventional design with largest aperture in the center) provides the largest bandwidth (89.1 percent) at the expense of a $0.3\lambda_g$ coupler length. Compared to that, the cosine design (smallest aperture in the center) achieves a size (length) reduction of almost 50 percent ($0.17\lambda_g$), yet maintaining a bandwidth within less than ten percent (81 percent) of the sinusoidal profile. The design with a uniform profile of distribution of apertures appears to be a very good compromise between the cosine (largest bandwidth) and sinusoidal (smallest coupler) design.

Table 3.1 Design dimensions of various couplers
f = 1GHz, C = 20 dB, N = 5, b = 1.6 mm, h = 0.8 mm
$Z_C = 50\ \Omega$, $\varepsilon_r^s = \varepsilon_r^m = 2.32$.

Profile	Radius (mm)	Distance[1] (mm)	Bandwidth ± 1 dB	Length[2] λ_g
Cosine	4.06	0	81%	17%
	3.27	9.32		
	1.35	15.94		
	3.27	22.56		
	4.06	31.89		
Sinusoidal	1.54	0	89.1%	30%
	3.72	12.88		
	4.62	31.08		
	3.72	49.29		
	1.54	62.17		
Uniform	3.47	0	83.6%	19.8%
	3.47	9.64		
	3.47	19.27		
	3.47	28.91		
	3.47	38.54		

[1] Note that the distance is measured from the center of the first aperture to the center of the respective next aperture.

[2] Length is measured from the left edge of the left-most aperture to the right edge of the right-most aperture.

The size difference is shown in Fig.3.4 which depicts, from left to right, the cosine profile of circular apertures, the (much longer) sine profile of apertures, the stripline and the microstrip circuitry.

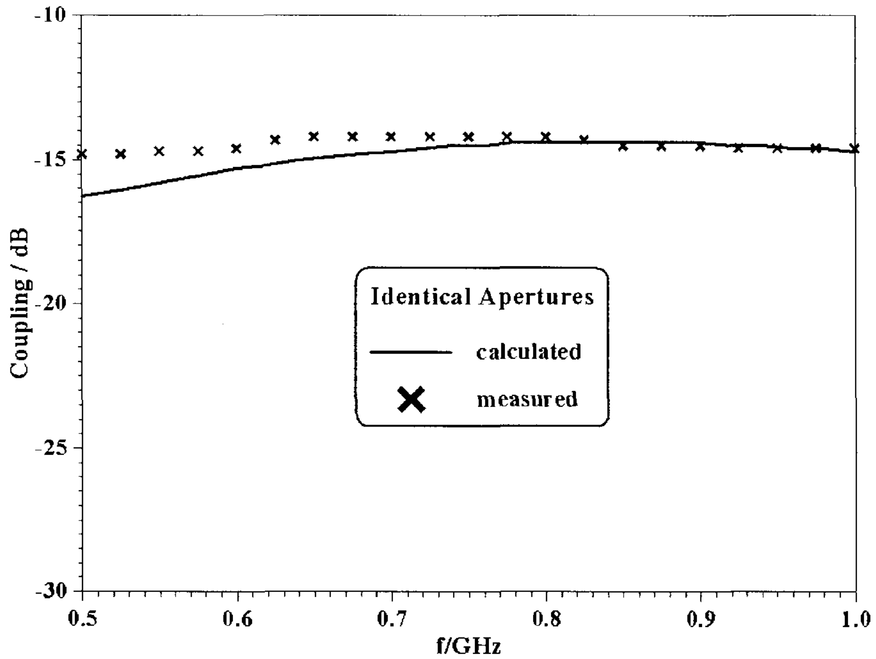

Figure 3.3 Measured (xx) and calculated (solid line) coupling performance of stripline-to-microstrip coupler with six identical apertures centered at 0.75 GHz.

The measured results of the prototype couplers are shown in Figs. 3.5 and 3.6 and are directly compared to computations in Fig. 3.5a and Fig. 3.6a. Unfortunately, the prototypes were printed on a substrate with reduced thickness: 0.508mm instead of 0.8mm. This increases the coupling significantly. Moreover, the return loss is strongly influenced by the violation of the weak-coupling assumption and, more importantly, by the drastic change in characteristic impedance due to the reduced substrate heights. In order to be able to verify the design and analysis concept presented here and, at the same time, demonstrate that the cosine profile yields smaller component size with comparable performance, the reduced substrate height was used in a recalculation of the two prototype couplers.

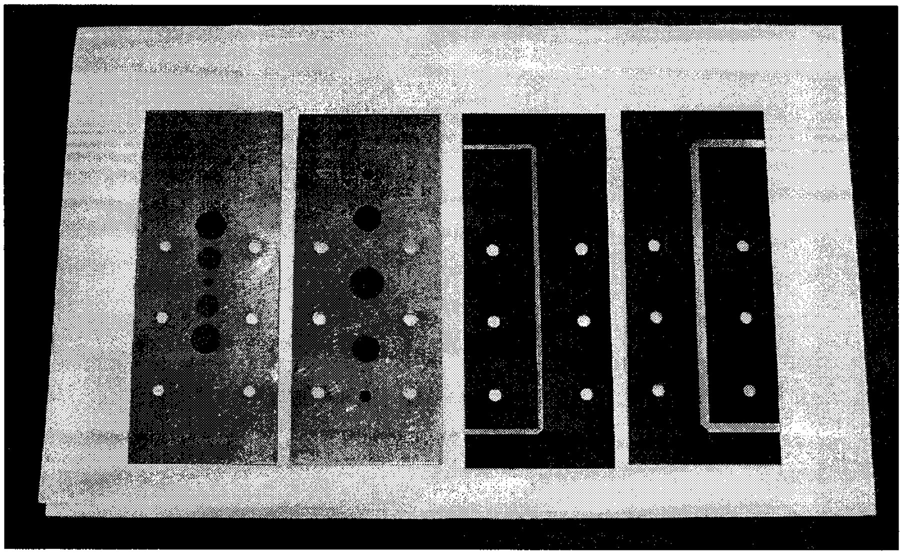

Figure 3.4 Photograph of parts of the prototype aperture-coupled strip-to-microstrip-line couplers. From left to right: aperture pattern of cosine profile, aperture pattern of sine profile, stripline circuit, and microstrip circuit.

Fig. 3.5a shows a direct comparison of measured and calculated forward and backward coupling for the cosine profile. Good agreement is observed for both coupling directions, thus verifying the theory presented in the previous sections. Measured reflection and transmission coefficients with respect to the stripline ports are presented in Fig. 3.5b. As expected from the reduction in substrate height, the reflection coefficient is only 6 dB in the upper frequency range but down to 12 dB towards the lower frequency range. The measured transmission performance is in the 1 dB range.

Corresponding curves for the sine profile are shown in Figs. 3.6. After reassembling circuits and connectors for this coupler, the agreement between measured and computed results deteriorated. While the return loss (Fig. 3.6b) is slightly better than that of the cosine profile (Fig. 3.5b), the coupling behavior (Fig. 3.6a) shows no advantage to that of the cosine profile (Fig. 3.5a). Since also the insertion loss measurements of both couplers are similar, we believe that the much smaller size of the coupling region of the cosine-profiled coupler (c.f. Table 3.1 and Fig. 3.4, left) makes this design more attractive in practical applications. With five apertures, it covers a wide bandwidth at an overall length of one fifth of a wavelength at midband frequency.

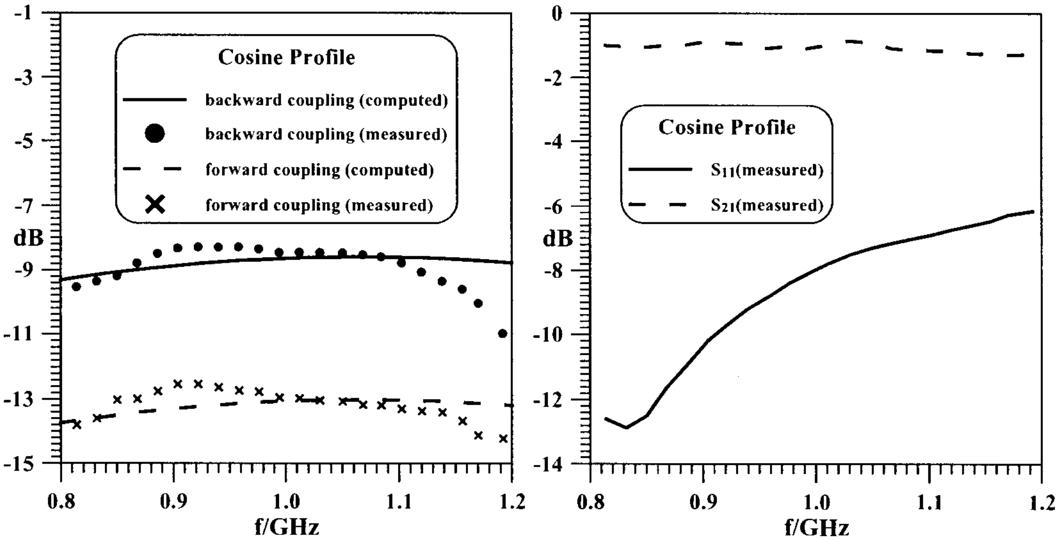

(a) (b)

Figure 3.5 Measured and computed results of strip-to-microstrip line coupler prototype with cosine profile of circular apertures.

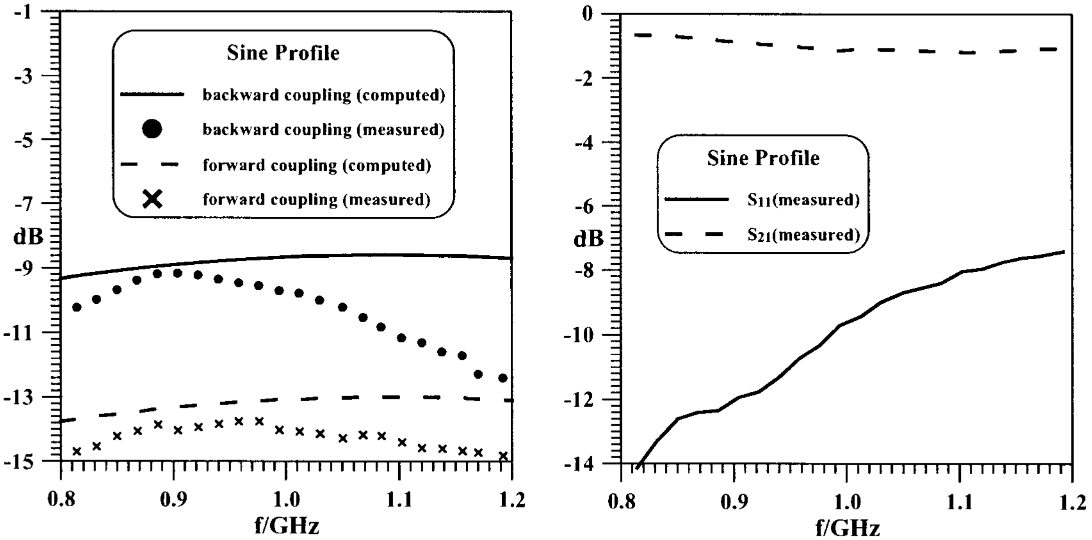

(a) (b)

Figure 3.6 Measured and computed results of strip-to-microstrip line coupler prototype with sine profile of circular apertures.

3.4 Conclusions

It is demonstrated, both in theory and measurements that a strip-to-microstrip line coupler featuring a cosine profile of circular apertures in the common ground plane is a more attractive option than one based on the more standard sine profile. While both couplers show comparable circuit performance, the one with cosine profile is significantly shorter. Simple design guidelines and an analysis based on weak coupling provide the design engineer with simple tools for the design of strip-to-microstrip line couplers.

Chapter-IV

4 Analysis and Initial Design of Rectangular Waveguide Cross-Slot Coupler

Introduction

Coupling between two waveguides play an important role in the design of directional couplers and filters. The standard design process consists of an initial design followed by a full-wave analysis and optimization. The design cycle is shortened considerably if the initial design is close to the desired performance.

An initial coupler design usually involves Bethe's coupling theory [4]. However, this approach is applicable only for small apertures and only for aperture shapes (e.g., circular or rectangular) with well-known expressions for their electric and magnetic polarizabilities, e.g. [10], [13], [14]. Since the theoretical computation of polarizabilities for an arbitrary aperture is mathematically complex, such shapes and/or larger apertures require the use of full-wave methods even in the early design stages, e.g. [15], thus leading to prohibitively long prototype developments.

One of the important apertures in coupler, filter and antenna feed system design is the cross slot, e.g. [15], [16], [17], [18]. Its analysis and initial design, however, is hampered by the lack of expressions for its electric and magnetic polarizabilities. The calculation of theoretical values, especially for the cross slot with rounded corners, is mathematically difficult and computationally time-consuming. So far, only measured electric and magnetic polarizabilities are available for the cross slot [19], [20].

In this chapter, an analysis and initial design concept for cross-slot couplers is presented. To facilitate a speedy design process, the measured data for the polarizabilities in [19], [20] have been curve fitted by a least square method, and large cross-slots are analyzed by field averaging. By utilizing concepts similar to those in Chapter 3 and [21], a fairly simple strategy for the analysis and initial design of E-plane waveguide cross-slot couplers is developed. This approach includes the effect of the orientation of the slot and allows coupling between asymmetric waveguides.

4.1 Theory

4.1.1 Small Cross-Slot

Fig. 4.1 shows the E-plane waveguide directional coupler with a cross-slot in the common broad wall. Assuming monomode propagation, the electromagnetic field incident at port 1 can be written as

$$E_y = \sin\left(\frac{\pi x}{a}\right)e^{-j\beta z} \tag{4.1}$$

$$H_x = -\frac{1}{Z}\sin\left(\frac{\pi x}{a}\right)e^{-j\beta z} \tag{4.2}$$

$$H_z = \frac{j\pi}{\beta a Z}\cos\left(\frac{\pi x}{a}\right)e^{-j\beta z} \tag{4.3}$$

where βz is the phase term in axial direction, and Z is the impedance of the fundamental mode. Using the reciprocity theorem [22], and similar to (3.19) and (3.20), we derive the forward $\left(C^F\right)$ and reverse $\left(C^R\right)$ coupling coefficients for waveguides as

$$C^F = \frac{-j\omega}{P_1}\left[\varepsilon_0\alpha_e \sin^2\left(\frac{\pi h}{a}\right) - \frac{\mu_0\alpha_m}{Z^2}\left[\sin^2\left(\frac{\pi h}{a}\right) + \frac{\pi^2}{\beta^2 a^2}\cos^2\left(\frac{\pi h}{a}\right)\right]\right] \tag{4.4}$$

$$C^R = \frac{-j\omega}{P_1}\left[\varepsilon_0\alpha_e \sin^2\left(\frac{\pi h}{a}\right) + \frac{\mu_0\alpha_m}{Z^2}\left[\sin^2\left(\frac{\pi h}{a}\right) - \frac{\pi^2}{\beta^2 a^2}\cos^2\left(\frac{\pi h}{a}\right)\right]\right] \tag{4.5}$$

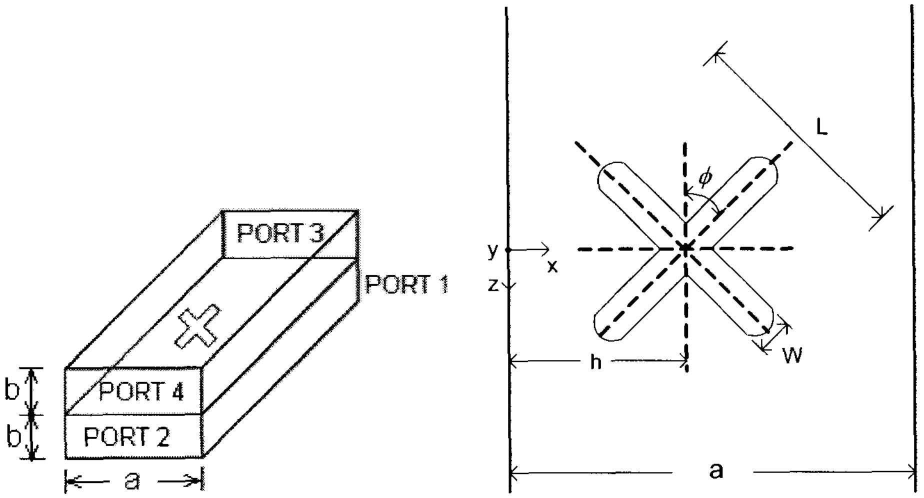

Figure 4.1 E-plane waveguide directional coupler with a cross-slot in the common broad wall.

where $P_1 = \frac{ab}{Z}$, and α_e and α_m are the electric and magnetic polarizabilities of the cross-slot. By curve fitting the measurements in [19], [20] using a least square method, the following closed-form expressions for the polarizabilities are obtained.

$$\alpha_e = 10^{-2} L^3 \begin{bmatrix} -411.5266\left(\frac{W}{L}\right)^5 + 261.1877\left(\frac{W}{L}\right)^4 - 87.8896\left(\frac{W}{L}\right)^3 + \\ 46.68\left(\frac{W}{L}\right)^2 + 0.1901\left(\frac{W}{L}\right) - 0.0007 \end{bmatrix}$$

$$0.1 < \frac{W}{L} \leq 0.35 \tag{4.6}$$

$$\alpha_m = 10^{-2} L^3 \left[2.86 + 36.16\left(\frac{W}{L}\right) - 50.22\left(\frac{W}{L}\right)^2 + 41.39\left(\frac{W}{L}\right)^3 - 13.54\left(\frac{W}{L}\right)^4 \right]$$

$$0.1 < \frac{W}{L} \leq 1 \tag{4.7}$$

Similarly, the scattered fields in the input waveguide can be written as

$$S^F = \frac{j\omega}{P_1}\left[\varepsilon_0 \alpha_e \sin^2\left(\frac{\pi h}{a}\right) - \frac{\mu_0 \alpha_m}{Z^2}\left[\sin^2\left(\frac{\pi h}{a}\right) + \frac{\pi^2}{\beta^2 a^2}\cos^2\left(\frac{\pi h}{a}\right) \right] \right] \tag{4.8}$$

$$S^R = \frac{j\omega}{P_1}\left[\varepsilon_0\alpha_e \sin^2\left(\frac{\pi h}{a}\right) + \frac{\mu_0\alpha_m}{Z^2}\left[\sin^2\left(\frac{\pi h}{a}\right) - \frac{\pi^2}{\beta^2 a^2}\cos^2\left(\frac{\pi h}{a}\right)\right]\right] \tag{4.9}$$

With (4.4), (4.5), (4.8) and (4.9), the S-parameters of the coupler can be represented by

$$S_{11} = 20\log\left|S^R\right| \tag{4.10}$$

$$S_{31} = 20\log\left|C^R\right| \tag{4.11}$$

$$S_{41} = 20\log\left|C^F\right| \tag{4.12}$$

$$S_{21} = 10\log\left(1 - \left|C^F\right|^2 - \left|C^R\right|^2 - \left|S^R\right|^2\right) \tag{4.13}$$

4.1.2 Large Cross-Slot

Apertures in coupling applications frequently assume a larger size than that permitted by Bethe's coupling theory [4]. In order to include larger cross-slot apertures in the initial coupler design process, the fields averaged over the aperture are considered in the analysis rather than those at the aperture center for small cross-slots.

Assuming that the width of the slot is small enough to produce a constant field, typically in the order of one tenth of the waveguide width, then the normalized field averaged over the length of the slot can be represented by

$$\begin{aligned}
E_y^{avg} &= \frac{1}{2L}\left[\int_{\frac{-L}{2}}^{\frac{L}{2}} \sin\frac{\pi}{a}(h - \rho\sin\phi)e^{-j\beta\rho\cos\phi}d\rho + \int_{-\frac{L}{2}}^{\frac{L}{2}} \sin\frac{\pi}{a}(h + \rho\cos\phi)e^{-j\beta\rho\sin\phi}d\rho\right] \\
&= \frac{2}{M^2+N^2}\left[\begin{array}{l} \sin\left(\frac{ML}{2}\right)\cosh\left(\frac{NL}{2}\right)\left(M\sin\left(\frac{\pi h}{a}\right) - N\cos\left(\frac{\pi h}{a}\right)\right) \\ +\cos\left(\frac{ML}{2}\right)\sinh\left(\frac{NL}{2}\right)\left(N\sin\left(\frac{\pi h}{a}\right) + M\cos\left(\frac{\pi h}{a}\right)\right) \end{array}\right] \\
&\quad + \frac{2}{P^2+Q^2}\left[\begin{array}{l} \sin\left(\frac{PL}{2}\right)\cosh\left(\frac{QL}{2}\right)\left(P\sin\left(\frac{\pi h}{a}\right) + Q\cos\left(\frac{\pi h}{a}\right)\right) \\ +\cos\left(\frac{PL}{2}\right)\sinh\left(\frac{QL}{2}\right)\left(Q\sin\left(\frac{\pi h}{a}\right) - P\cos\left(\frac{\pi h}{a}\right)\right) \end{array}\right]
\end{aligned} \tag{4.14}$$

The H_x component is obtained from $H_x^{avg} = -\frac{1}{Z} E_y^{avg}$, and averaging the H_z component leads to

$$H_z^{avg} = \frac{A}{2L}\left[\int_{\frac{-L}{2}}^{\frac{L}{2}} \cos\frac{\pi}{a}(h - \rho \sin\phi) e^{-j\beta\rho\cos\phi} d\rho + \int_{-\frac{L}{2}}^{\frac{L}{2}} \cos\frac{\pi}{a}(h + \rho\cos\phi) e^{-j\beta\rho\sin\phi} d\rho \right]$$

$$= \frac{2A}{M^2+N^2}\left[\begin{array}{l} \sin\left(\frac{ML}{2}\right)\cosh\left(\frac{NL}{2}\right)\left(M\cos\left(\frac{\pi h}{a}\right) + N\sin\left(\frac{\pi h}{a}\right)\right) \\ +\cos\left(\frac{ML}{2}\right)\sinh\left(\frac{NL}{2}\right)\left(N\cos\left(\frac{\pi h}{a}\right) - M\sin\left(\frac{\pi h}{a}\right)\right) \end{array} \right]$$

$$+ \frac{2A}{P^2+Q^2}\left[\begin{array}{l} \sin\left(\frac{PL}{2}\right)\cosh\left(\frac{QL}{2}\right)\left(P\cos\left(\frac{\pi h}{a}\right) - Q\sin\left(\frac{\pi h}{a}\right)\right) \\ +\cos\left(\frac{PL}{2}\right)\sinh\left(\frac{QL}{2}\right)\left(Q\cos\left(\frac{\pi h}{a}\right) + P\sin\left(\frac{\pi h}{a}\right)\right) \end{array} \right] \tag{4.15}$$

The remaining quantities in (4.14), (4.15) are given by

$$A = \frac{j\pi}{\beta a Z};\ M = \frac{\pi}{a}\sin\phi; N = -j\beta\cos\phi;\ P = \frac{\pi}{a}\cos\phi;\ Q = -j\beta\sin\phi \tag{4.16}$$

The coupled fields in forward and reverse direction can then be estimated from

$$C^F = -\frac{j\omega}{P_1}\left[\varepsilon_0 \alpha_e E_{avg}^y \sin\left(\frac{\pi h}{a}\right) + \mu_0 \alpha_m \left\{ -\frac{1}{Z^2} E_{avg}^y \sin\left(\frac{\pi h}{a}\right) + \frac{j\pi}{\beta a Z} H_{avg}^z \cos\left(\frac{\pi h}{a}\right) \right\} \right] \tag{4.17}$$

$$C^R = -\frac{j\omega}{P_1}\left[\varepsilon_0 \alpha_e E_{avg}^y \sin\left(\frac{\pi h}{a}\right) + \mu_0 \alpha_m \left\{ \frac{1}{Z^2} E_{avg}^y \sin\left(\frac{\pi h}{a}\right) + \frac{j\pi}{\beta a Z} H_{avg}^z \cos\left(\frac{\pi h}{a}\right) \right\} \right] \tag{4.18}$$

Since S_{11} equals S_{31}, (4.17) and (4.18) are sufficient to compute the four scattering parameters according to (4.10) – (4.13).

The above expressions are simple and can be straightforwardly implemented. In order to verify the basic approach, Fig. 4.2 shows a direct comparison of this approach with results obtained by HFSS using a slot thickness of 25.4μm. Although slight differences can be observed in the forward (S_{41}) and reverse (S_{31}) coupling performance, the general agreement is good – considering the simplicity of the model – and, therefore, appears feasible in an initial design task. (Note that according to the simplified approach used here, the reverse coupling (S_{31}) always equals the input reflection coefficient (S_{11}).

In order to demonstrate the advantage of field averaging, Fig. 4.3 compares the coupling through a large cross-slot calculated with and without field averaging. It is obvious that the computation without field averaging (dashed lines) fails as the power balance (4.13) results in non-physical solutions for S_{21}. The calculations including aperture field averaging (solid lines), however, produce realistic results, which show good resemblance with Fig. 4.2 considering that the aperture area in Fig. 4.3 is increased by a factor of four. The influence of the slot rotation is depicted in Fig. 4.4 for the large slot of Fig. 4.3, i.e., including slot field averaging. It is obvious from (4.14)-(4.16) that rotating the slot will reduce coupling in two arms of the cross but increase coupling in the two perpendicular arms. Therefore, the influence of slot rotation is relatively small as shown in Fig. 4.4. However, slot rotation by 45 degrees permits a smaller distance between multiple slots and, therefore, contributes to a reduction in component size.

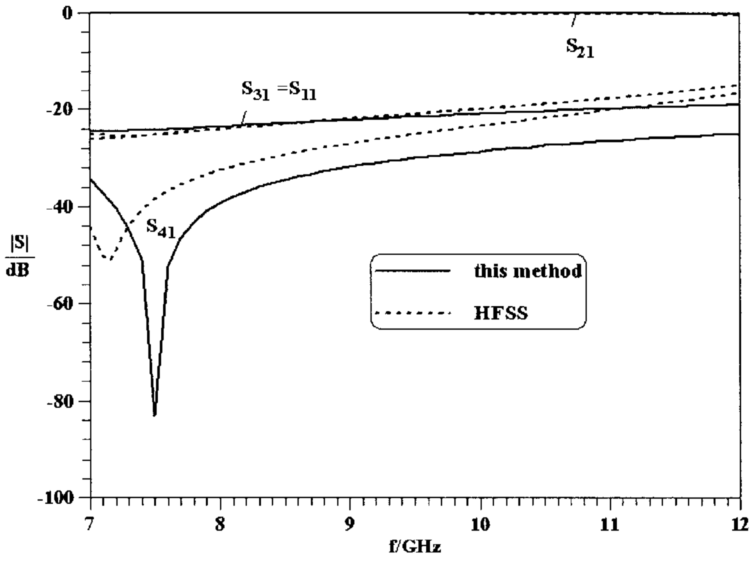

Figure 4.2 Comparison of results of this method (solid lines) and HFSS (dashed lines) for the structure in Fig. 4.1. Dimensions: a=22.86mm, b= 10.16mm, L=10mm, w=2.5mm, h=a/2, $\phi=0°$.

Note that both methods, HFSS and this technique satisfy power balance. The discrepancy between the two S_{41} curves in Fig. 4.2 leads to differences in S_{21}, which falls within plotting accuracy (c.f. (4.13)).

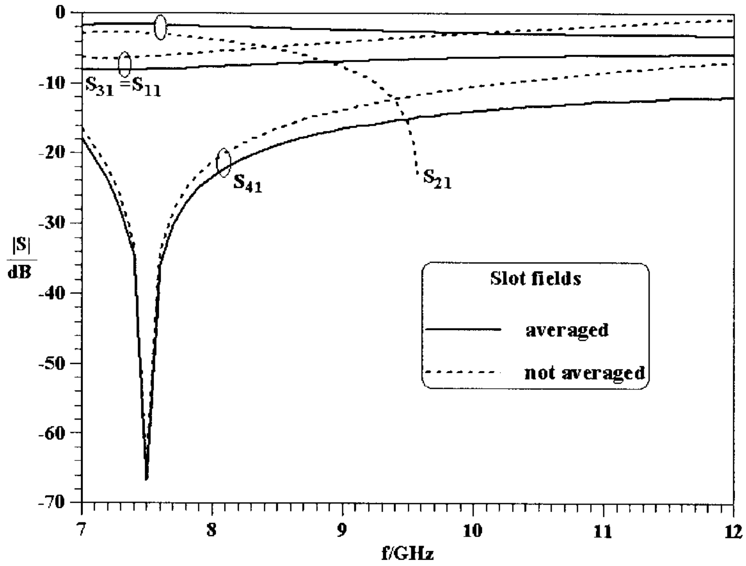

Figure 4.3 Comparison of results with and without slot field averaging
Dimensions: a=22.86mm, b= 10.16mm, L=20mm, w=5mm, h=a/2, ϕ=0°.

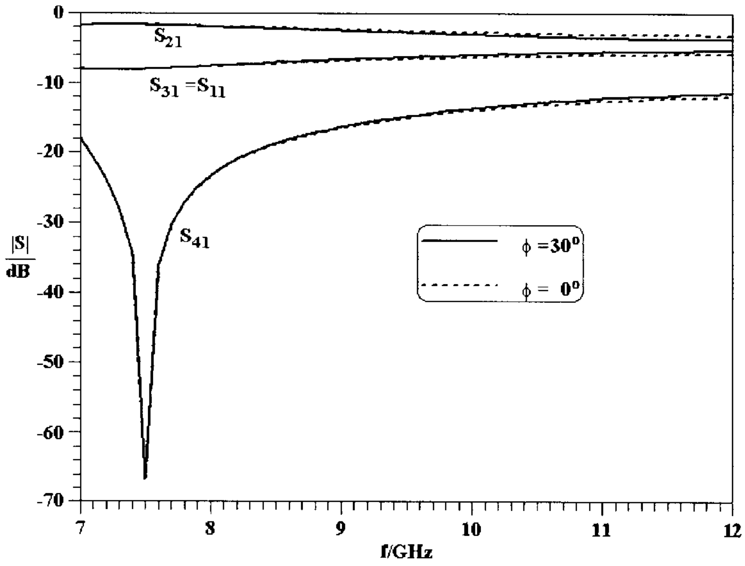

Figure 4.4 Influence of cross-slot rotation
Dimensions: a=22.86mm, b= 10.16mm, L=20mm, w=5mm, h=a/2.

4.2 Coupling Between Different Waveguides

One of the advantages of this approach is the fact that contrary to common coupler design, e.g. [23], the coupled waveguides need not be of the same size. The inset in Fig. 4.5 shows the arrangement of two different waveguides coupled through a cross-slot. By applying an analysis similar to that of Section 4.1.1, we can write the coupling coefficients in forward and reverse directions as follows.

$$C^F = \frac{-j\omega}{P_2}\left[\varepsilon_0\alpha_e \sin\left(\frac{\pi D}{a_2}\right)\sin\left(\frac{\pi h}{a_1}\right) - \frac{\mu_0\alpha_m}{Z_1Z_2}\left[\sin\left(\frac{\pi D}{a_2}\right)\sin\left(\frac{\pi h}{a_1}\right) + \frac{\pi^2}{\beta_1\beta_2 a_1 a_2}\cos\left(\frac{\pi D}{a_2}\right)\cos\left(\frac{\pi h}{a_1}\right)\right]\right] \tag{4.19}$$

$$C^R = \frac{-j\omega}{P_2}\left[\varepsilon_0\alpha_e \sin\left(\frac{\pi D}{a_2}\right)\sin\left(\frac{\pi h}{a_1}\right) + \frac{\mu_0\alpha_m}{Z_1Z_2}\left[\sin\left(\frac{\pi D}{a_2}\right)\sin\left(\frac{\pi h}{a_1}\right) - \frac{\pi^2}{\beta_1\beta_2 a_1 a_2}\cos\left(\frac{\pi D}{a_2}\right)\cos\left(\frac{\pi h}{a_1}\right)\right]\right] \tag{4.20}$$

where $Z_1 = \frac{\omega\mu_0}{\beta_1}$, $Z_2 = \frac{\omega\mu_0}{\beta_2}$, $P_2 = \frac{a_2 b_2}{Z_2}, D = h - \frac{a_1 - a_2}{2}$ and β_1, β_2 are the propagation constants for the TE_{10} modes in the respective waveguides.

As an example, Fig. 4.5 shows a comparison of this theory with HFSS. Although there are differences between the two sets of curves, it is obvious that this approach provides sufficient accuracy to be used as an initial design procedure.

4.3 Design Examples

In this section, we demonstrate that couplers with given specifications can be initially designed using the above analysis.

For simplicity, we assume uniformly spaced identical cross-slot apertures. (Different apertures and aperture spacings can be accounted for by using the procedure in Chapter 3 and [21]).

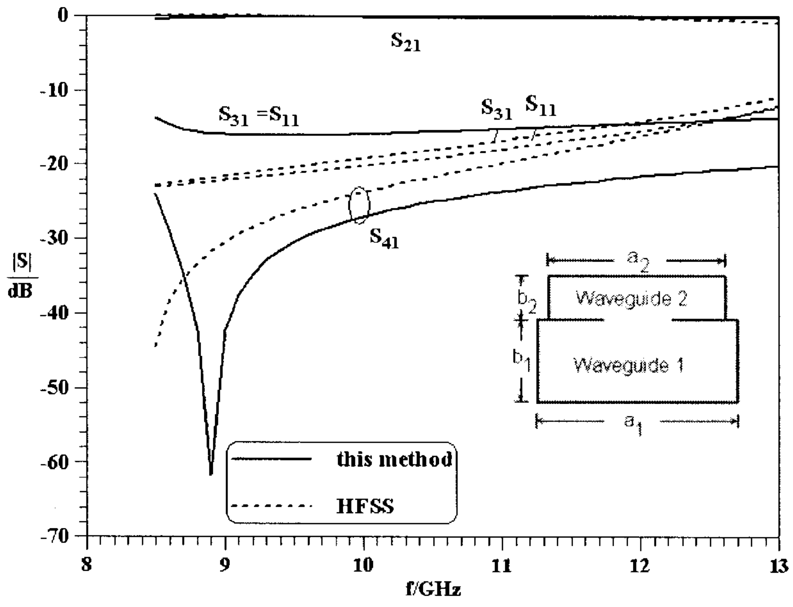

Figure 4.5 Cross-slot coupling between two different waveguides and comparison with results from HFSS. Dimensions: a_1=22.86mm, b_1= 10.16mm, a_2=18mm, b_2= 8mm, L=10mm, w=2.55mm, h=a/2, ϕ=0°.

The coupling due to multiple slots, which are unevenly placed in the common wall between two rectangular waveguides of propagation constants β_1 and β_2, can be written as

$$C_{Total}^{R} = C_s^R \sum_{i=1}^{N} e^{-j(\beta_1+\beta_2)d_{1i}} \tag{4.21}$$

$$C_{Total}^{F} = C_s^F \sum_{i=1}^{N} e^{-j(\beta_1 d_{1i}+\beta_2 d_{iN})} \tag{4.22}$$

where C_s^R and C_s^F are the reverse and forward coupling, respectively, due to a single cross-slot; d_{ij} are the distances between the i^{th} slot and j^{th} slot with $d_{ii}=0$.

In order to demonstrate the validity of our approach for the initial design of waveguide cross-slot couplers, which need not necessarily be directional couplers, we assume in this example a backward coupling (C_{Total}^{R}) of 20 dB at an operating frequency of 10 GHz in

WR90 waveguides. If the design aims for smallest aperture dimensions and maximum reverse coupling, then the distances between the apertures should be $\lambda_g/2$. (Depending on the specific application with respect to forward and backward coupling, the spacing between the apertures can be adjusted.) The only unknown in equation (21) is the dimension of the slot. Fig. 4.6 shows the initial design using this method with three apertures (solid lines) and compares it to the results of an HFSS analysis (dashed lines). The design goal of 20 dB reverse coupling at 10 GHz is achieved exactly, and the forward coupling is almost 10 dB lower (29.9 dB). The respective HFSS values are 21.5 dB and 26.7 dB. Note that the agreement is reasonable over a wider bandwidth and, therefore, allows for an immediate fine optimization in an actual design scenario.

The last example is a conventional 9GHz, 20dB forward directional coupler with three cross-slots and inter-slot distances of somewhat less than $\lambda_g/4$. According to [23], the slots are no longer centered with respect to the waveguide broad wall but are located at h=a/4 (c.f. Fig. 4.1) and, as additional proof of generality, rotated by $\phi=45°$. Fig. 4.7 shows the results obtained with this method and with HFSS. Good agreement can be observed for all four S parameters, hence validating the initial design procedure. The better agreement for S_{41} in Fig. 4.7 compared to that of Fig. 4.6 is attributed to the fact that the respective signal level in Fig. 4.7 is 10 dB above that of Fig. 4.6.

Note that since the cross-slot aperture is fairly complex, we expect our initial design to have a slightly higher deviation from the ideal performance than those reported for simple circular or rectangular apertures, e.g. [24]. Nevertheless, Fig. 4.6 and Fig.4.7 demonstrate initial designs whose performances are close enough to the specifications so that they can be immediately fine-tuned (without any further investigation) using a field-based analysis method and any optimization strategy. Thus the initial design guidelines presented here are a valuable contribution to the pool of CAD procedures for waveguide components.

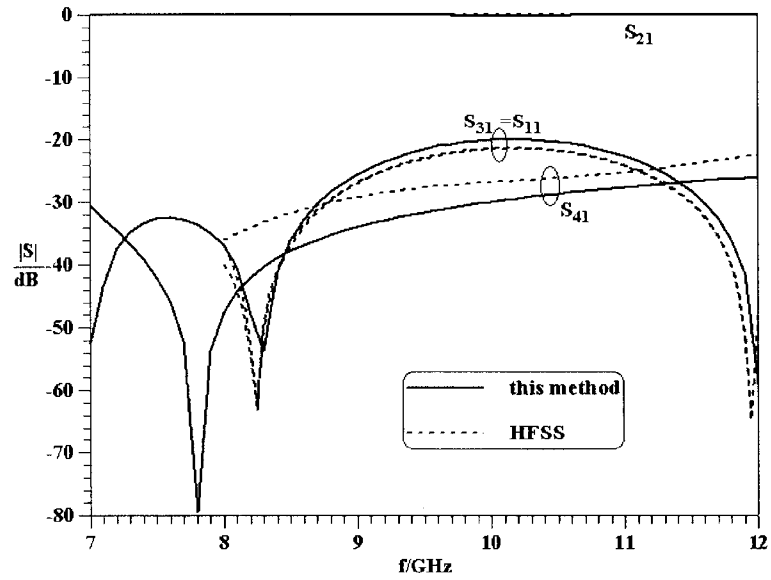

Figure 4.6 Initial design of a three-cross-slot 20dB backward coupler and comparison with results by HFSS. Dimensions: a=22.86mm, b= 10.16mm, L=6.9mm, w=2.1mm, h=a/2, ϕ=0°, d=19.85mm.

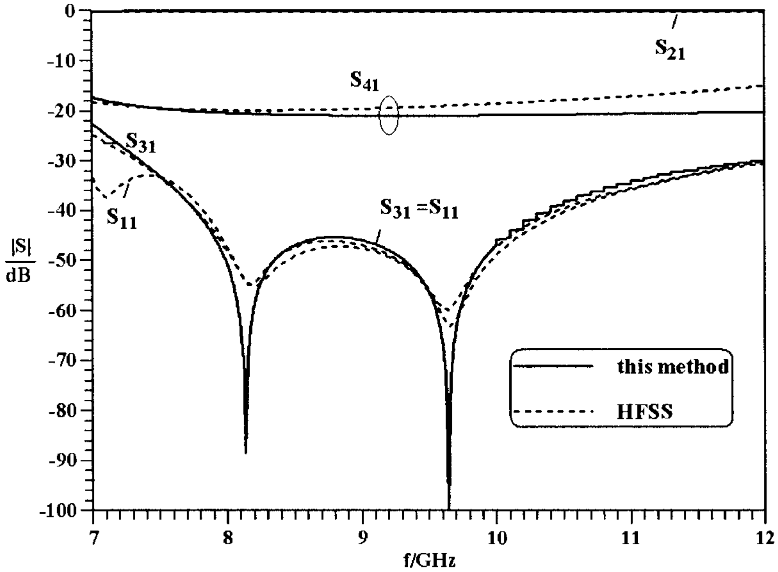

Figure 4.7 Initial design of a three-cross-slot 20dB forward coupler and comparison with results by HFSS. Dimensions: a=22.86mm, b= 10.16mm, L=8.875mm, w=2.66mm, h=a/4, ϕ=45°, d=7.05mm.

4.4 Conclusions

The simplified analysis of cross-slot coupling through the common broad wall of two rectangular waveguides provides a useful tool for the initial design of waveguide cross-slot couplers. The closed-form equations presented here are easily implemented on a computer even though they include the angular rotation of the slots. Moreover, a wide range of slot dimensions is considered through field averaging, and coupling between different waveguides is included. Two three-slot examples exhibiting different coupling schemes are presented. Their verification with HFSS demonstrates the usefulness of this technique for the initial design of waveguide cross-slot couplers.

Chapter-V

5 Design of Compact Single-Channel Rotary Joint

Introduction

In tracking radar applications, rotary joints form the link between the stationary and movable parts of the microwave communication system. Their essential characteristics are high power carrying capability, low insertion loss and good impedance matching. Although a large variety of rotary joints involving coaxial or waveguide technology is available commercially, it is difficult to find related performance measurements in the open literature.

In high-power applications, the single-channel waveguide rotary joint consists of three plane waveguide rings of equal diameter, stacked 'coaxially' with their narrow walls in contact, e.g. [25]. The center ring is halved along its E-plane so that its upper half can be brazed to the output ring and its lower half to the input ring. These two parts are separated by a 0.1 mm gap to avoid friction and wearing of the rings during rotation. As is typical for E-plane structures, this separation does not affect the fundamental- mode field configuration in the center waveguide. In order to couple power from the input to the center ring and further to the output ring, a series of apertures are used. The rings form two stacked 0 dB directional couplers, which can be designed, e.g., according to [23], [26], [27] thus providing full power transfer from the input to the output via the center ring. Matched terminations are incorporated at the ends of the outer rings.

However, in order to perform the full power transfer through the three waveguide rings, the phase relations have to satisfy a 360 degree phase shift along the mean ring length. As the ring diameter is usually specified through other dimensions of the microwave system, provisions for phase adjustments must be incorporated.

Therefore, this chapter proposes a new rotary joint design which, through the incorporation of ridges in the central ring, allows the phase to be adjusted for a given ring diameter. Two pairs of tapered double-ridge sections are introduced in the central waveguide such that one half moves with the upper and the other half with the lower part of the rotary joint. This is depicted in Fig. 5.1.

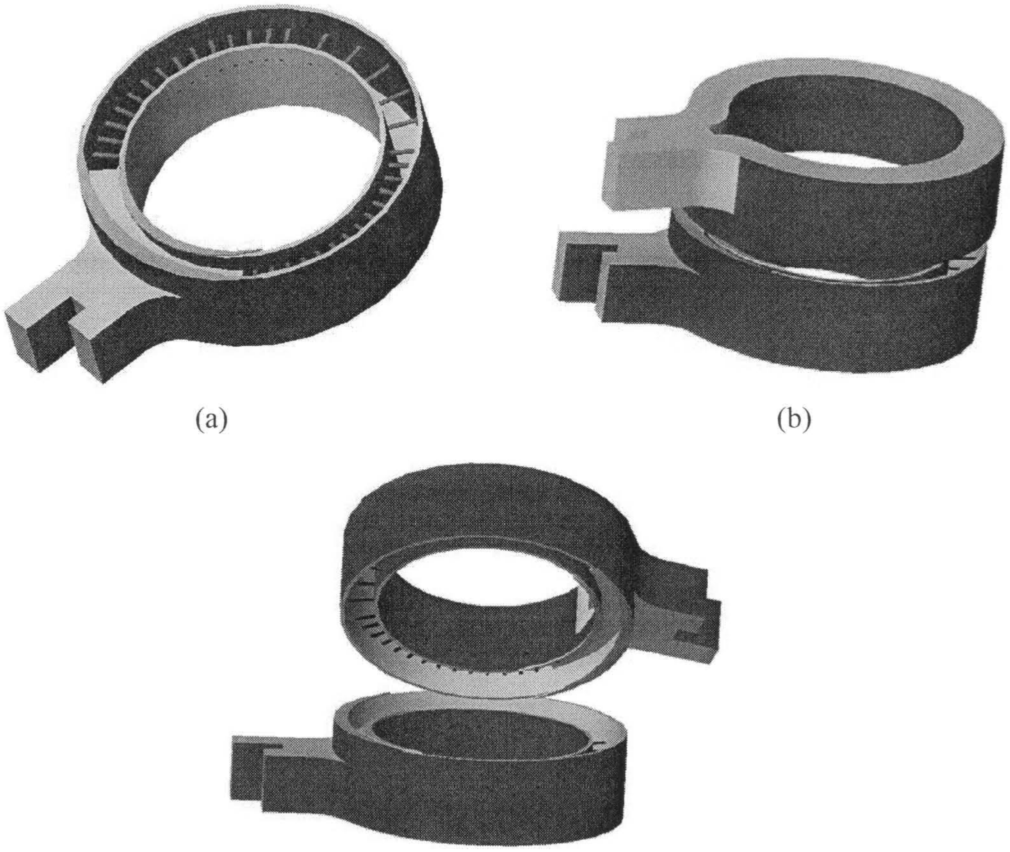

(a) (b)

(c)

Figure 5.1 Compact rotary joint utilizing ridged waveguides to lower the ring diameter
(a) One half of the rotary joint (b) Rotary joint parts aligned in 0-degree position
(c) Rotary joint parts aligned in 180-degree position

5.1 Design Considerations

5.1.1 Transmission Characteristics

The central ring is one of the important parts of the rotary joint. It is a continuous rectangular waveguide ring with apertures (coupling slots) on both of its narrow walls for full power coupling. As a first approximation, we will treat it as a periodic structure considering the middle ring as the unit segment of an infinitely loaded line. Each unit cell consists of a length $L=\pi D$ where D is the mean diameter of the ring. When the signal is coupled from the input ring to the center ring, the power transfer to the output ring will not be completed after one revolution of the wave front. So for maximum power transfer from the input ring to the center ring, the traveling wave after one revolution must be in phase with the incoming signal. This is possible if

$$\pi D = n\lambda_g \tag{5.1}$$

where λ_g is the guided wavelength. A different situation arises when

$$\pi D = \left(n \pm \tfrac{1}{2}\right)\lambda_g \tag{5.2}$$

In this case, the traveling wave has a 180 degrees phase difference after the first revolution. Thus (5.1) and (5.2) give rise to the pass- and stopbands of the rotary joint [25]. The effect of slotting a waveguide is an increase of the guided wavelength [26]. Consequently, the propagation constant β is much lower than in a regular waveguide, and the diameter of the ring required to achieve 2π radians of phase shift will be very high, thus leading to a large and bulky component. In order to arrive at a more compact design, we introduce ridged sections in the center waveguide ring. This measure increases β to very high values so that 2π radians of phase shift can be achieved with a reasonable ring diameter. (Alternatively and without ridges, the ring would not accomplish 360 degrees of phase shift which usually creates small stopbands within a specified passband frequency range [25].)

The entire design of the rotary joint can be made symmetric over its principal diagonal plane. The required phase conditions and aperture positions on the narrow walls of the center waveguide will vary with rotation. The required phase in the center waveguide for one revolution of the field will be $(360-\psi)$ degrees, where ψ is the angular separation between input and output ports. A good design requires these conditions to be satisfied at all angular positions, which can be achieved by the effective use of ridge dimensions and aperture widths.

Since the entire component is symmetric, matching the phase condition between $\psi = 0$ degrees and $\psi = 180$ degrees is sufficient. The 0 degree position is shown in Fig. 5.2a. Once the wave completes one revolution in the center ring, it will have a phase change of $\varphi_1+\varphi_2$, where φ_1 and φ_2 are the phases in regions 1 and 2, respectively. In region 2, the center waveguide has apertures on both of its narrow walls, and they are designed for full power coupling (see Section 5.1.2). Therefore, the traveling wave has 45 degrees phase shift over region 2. The dimensions of the ridges are designed such that the phase changes by 315 degrees in region 1. The extension of the ridges into the coupling region can be taken into account by adding the respective phases.

Fig. 5.2b shows the configuration in the 180 degrees position. Here the required phase for full power transfer from input to output is 180 degrees. The configuration is symmetric with respect to plane DD'. Let φ_1 be the phase change over region 1 where the center waveguide has apertures on only one of its narrow walls.

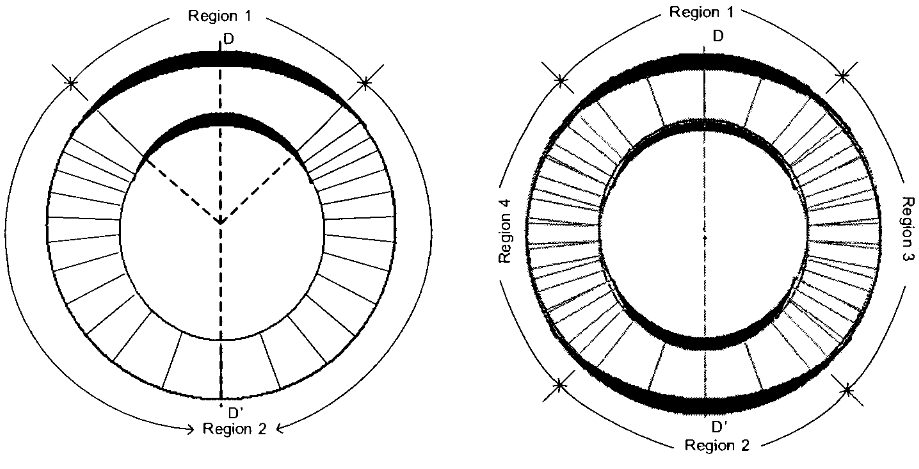

(a) (b)

Figure 5.2 Aperture and ridge configurations in 0-degree position (a) and 180-degree position (b).

Let $\varphi_2 = \phi_2/4$ be the phase change over region 4, where ϕ_2 is the phase difference between even and odd modes due to apertures on one side in region 4. So for phase matching in this position, we require

$$2(\varphi_1 + \varphi_2) = \pi \tag{5.3}$$

Similarly, the phase can be matched in other positions and, therefore, it is possible to match the phase manually for a few angular positions. Optimization might be used to further improve the performance.

5.1.2 Coupler Design

Since, unlike the input and output rings, the center waveguide ring has apertures on both of its narrow walls, the guided wavelength in all the three rings is not the same. To adjust the guided wavelength in the center ring, its broad wall dimension must be slightly reduced. This places a restriction on the design of the 0 dB coupler.

For this purpose, a modified, asymmetric algorithm based on the Mode-Matching Technique (MMT) [23] has been developed, and initial coupler values were obtained using principles described in [26], [27]. Fig. 5.3 compares computed and measured [26] results for the 0 dB uniform-aperture coupler presented in [26]. Good agreement is obtained even though our model features a conversion [28] from the cylindrical pins used in [26] to rectangular cross sections in the MMT. The lighter lines in Fig. 5.3 demonstrate the influence of reducing the width of the coupled guide, i.e., the center ring in the rotary joint.

As is well known, couplers with non-uniform apertures can be synchronously tuned and achieve superior return-loss performance. Therefore, an H-plane coupler with 72 non-uniform apertures was designed for the rotary joint application. In order to adjust the guided wavelength in the center ring, its width is reduced by 2.5 percent, whereas those of the input/output rings are increased by the same amount. The computed performance of this coupler is shown in Fig. 5.4. In comparison with Fig. 5.3, it demonstrates the advantage of the non-uniform aperture design by achieving return-loss and isolation values better than 40 dB.

5.2 Ridge Waveguide Analysis

An accurate evaluation of the fundamental-mode phase constant in the ridged waveguide sections is of fundamental importance for this design. Due to rotation of the two rotary joint parts (c.f. Fig. 5.1), symmetric as well as asymmetric ridged waveguide cross sections appear. A snap-shot cross section is shown in Fig. 5.5.

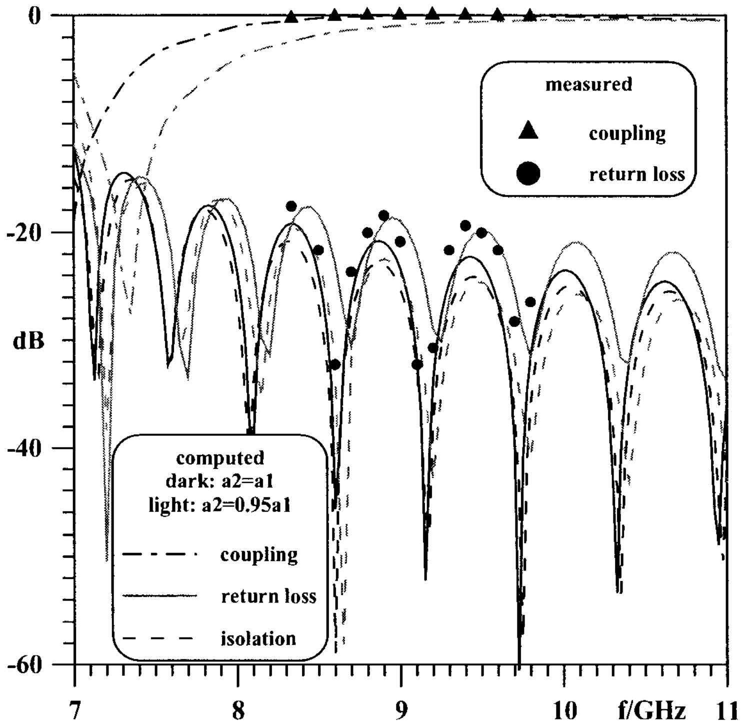

Figure 5.3 Computed and measured [26] response of a 0 dB H-plane coupler with 22 apertures (21 pins). Dark lines calculated with identical widths in main and coupled ports (a2=a1), gray lines with coupled port dimension reduced by five percent (a2=0.95a1).

In order to determine the fundamental-mode phase constants of cross sections pertaining to the rotary joint, a versatile and efficient routine had been developed by the author [29]. The procedure is based on a transverse resonance technique utilizing well-known susceptance relations for the cross-sectional discontinuities introduced by the ridges [2]. The details on the theory and general results, are reported in [29]. Here, we are demonstrating the validity of this approach with respect to the specific cross section of Fig. 5.5.

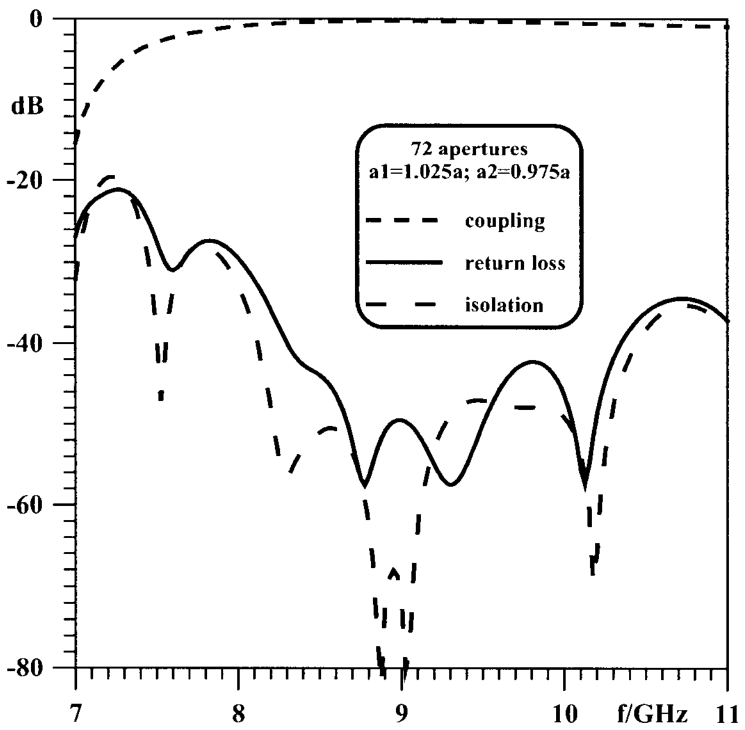

Figure 5.4 Computed response of a 0 dB H-plane coupler with 72 apertures (71 pins) for the 8.8 - 9.2 GHz frequency range. Main and coupled port widths have been offset each by 2.5 percent in opposite directions.

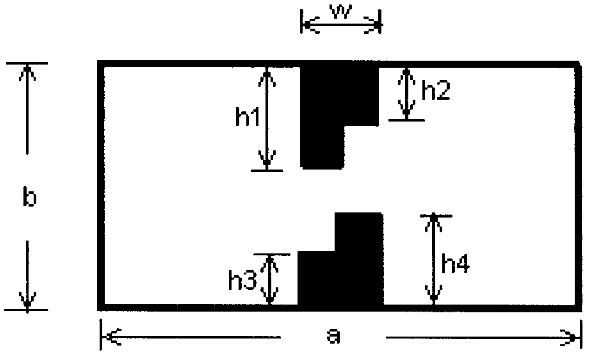

Figure 5.5 Snap-shot of ridged waveguide cross-section obtained by rotation of two halves shown in Fig. 5.1.

A comparison of the results computed by a transverse resonance technique [29] with those obtained by the commercial package HFSS is shown in Table 5.1 and demonstrates good agreement.

Table- 5.1

Cutoff wave numbers of ridge waveguide in Fig. 5.5 calculated using transverse resonance technique [29] and HFSS. a = 22.86 mm, b = 10.16 mm, w = 4 mm. Dimension are in mm. k_c is in rad/mm.

h_1	h_2	h_3	h_4	k_c [29]	k_c (HFSS)
3	2	2	3	0.10615	0.10904
3	3	2	2	0.11062	0.10983
3	3	3	3	0.10216	0.10199
2	3	2	3	0.10551	0.10766

5.3 Results

Using the guidelines presented above, a single-channel waveguide rotary joint was designed for operation at 9.05 GHz. The mean diameter of the rotary joint was specified as 119.38 mm (4.7 inches). A total of 72 non-uniform coupling apertures are employed for full power coupling. The diameter of the grid wire (coupling pins) is 0.5 mm. The center waveguide broad wall is undercut by 2.5 percent; input/output rings are widened by 2.5 percent in order to adjust the guided wavelength in the three rings. The peak heights of the ridges are 2.2 mm and their thickness is 2.0 mm in one half of the rotary joint.

The center ring is halved along the central axis of the transverse cross section. The upper and lower halves of the center ring are brazed to the output and input rings, respectively. The so-obtained upper and lower halves of the rotary joint are separated by a 0.1 mm ball bearing structure. This separation avoids friction and wearing of the rings and has negligible effect on the field configuration in the center waveguide for fundamental mode operation. In general, waveguide rotary joints have long-life rubber seals to protect the inside of the waveguides and the ball bearings from humidity and dust.

Fig. 5.6 shows the measured transmission characteristic of the rotary joint in the 0 degrees position. The passband is centered at 9.05 GHz with stopbands appearing at 8.75 GHz and 9.33 GHz.

Measurements of the insertion loss at different angular positions are presented in Fig. 5.7. The measured insertion loss is better than 1 dB between 8.9 GHz and 9.17 GHz. It is expected that the bandwidth may be improved by optimizing the aperture widths and ridge dimensions for the required phase match in different angular positions.

In order to ensure high-power handling capability, the prototype rotary joint was tested at a peak power of 100 KW. The final design is supposed to operate up to 250 KW.

Transition phase responses of the input and output couplers are linear with respect to frequency. Therefore, although the absolute phase value changes in the individual positions measured in Fig. 5.7, the frequency linearity is preserved. As the joint rotates with only 44 rpm, the influence of the rotation on the phase linearity is of no concern.

5.4 Conclusions

It is demonstrated that by incorporating ridge waveguide sections, a single-channel waveguide rotary joint can be designed which simultaneously achieves high-power handling capability, reduced component size and correct signal phase conditions. The presented design guidelines demonstrate the feasibility of this concept. Prototype measurements validate the design approach.

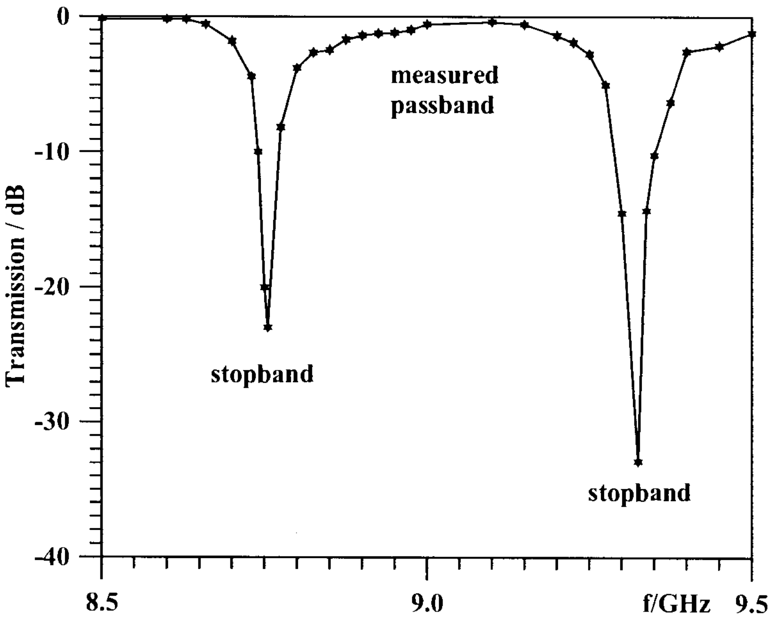

Figure 5.6 Measured broadband transmission performance of waveguide rotary joint prototype in the 0-degree position.

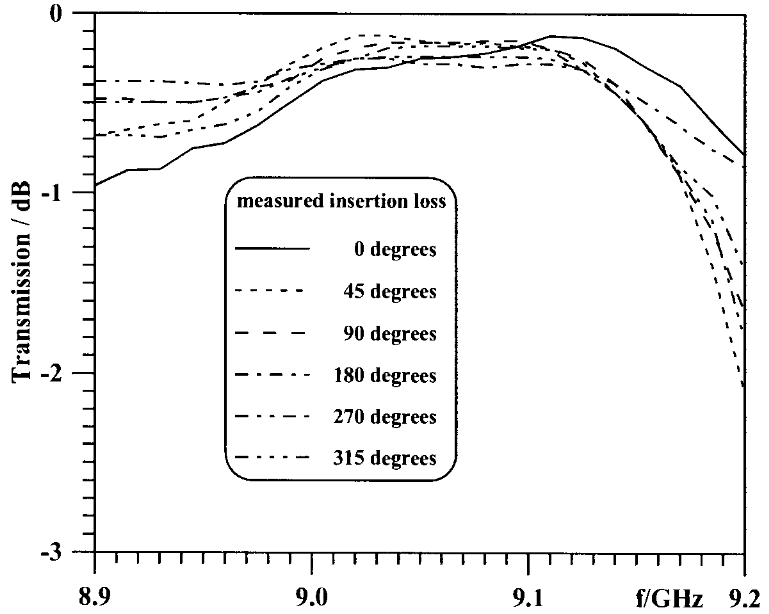

Figure 5.7 Measured narrowband transmission performance of rotary joint prototype in various angular positions.

Chapter-VI

6 Analysis and Design of Stepped Impedance Resonator LTCC Filter

Introduction

RF and microwave system-on-chip (SOC) modules for wireless communications are increasingly fabricated in low temperature co-fired ceramic (LTCC) technology, e.g. [30], [31]. Filter components with transmission zeros are integral parts of the design methodology, and several designs have been presented, e.g. [32] – [34].

In [32], two stripline stepped-impedance resonators (SIR's) are coupled electromagnetically to form a single attenuation pole, which can be controlled through a planar transmission line on a layer beneath the SIR's [33]. A two-pole filter with two attenuation poles, one on either side of the passband, has been developed based on inductively coupled resonators with a feedback capacitance between input and output [34]. However, the attenuation of this filter decreases towards higher frequencies.

In this chapter, first, we propose a filter configuration with improved performance in the stopband. It is based on all capacitively coupled strips with two stripline SIR's and utilizes coupling from source to load as well as from source/load to both SIR's. Two attenuation poles are created on either side of the passband, and their locations can be controlled by varying the coupling capacitances.

Secondly, we present a simplified analysis of capacitively coupled stripline components in LTCC, which permits the design engineer to perform a fast initial design of this class of LTCC filters.

6.1 Filter Structure

Fig. 6.1 shows the schematic of the proposed filter including the capacitances used for the coupling scheme. Fig. 6.2 shows the equivalent circuit model for the proposed filter. Four layers of dielectrics are sandwiched between two ground planes. The SIR's are located on layer #2. An external coupling pad is provided on layer #1 and is used to control the location of the attenuation poles. The input/output pads are printed on layer #3. The orientation and shape of these pads must simultaneously satisfy the source/load capacitance C_{12} and input/output capacitances C_1, C_2. The spacing between the resonators and the length of the resonators can be tuned to the desired pass band of the filter. The cross coupling between the input/output pad and the second/first resonator, which is represented by C_x in Fig. 6.2, is very crucial for the locations of the attenuation poles. Without these cross couplings, the attenuation poles would be symmetric about the passband. With proper control of the cross couplings, the shape of the stopband can be improved.

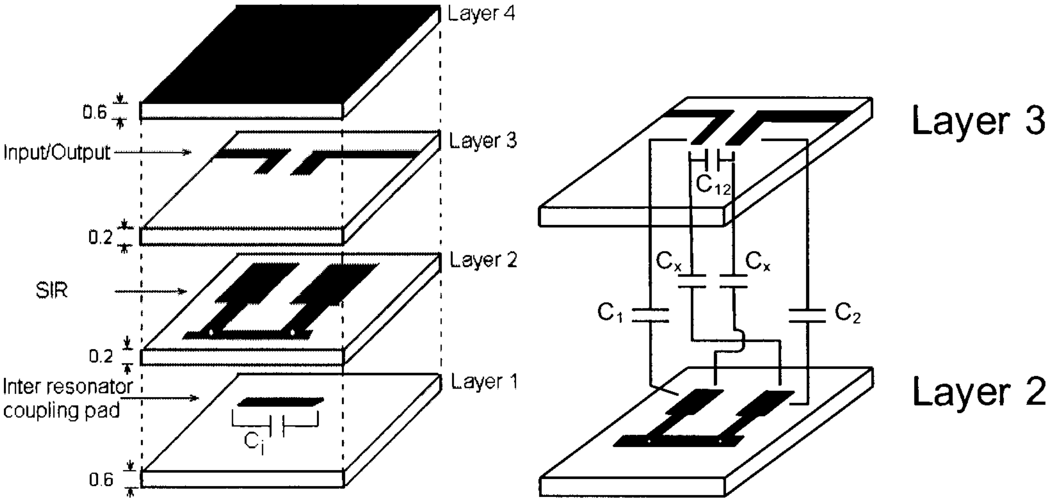

Figure 6.1 Proposed filter structure and capacitors involved in the coupling scheme (layer thicknesses in mm).

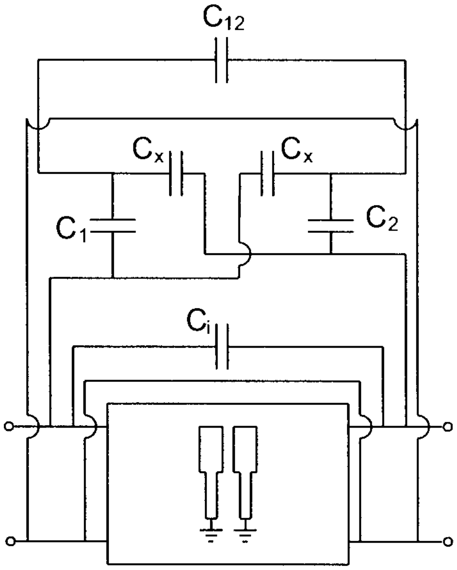

Figure 6.2 Equivalent circuit of the structure in Fig. 6.1

6.2 Theory

According to Fig. 6.2, a matrix representation of the entire circuit can be obtained by adding the admittance matrices of the parallel-coupled lines and the inter-resonator capacitance C_i and converting to impedance matrix. By adding the impedance matrix of the block containing C_1, C_2 and C_x, converting the result back to admittance representation and adding the admittance matrix of the source-load capacitance C_{12}, the circuit is completely described. With the admittance matrix of the coupled SIR's given in [32] and assuming $C_1=C_2=C_0$ due to the symmetry of the circuit, the scattering parameters S_{11} and S_{21} of the filter are then given by

$$S_{11} = \frac{\left(\frac{N}{M^2-N^2}+\omega C_{12}\right)^2 \frac{1}{Y_0^2} - \left(\frac{M}{M^2-N^2}-\omega C_{12}\right)^2 \frac{1}{Y_0^2} + 1}{\frac{1}{Y_0^2}\left[\frac{1}{M^2-N^2} - \frac{2\omega C_{12}}{M-N}\right] + \frac{2j}{Y_0}\left[\frac{N}{M^2-N^2}+\omega C_{12}\right] + 1} \tag{6.1}$$

$$S_{21}=\frac{-2j\left[\dfrac{M}{M^2-N^2}-\omega C_{12}\right]\dfrac{1}{Y_0}}{\dfrac{1}{Y_0^2}\left[\dfrac{1}{M^2-N^2}-\dfrac{2\omega C_{12}}{M-N}\right]+\dfrac{2j}{Y_0}\left[\dfrac{N}{M^2-N^2}+\omega C_{12}\right]+1} \tag{6.2}$$

where Y_0 is the admittance of the connected lines at the input/output ports, and the other quantities are given by

$$M=\frac{Q-\omega C_i}{(Q-\omega C_i)^2-(P+\omega C_i)^2}+\frac{\omega\dfrac{C_x}{2}}{\dfrac{1}{4}\omega^2C_x^2-\omega^2\left(C_o+\dfrac{1}{2}C_x\right)^2} \tag{6.3}$$

$$N=\frac{P+\omega C_i}{(Q-\omega C_i)^2-(P+\omega C_i)^2}+\frac{\omega\left(C_o+\dfrac{1}{2}C_x\right)}{\dfrac{1}{4}\omega^2C_x^2-\omega^2\left(C_o+\dfrac{1}{2}C_x\right)^2} \tag{6.4}$$

$$Q=\left[\frac{k_o\alpha-k_e\beta-(\alpha+\beta)t^2}{2\alpha\beta t}\right] \tag{6.5}$$

$$P=\left[\frac{-k_o\alpha-k_e\beta+(\alpha+\beta)t^2}{2\alpha\beta t}\right] \tag{6.6}$$

where $k_e=\dfrac{Z_{e2}}{Z_{e1}}$, $k_o=\dfrac{Z_{o2}}{Z_{o1}}$, $\alpha=k_e(1+k_e)Z_{e1}$, $\beta=k_o(1+k_o)Z_{o1}$, $t=\tan\left(\dfrac{2\pi f\sqrt{\varepsilon_r}L_{1,2}}{c}\right)$.

$Z_{e/o}$ are the even/odd-mode impedances of the coupled line resonator sections of lengths $L_1=L_2$ [32], f is the frequency and c the speed of light. The position of the attenuation poles is determined by letting $S_{21}=0$ in (6.2).

In order to relate the dimensions of the actual structure to the quantities involved in the computation of (6.1) and (6.2), well-known expression for the individual capacitances are used as outlined below.

6.2.1 Input and Output Capacitances

The input and output capacitances of the filter are estimated by using the thin-film capacitance model [6]. The capacitive pads are bent to miniaturize the structure as well as to achieve the desired input and output capacitances. The capacitance between the pad and the resonator beneath can be represented as a parallel combination of two capacitors (e.g., C_1, $C_2 = C_a + C_b$) as shown in Fig. 6.3.

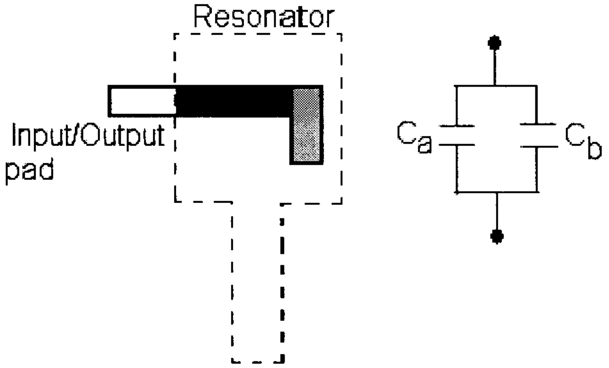

Figure 6.3 Model to calculate input and output capacitances C_1, C_2 in Fig. 6.2; C_a and C_b refer to the dark and grey parts, respectively.

The values C_a, C_b for the two sections shown in Fig. 6.3 are computed from

$$C_{a,b} = \frac{\varepsilon_r \varepsilon_0 \left(l_{a,b} + \Delta f\right)\left(w_{a,b} + \Delta f\right)}{h} \tag{6.7}$$

where $l_{a,b}$ and $w_{a,b}$ are the lengths and widths of the two sections, respectively; h is the substrate thickness between the pad and the resonator, and $\Delta f = 4h\ln(2)/\pi$ represents the fringing fields.

6.2.2 Inter-Resonator Capacitance

The inter-resonator capacitance can be represented as shown in Fig. 6.4. C_a and C_b are capacitances between resonator 1 and 2, respectively, and the strip. They are connected in series (i.e., $C_i = C_a C_b / (C_a + C_b)$) and can be estimated using the above thin-film capacitance model (6.7). These two capacitors are connected in series with the strip.

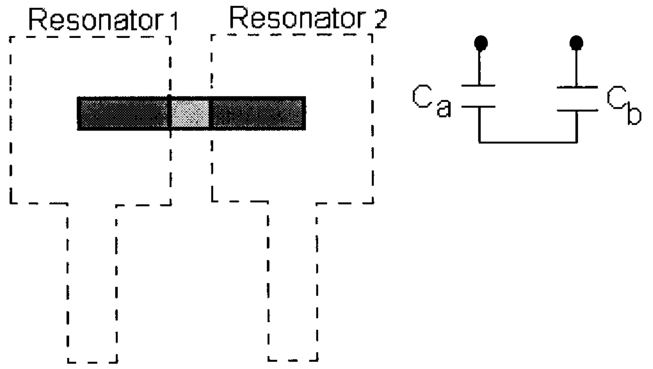

Figure 6.4 Model to calculate the inter-resonator capacitance C_i.

6.2.3 Source-Load Capacitance

This capacitance can be estimated by even and odd mode analysis of edge-coupled striplines [6] as shown in Fig. 6.5. The total capacitance between the coupled lines is

$$C_{12} = \frac{C_o - C_e}{2} l_{eq} \tag{6.8}$$

where C_e and C_o are the even and odd mode capacitances [6], respectively, and l_{eq} is the total length of the edge-coupled lines including fringing fields.

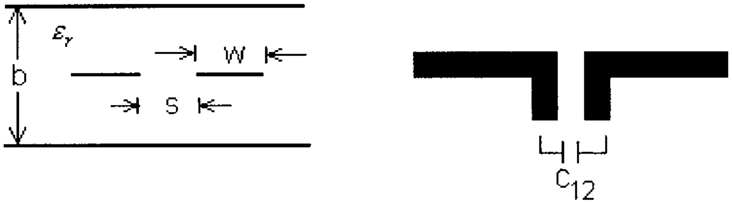

Figure 6.5 Model to calculate the source-load capacitance C_{12}.

6.2.4 Capacitance Between Source and Resonator 2 - Resonator 1 and Load

The model to compute C_x is the offset-coupled stripline as shown in Fig. 6.6. The expression for C_x is identical to (6.8), but the even and odd mode capacitances are computed from the conformal mapping method in [35]. Design expressions can be found in the Appendix.

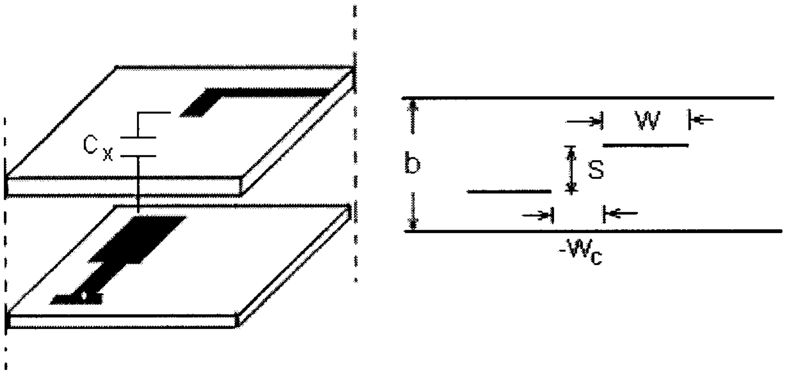

Figure 6.6 Model to calculate the capacitances between source and resonator 2 as well as Resonator 1 and load.

Since this technique holds only for striplines of identical width, we are applying, for simplicity, the average width between the feed line and the resonator. l_{eq} is that part of the length of the feed line which is parallel to the resonator and includes fringing fields.

6.3 Results

In order to validate the simplified theory and demonstrate its applicability towards the design of miniaturized LTCC filters, the results of this analysis are compared with measurements presented in [32].

Figs. 6.7 and 6.8 compare the measurements of Fig. 7a,b of [32] with the results obtained with our method. For the dimensions given in [32], this method predicts performances, which are in good agreement with the measurements in [32], for the two cases showing an attenuation pole below (Fig. 6.7) and above (Fig. 6.8) of the passband.

These comparisons verify the simplified approach presented here.

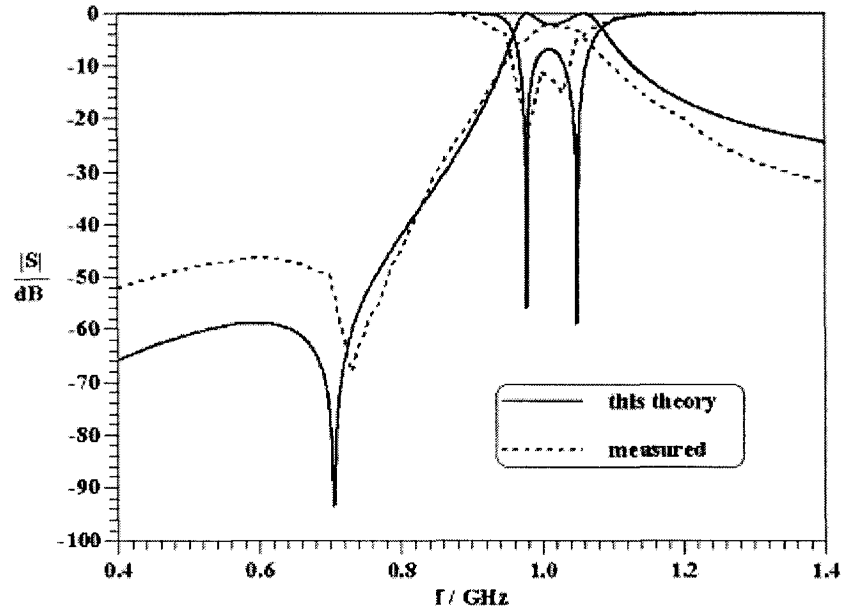

Figure 6.7 Comparison between this theory and measurements [32] for a LTCC filter with an attenuation pole below the passband.

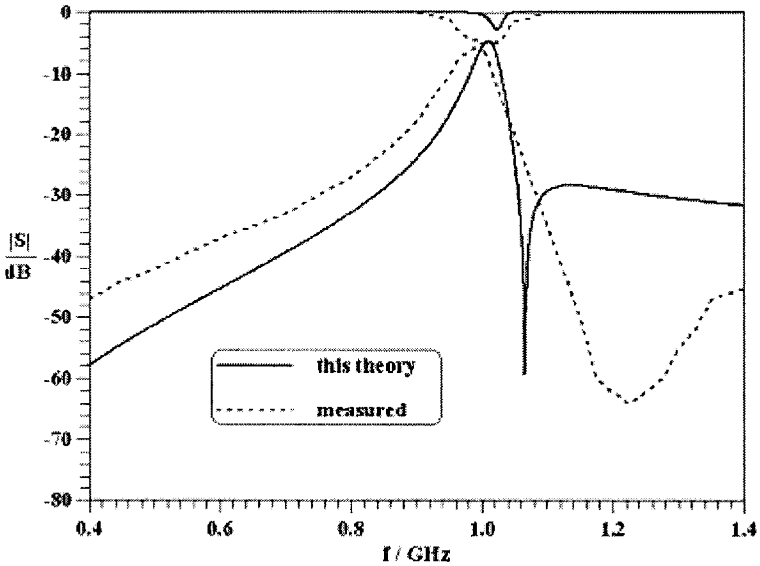

Figure 6.8 Comparison between this theory and measurements [32] for a LTCC filter with an attenuation pole above the passband.

6.4 Design

We now apply this theory towards the design of the LTCC filter shown in Fig. 6.1. The center frequency is 945 MHz with attenuation poles at 620 MHz and 1.1 GHz. The dielectric material has ε_r=58 and a total thickness of b=1.6mm as shown in Fig. 6.1. The dimensions are:

Layer #1 (inter-resonator coupling strip):

Width 0.2 mm, length 1.6 mm

Layer #2 (SIR coupled lines):

High-impedance section:

Length 3.2mm, width 0.35 mm, gap 1.2 mm

Low-impedance section:

Length 3.2mm, width 1.55 mm, gap 0.2 mm

Layer #3 (L-shaped input/output pads, c.f. Fig. 6.3):

Length for C_a: 1.3 mm, length for C_b: 0.5 mm.

Widths of pads: 0.2 mm
Gap between pads: 0.3 mm.

These dimensions lead to the following parameters calculated from the theory: Z_{e1}=20Ω, Z_{o1}=18.6Ω, Z_{e2}=10Ω, Z_{o2}=7Ω, C_1=C_2 =2.1pF, C_i=(-)0.421pF, C_{12}=(-)0.317pF, C_x=(-)0.52PF. (Note that the negative signs in parentheses represent negative coupling values; the actually calculated capacitances are positive, e.g. [33]). This data results in the performance shown in Fig. 6.9 (theory), which is compared to solutions by the commercially available field solvers IE3D® and Ansoft Designer®. Very good agreement is obtained. Slight differences were to be expected because of the simplicity of the model. The passband computed by the field solvers is narrower due to losses up to 3 dB. We attribute these losses to accessory electromagnetic coupling not included in the simplified theory. The level of attenuation in the stopband matches with our theoretical predictions and presents an improvement compared to the design of [34]. The locations of attenuation poles are predicted very well.

Both IE3D® and Ansoft Designer® are MOM-based codes. Therefore, we expect identical solutions in Fig. 6.9. However, the implementation of algorithms for faster solutions differs, thus leading to different performance evaluations.

Since the CPU time is in extreme favor of the method presented in this chapter (instant response versus appr. 30 min with IE3D® and Ansoft Designer® for 100 frequency samples), it can be used to obtain a fast and reasonably accurate initial design. A fine optimization may then be performed with full-wave solvers.

6.5 Conclusions

The simplified analysis technique is a viable option for the design of capacitively coupled LTCC resonators. The individual capacitances introduced with this model account for the large majority of coupling effects between all elements of the filter. The theory compares well with previously published measurements. A new filter configuration with attenuation poles on either side of the passband is initially designed and compares well with the results of field solvers. It also presents a stopband improvement over similar state-of-the-art LTCC filters.

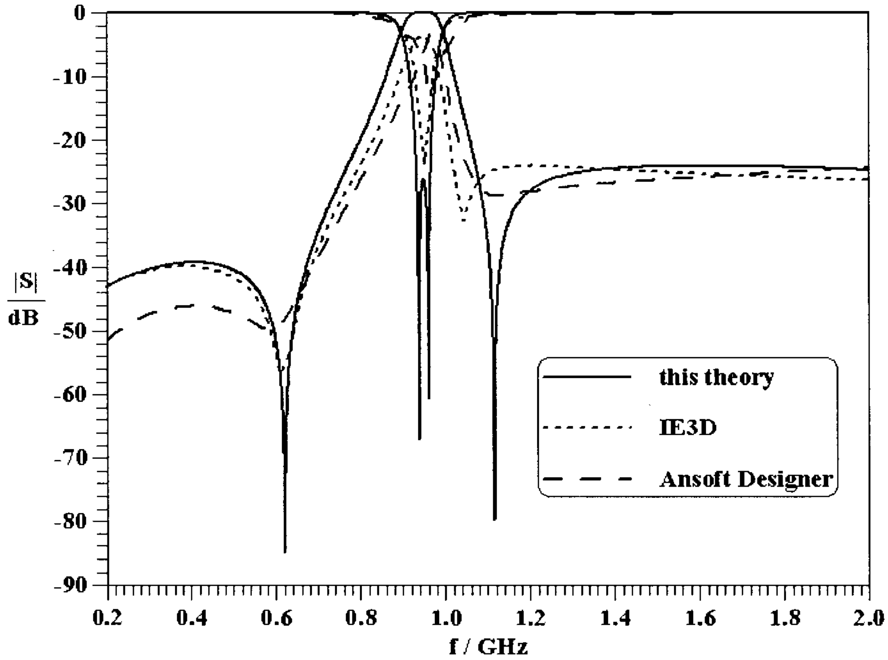

Figure 6.9 Comparison between results of simplified analysis and commercially available field solvers for a design according to Fig. 6.1.

Chapter-VII

7 Quasi-Static Analysis of Circular Signal Tapping Pads

Introduction

Microstrip circuits invariably incorporate transmission line discontinuities of one type or another. The effect of these discontinuities is predominant at microwave frequencies. In high-density RF circuits, it is important to estimate the influence of the discontinuities so that RF noise can be controlled. Some of the common forms of microstrip discontinuities are open ends, gaps [36], steps in width, right angled bends [37], T-junctions and cross-junctions [38]. Since discontinuity dimensions are usually much smaller than the guided wavelength, they may be modeled quasi-statically as lumped element equivalent circuits, e.g., [12].

Other important discontinuities in the RF circuit are signal tapping pads and DC biasing pads. Generally, these pads are isolated from the ground, as shown in Fig. 7.1, and will introduce capacitive reactance to an RF circuit. The field in the slot, between the pad and ground, can cause (very small) radiation. In high-speed circuits, the capacitance of the pads will create a time delay for signal propagation and, therefore, the capacitance created by the pads must be known in order to design compensatory circuits to overcome time delays. Since displacement currents dominate the conduction currents, cutting slots into the pads will not reduce their reactance. Therefore, and in combination with lumped inductors, filter sections can be designed using tapping pads.

The quasi-static evaluation of the open-end discontinuity capacitance has been treated in [36]. In this chapter, we present the quasi-static analysis for the capacitance of a DC biasing pad.

7.1 Formulation

If the substrate height h is small (c.f. Fig. 7.1), the voltage between the pad and the ground plane is uniform with respect to the radial direction r in region I ($0<r<a$). It depends on the z direction only. In the slot, region II ($a<\mathrm{r}<d$), the potential function satisfies Laplace's equation

$$\nabla^2 V = 0 \tag{7.1}$$

with boundary conditions

$$V=V_0 \quad \text{at } r=a \text{ and } z=h \tag{7.2a}$$

$$V=0 \quad \text{at } r=d \text{ and } z=h \tag{7.2b}$$

$$V=0 \quad \text{for all } r \text{ and } z=0 \tag{7.2c}$$

Due to the symmetry, the angular variable ϕ can be neglected, and the general solution to (7.1) is

$$V(r,z) = [b_1 I_0(\lambda r) + b_2 K_0(\lambda r)] \cdot [c_1 \cos(\lambda z) + c_2 \sin(\lambda z)] \tag{7.3}$$

where b_1, b_2, c_1 and c_2 are amplitude constants, which can be eliminated by using the boundary conditions (7.2a) to (7.2c); K and I are modified Bessel functions.

Since the solution for the potential in the region II is

$$V_2(r,z) = V_0 \left[\frac{I_0(\lambda d)K_0(\lambda r) - K_0(\lambda d)I_0(\lambda r)}{I_0(\lambda d)K_0(\lambda a) - K_0(\lambda d)I_0(\lambda a)} \right] \frac{\sin(\lambda z)}{\sin(\lambda h)}, \tag{7.4}$$

where $\lambda = \pi/(2h)$, the electric field in region II can be written as

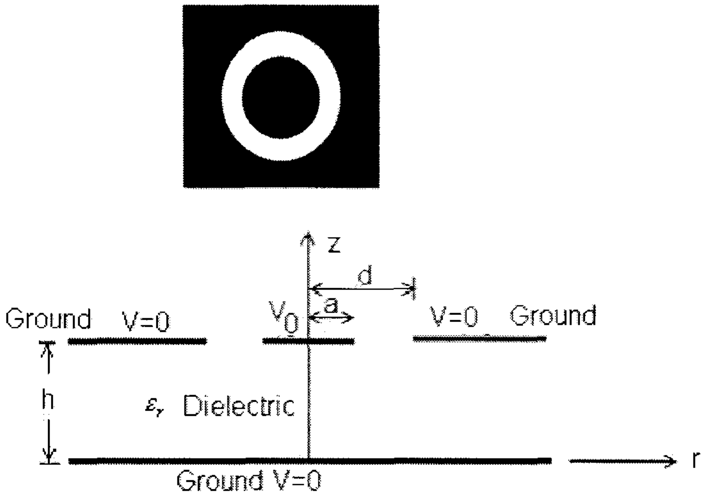

Figure 7.1 Top view and cross section of circular signal/DC tapping pad

$$E_2(r,z)=\frac{V_0\lambda}{\sin(\lambda h)}\left\{\frac{I_0(\lambda d)\left[K_1(\lambda r)\sin(\lambda z)-K_0(\lambda r)\cos(\lambda z)\right]}{I_0(\lambda d)K_0(\lambda a)-K_0(\lambda d)I_0(\lambda a)}-\frac{K_0(\lambda d)\left[I_1(\lambda r)\sin(\lambda z)-I_0(\lambda r)\cos(\lambda z)\right]}{I_0(\lambda d)K_0(\lambda a)-K_0(\lambda d)I_0(\lambda a)}\right\} \tag{7.5}$$

Similarly, the voltage and electric field in region I are $V_1=V_0 z/h$ and $E_1=-V_0/h$. From the energy stored in the structure

$$W=\frac{1}{2}CV_0^2=\frac{1}{2}\varepsilon\int_v |E|^2 dv \tag{7.6}$$

the capacitance of the pad can be derived as

$$C=\varepsilon\frac{\pi a^2}{h}+\frac{2\pi\varepsilon}{V_0^2}\int_{r=a}^{d}\int_{0}^{h} r|E_2|^2 ds \tag{7.7}$$

7.2 Results

For an example of a=4mm, h=2mm, ε_r=10 and three parameters of the outer pad radius, d, Fig. 7.2 shows the electric-field variation in radial direction (region II) at height $z=h$. While it is obvious from (7.4) that the potential between the two ground planes at $r=d$ vanishes, Fig. 7.2 demonstrates that this is not the case for the electric field in (7.5) due to the non-zero voltage gradient (e.g., d=5mm and 6mm in Fig. 7.2). Only if the slot width increases in radial direction (d=8mm), then the field at $r=d$ decreases as expected.

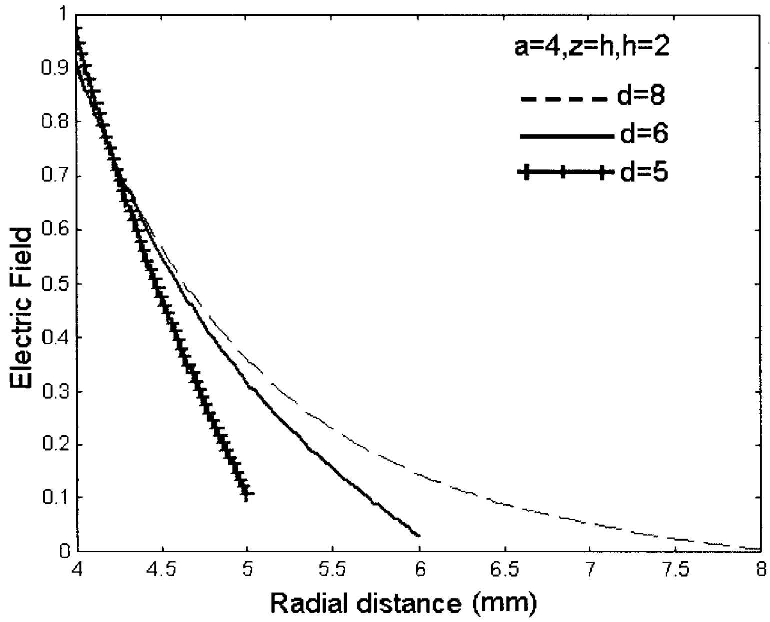

Figure 7.2 Variation of the electric field in region II at z=h for d = 8, 6 and 5 mm.

Fig. 7.3 displays the electric field at half the distance between the lower and upper ground plane ($z=h/2$) for the three different slot gaps d. This confirms the presence of an electric field between the two ground planes.

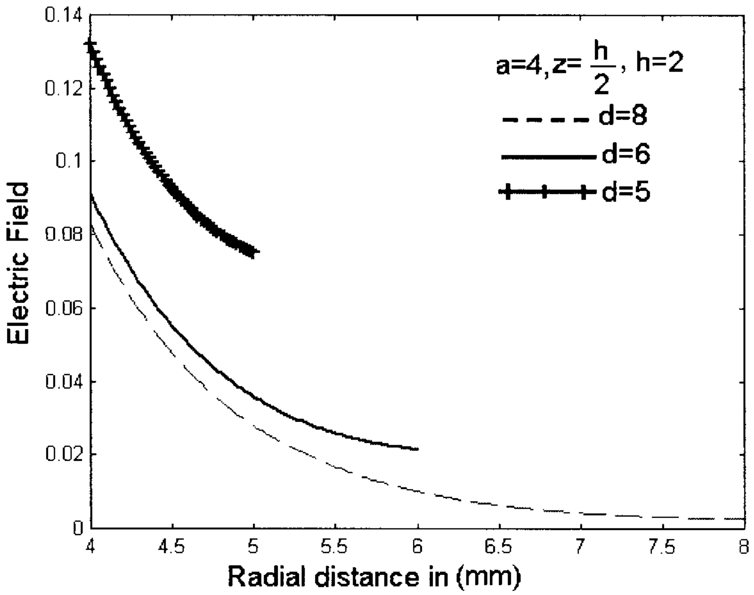

Figure 7.3 Variation of the electric field in region II at z=h/2 for d = 8, 6 and 5 mm.

In Table 7.1, the analytical quasi-static formula (7.7) is compared with numerical results obtained with the commercial EM simulator IE3D, version 9. The capacitance is derived from the impedance parameters calculated from IE3D by defining the port against the pad. Good agreement between the quasi-static approach and IE3D is demonstrated up to 3 GHz. A similar comparison was carried out for the range of dimensions. It is concluded that the capacitance is accurately predicted as long as $h/a < 1.5$, even if h/d is as high as 10. If $h/d < 0.5$, then the model works very well up to $h/a = 2$. The variation with respect to the substrate material is shown in Table 7.2 and demonstrates very good agreement for permittivities up to 13. Impedance values obtained with IE3D and with the quasi-static theory are compared in Fig. 7.4. The dimensions are: a=1.4mm, h=0.8 mm, gap width d-a= 0.6mm and ε_r=10. Very good agreement is demonstrated. As for comparison of CPU times with IE3D, it depends on how large a ground plane is chosen surrounding the pad and how many via holes are selected to actually connect that plane to the lower (infinite) ground plane (c.f. next example). On the average, the quasi-static formulation (7.7) has been at least three times faster than IE3D.

Finally, the capacitance calculation according to (7.7) is used in a circuit design problem. We focus our attention on obtaining an initial design for a fifth-order lowpass filter at 3 GHz. Lumped-element capacitances and inductances are readily calculated from standard filter theory. We then use (7.7) to determine parameters a and d in order to match the theoretical capacitance values with those of the practical pads. The circuit is shown in Fig. 7.5. The area around the pads is grounded through via holes, and the inductors are mounted within the elevated strip line. The vertical bends of the strip line were included in the EM simulation (using the commercial package MEFiSTo-3D) but not in the filter design process.

Table 7.1

Comparison of capacitance (in pF) obtained with this theory and IE3D for varying gap width. a=1mm, h=0.8mm, ε_r=10.

Gap (mm)	This Theory	IE3D 0.5GHz	IE3D 1 GHz	IE3D 2 GHz	IE3D 3 GHz
0.2	0.76	0.74	0.73	0.75	0.78
0.4	0.67	0.67	0.67	0.69	0.70
0.6	0.63	0.61	0.63	0.65	0.68
1.0	0.62	0.60	0.63	0.64	0.68
3.0	0.60	0.63	0.63	0.65	0.67
5.0	0.59	0.63	0.63	0.65	0.67

Table 7.2
Comparison of capacitance (in pF) obtained with this theory and IE3D for varying permitivity. a=1mm, d=1.2mm, h=1.0mm.

Material	ε_r	This theory	IE3D 1 GHz	IE3D 2 GHz
PTFE	2.35	0.16	0.19	0.19
Quartz	3.8	0.27	0.28	0.29
GaAs	13.13	0.91	0.87	0.90
InP	12.61	0.88	0.85	0.86
HighRes. Silicon	11.8	0.81	0.81	0.82
Alumina	9.9	0.69	0.66	0.68

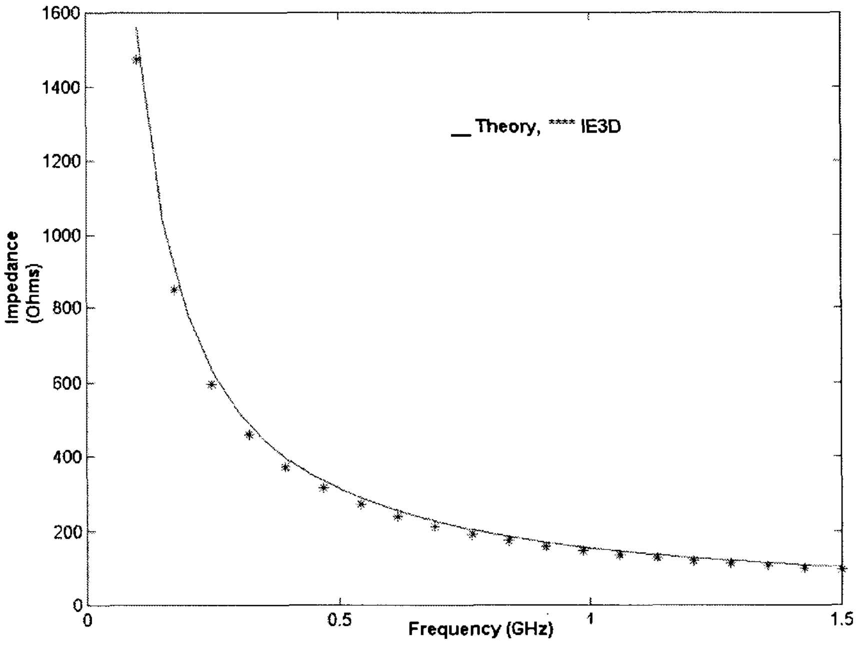

Figure 7.4 Impedance of the pad; comparison between this theory and IE3D.

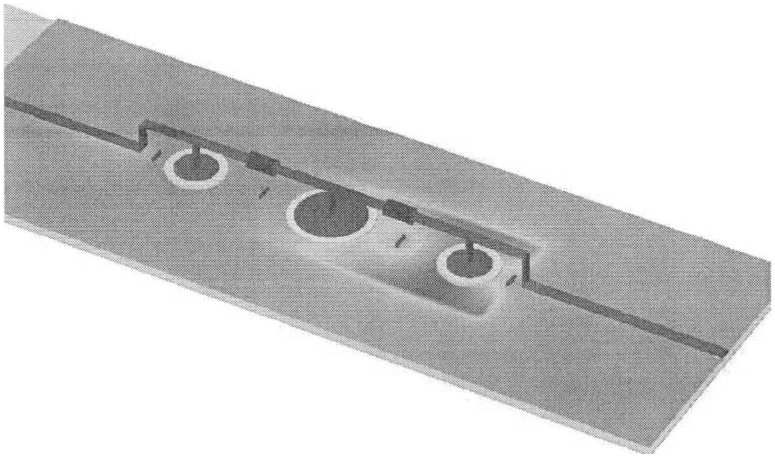

Figure 7.5 Lowpass filter designed with quasi-static approach of tapping pads.

The performance of this filter is depicted in Fig. 7.6. The dashed lines show the results of a circuit-based simulation (ADS) using the capacitances extracted from (7.7). The solid lines are obtained from a full-wave electromagnetic field solver (MEFiSTo-3D) and show a minimum return loss of 13 dB and 20 dB rejection between 5.2 GHz and 12 GHz. Note that the cutoff frequencies calculated with both methods are in good agreement which verifies the capacitance calculations via (7.7). Although this is not (and was not meant to be) a final design, it clearly demonstrates the value of the quasi-static theory in dealing with the capacitances of circular signal tapping pads.

7.3 Conclusions

A simple analytical expression for the capacitance of circular signal tapping pads is derived using a quasi-static analysis. The theory is validated by analysis of the pads with the commercial software package IE3D. Very good agreement is demonstrated. The quasi-static analysis is applied to the design of a new lowpass filter, which combines the signal tapping pads with lumped inductors. Its performance simulation demonstrates the value of the quasi-static theory in dealing with initial design problems involving the capacitances of circular signal tapping pads.

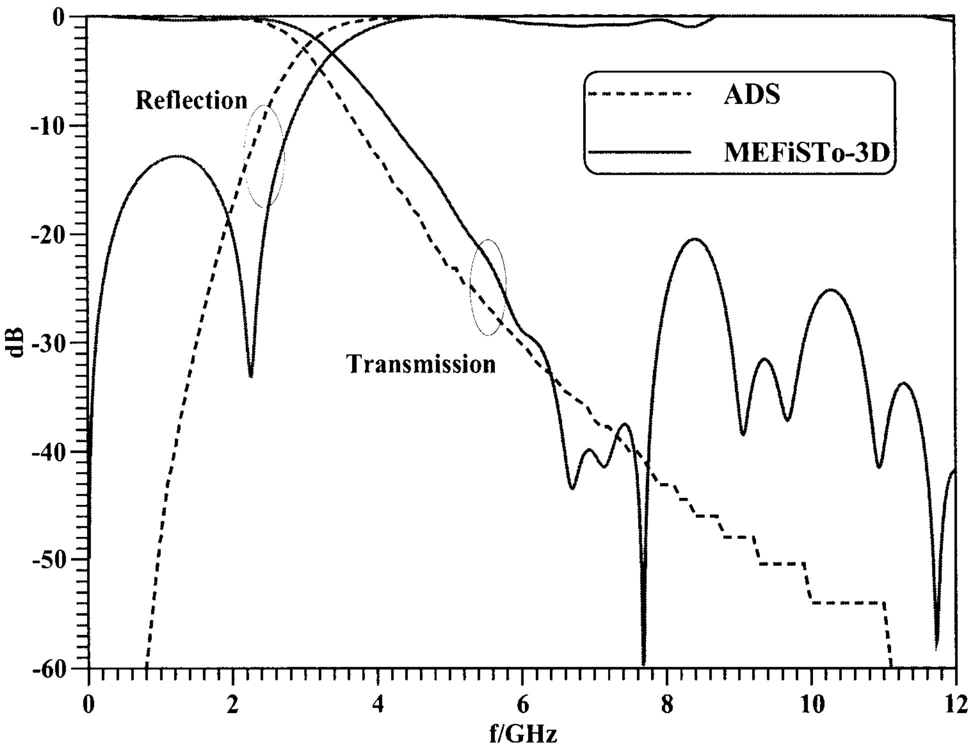

Figure 7.6 Performance of initial design of lowpass filter using tapping pads. Circuit-based (dashed lines) vs. EM-based (solid lines) simulation.

Chapter-VIII

8 Equivalent Circuit Model for Electromagnetic Band Gap Structures

Introduction

Recent advances and applications of Electromagnetic Band-Gap (EBG) structures have proven that the excitation of surface waves can be considerably reduced. Especially with respect to patch antennas, it was demonstrated that their performance could be improved by utilizing additional printed periodic structures, which create a stopband within the particular frequency range of operation. Several types of microstrip-based EBG structures have been proposed for a variety of applications, e.g. [39], and were analyzed and designed by using numerical techniques such as the finite-difference time-domain [40] and the finite-element method [41].

However, commercially available software packages based on rigorous numerical techniques are, in general, not well suited for a quick design of EBG structures. They are time consuming and/or memory intensive and often allow analysis of only a very limited number of cells as opposed to the true periodic structure. Therefore, equivalent-circuit methods have been developed in order to quickly design EBG structures for desired pass- and stopbands. One of these techniques was presented in [42] for applications to via-holed patches. In applying the related formulation, however, it was found that the first stopband, which is certainly considered for compact printed-circuit antenna designs, could not be predicted.

This chapter introduces an improved analytical method with a goal to develop a simple (yet accurate) and quick design tool for EBG's. Based on equivalent circuits and transmission line theory, the model will be shown to predict the first stopband and be in reasonable agreement with commercial field solvers as far as attenuation over a limited number of cells is concerned. As an application-oriented example, this model is then used to enhance the performance of a microstrip patch antenna similar to [43].

8.1 Analytical Model

Fig. 8.1 shows the schematic diagram of the EBG lattice [42] and its essential dimensions. A square metal sheet connected to the continuous ground plane through a via hole or thin wire [44] constitutes the unit cell of the lattice. This circuit can be treated as arrays of reactively loaded resonators coupled by gap capacitances. The resonant frequency below the half-wavelength resonance results from the reactive loading of the microstrip resonator. At resonance very little energy propagates along the structure.

The dominant surface wave in most practical microstrip patch antennas on a grounded dielectric substrate is the transverse magnetic mode. Using transmission line theory, an equivalent circuit as shown in Fig. 8.2 represents each unit cell of the lattice. (Note that contrary to [42], Fig. 8.2 includes the EBG's left and right edge coupling.) The centrally located shorting posts in Fig. 8.1 are represented by an inductive reactance X_l, resulting from the inductance [45]

$$L = \frac{\mu_0}{\pi} t \left[\ln\left(\frac{4t}{d}\right) + 0.5\left(\frac{d}{t}\right) - 0.75 \right] \tag{8.1}$$

where t and d are the length and diameter of the pin, respectively. The coupling between the unit cell and its immediate neighbors is represented by a capacitive reactance X_c, resulting from the coupling capacitance [45]

$$C = \frac{W\varepsilon_0\left(\varepsilon_{r1} + \varepsilon_{r2}\right)}{\pi} \cosh^{-1}(a/g) \tag{8.2}$$

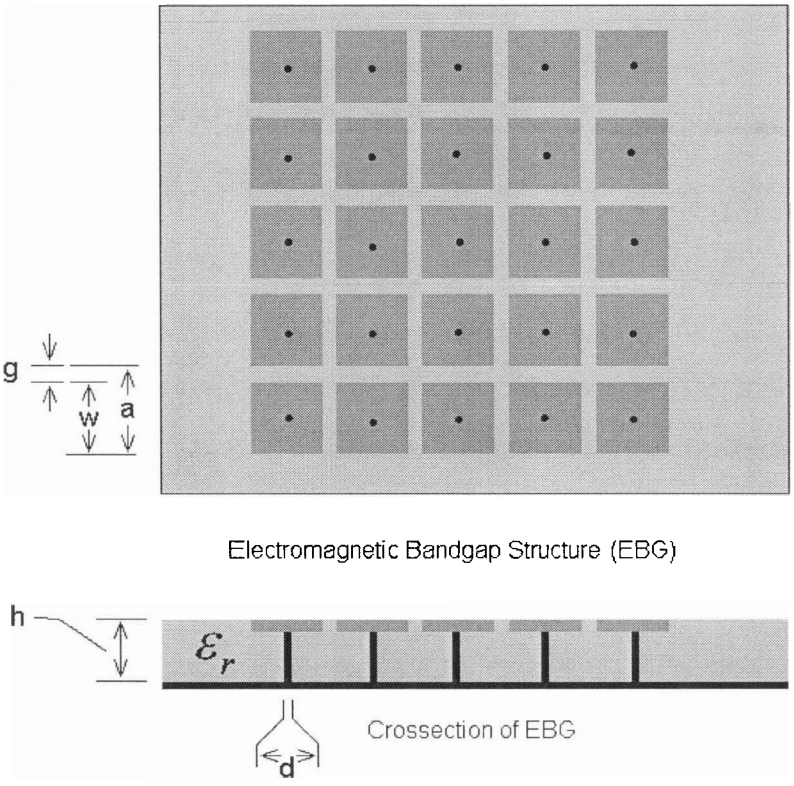

Figure 8.1 Schematic diagram of the EBG structure.

where ε_{r1} and ε_{r2} are the dielectric constants of the materials above and below the resonators and a, W, g are the dimensions shown in Fig. 8.1. The gap between two unit cells is represented by a capacitive Π-section [46] with C_g and C_p in Fig. 8.2 calculated using [37] – as is the fringing field due to the gap width Δl_g. As long as $w/h>2$, the pad can be analyzed as a microstrip line with characteristic impedance Z_0 and propagation constant β_m, both determined from the effective dielectric constant given in [47].

For the circuit shown in Fig. 8.2, the voltages and currents on either side of the nth unit cell are related through the ABCD matrix

$$\begin{bmatrix} V_n \\ I_n \end{bmatrix} = \begin{bmatrix} A & B \\ C & D \end{bmatrix} \begin{bmatrix} V_{n+1} \\ I_{n+1} \end{bmatrix} \tag{8.3}$$

The entries of the matrix follow from combining a transmission line section of length *a* with a series impedance Z_c (Fig. 8.2)

$$\begin{aligned}\begin{bmatrix} A & B \\ C & D \end{bmatrix} &= \begin{bmatrix} \cos(\beta_m a) & jZ_0 \sin(\beta_m a) \\ jY_0 \sin(\beta_m a) & \cos(\beta_m a) \end{bmatrix} \begin{bmatrix} 1 & Z_c \\ 0 & 1 \end{bmatrix} \\ &= \begin{bmatrix} \cos(\beta_m a) & Z_c \cos(\beta_m a) + jZ_0 \sin(\beta_m a) \\ jY_0 \sin(\beta_m a) & jZ_c Y_0 \sin(\beta_m a) + \cos(\beta_m a) \end{bmatrix}\end{aligned} \tag{8.4}$$

where Y_0 is the characteristic admittance of the microstrip pad.

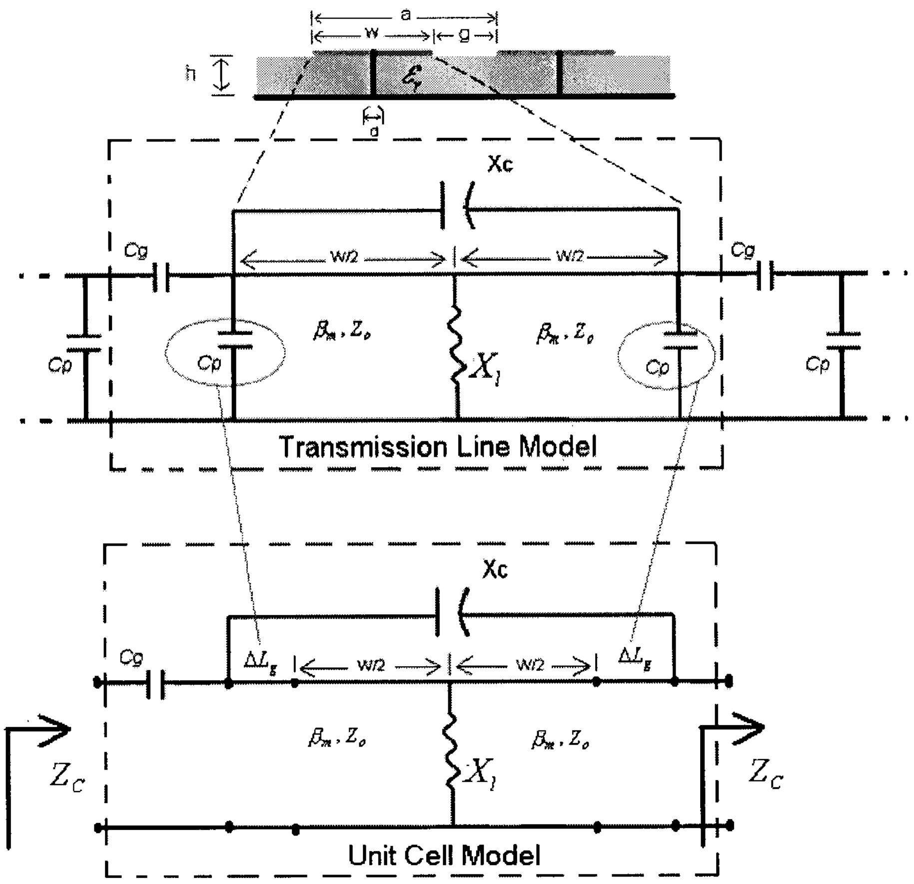

Figure 8.2 Transmission-line model of the unit cell.

Since the structure is periodic, the voltages and currents at the *n*th terminal differ from those at the *n+1*-th terminal by the propagation factor $\exp(-\gamma a)$. Therefore, using this condition in (8.3), the characteristic equation for non-trivial solutions is

$$AD + e^{2\gamma a} - (A + D)e^{\gamma a} - BC = 0 \tag{8.5}$$

Since the circuit is passive and reciprocal, *AB-CD* = 1. With $\gamma = \alpha + j\beta$, (8.5) is rewritten as

$$\begin{aligned} &\cosh(\alpha a)\cos(\beta a) + j\sinh(\alpha a)\sin(\beta a) = \\ &\qquad = \cos(\beta_m a) + j\frac{Z_c}{2Z_0}\sin(\beta_m a) \end{aligned} \tag{8.6}$$

Assuming a passband without conductor or dielectric losses (α=0), we get

$$\beta = \frac{1}{a}\cos^{-1}\left(\cos(\beta_m a) + j\frac{Z_c}{2Z_0}\sin(\beta_m a)\right) \tag{8.7}$$

Alternatively, we can assume a stopband exhibiting no propagation ($\beta = 0$)

$$\alpha = \frac{1}{a}\cosh^{-1}\left(\cos(\beta_m a) + j\frac{Z_c}{2Z_0}\sin(\beta_m a)\right) \tag{8.8}$$

In order to relate the attenuation constant for the periodic structure, *a*, to the actual attenuation S_{21} introduced by a finite number of cells, *N*, we employ a relationship introduced in [48] and verified in [49]

$$S_{21}/dB = -8.686N\alpha p \tag{8.9}$$

where p=a is the length of one cell.

8.2 Results

Both models (the one in [42] and the one presented above) were implemented in simple Matlab and/or Fortran routines. (Note that we added the calculation of the attenuation constant to the model in [42].)

As a direct comparison between the two models, Fig. 8.3a depicts the propagation constants calculated from this approach and compares it to results using the model in [42]. Both methods predict a number of passbands, which agree to a certain extent. But the main difference is the behavior towards lower frequencies. While the method in [42] (light curves) predicts a wide passband of varying propagation constant β (light solid line), our results (dark curves) clearly indicate a stopband with attenuation constant α (dark dashed line) up to appr. 2.6 GHz. A similar behavior is observed in the second stopband between 3 GHz and 5 GHz.

In order to make a decision as to whether a stopband in the lower frequency range exists, our attenuation data is compared with results from commercially available software packages. An array of 5x5 cells was analyzed by Ensemble® and IE3D® and, in Fig. 8.3b, compared to our attenuation values obtained from (8.9). Of course, agreement in the higher frequency range cannot be expected since the transmission-line models are restricted to the validity of the elements of the equivalent circuit in Fig. 8.2. However, both commercial software packages clearly predict a stopband up to 2 GHz, and the passband computed with the approach presented here falls in between those predicted with Ensemble® and IE3D®. This confirms the existence of the stopband and the validity of our simplified approach over a wider frequency range than that of [42].

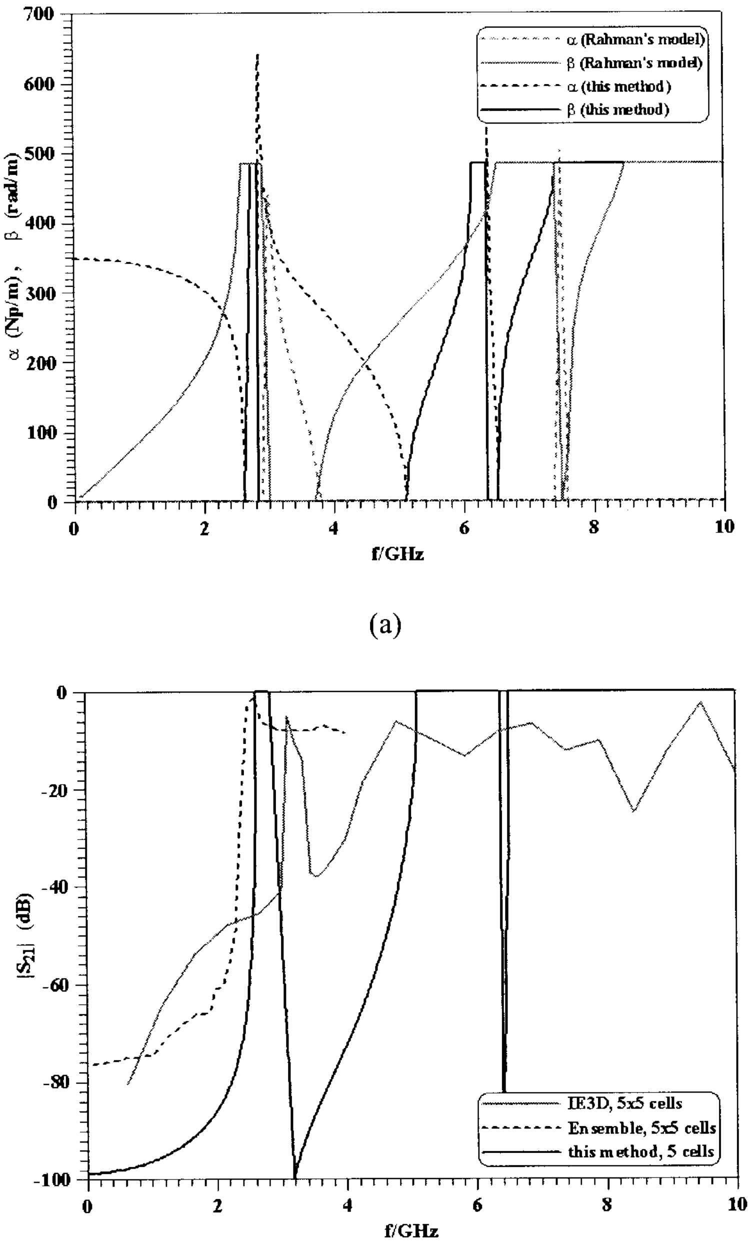

(a)

(b)

Figure 8.3 Comparison of propagation characteristics; (a) this model using (8.7), (8.8) (dark curves) and the model in [42] (light curves); (b) this model using (8.9) (dark solid curve), Ensemble (light dashed) and IE3D (light solid) results of a five-cell structure. Dimensions (c.f. Fig. 8.1): w=6.0mm, g=0.5mm, a=6.5mm, d=1.0mm, h=2.54mm, ε_r=10.2.

Fig. 8.4 shows the performance of an EBG structure with wider stopband performance. In comparison with the configuration in Fig. 8.3, the permittivity is reduced and the patches as well as the substrate height increased. For a 3x3 array, our S_{21} data is compared to results from IE3D, and very good agreement is observed. The slight ripple in the passband of the IE3D calculation is attributed to reflections within the small number of cells. They should weaken once a higher number of cells is considered, which was not possible in this investigation since 4x4 cells resulted in uncorrelated results from IE3D.

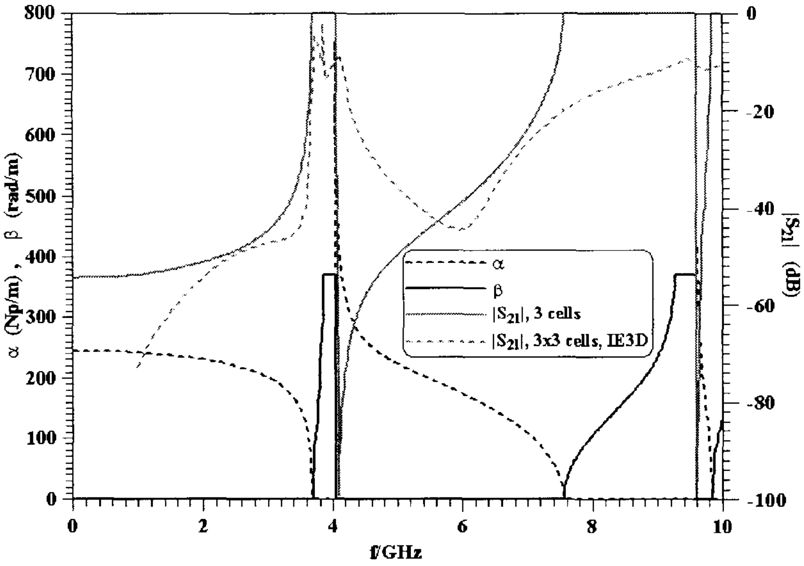

Figure 8.4 Propagation characteristics using this model (8.7), (8.8) (dark curves); comparison of transmission behavior: IE3D with 3x3 cells (light dashed line), this model using (8.9) (light solid line). Dimensions (c.f. Fig. 8.1): w=8.0mm, g=0.5mm, a=8.5mm, d=1.0mm, h=3.175mm, ε_r=2.35.

Our final example uses dimensions appropriate for fabrication in LTCC technology. Fig. 8.5 presents the propagation characteristics and a comparison of transmission behavior with IE3D. Good agreement is again observed except for the passband ripple in the IE3D data. Note that only a single passband exists up to 10 GHz and that, according to our computations, only two cells provide an attenuation of 60 dB up to 4 GHz.

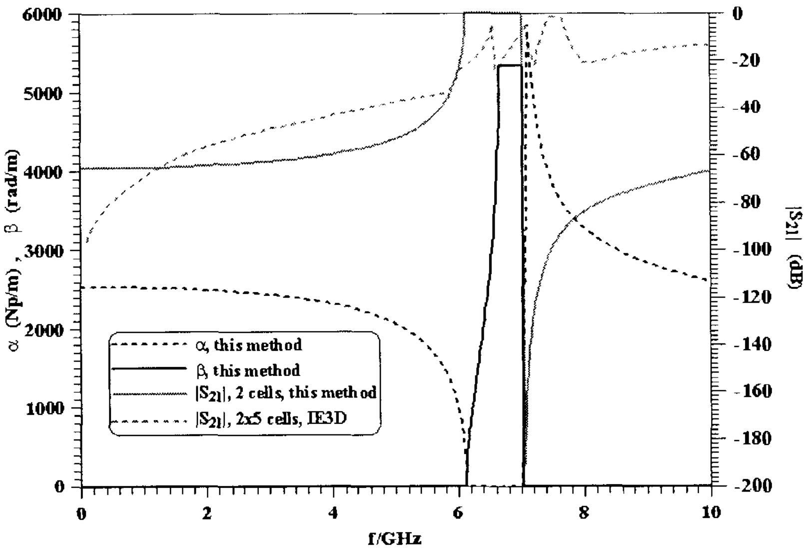

Figure 8.5 Propagation characteristics using this model (8.7), (8.8) (dark curves); comparison of transmission behavior: IE3D with 3x3 cells (light dashed line), this model using (8.9) (light solid line). Dimensions (c.f. Fig. 8.1): w=0.54mm, g=0.05mm, a=0.59mm, d=0.05mm, h=0.8mm, ε_r=58.

8.3 Application

Two lines of cells of the EBG structure investigated in Fig. 8.3 were used to improve the performance of a patch antenna operating at 1.575 GHz in right-hand circular polarization (c.f. Fig. 8.6). Indeed for this application, the substrate thickness is small, and the level of surface-wave excitation at this frequency should be insignificant. According to [50], however, if $h \leq \lambda/20$, the power ratio of surface waves to space waves can be estimated by

$$\frac{P_{surface}}{P_{space}} = \pi^2 \frac{(\varepsilon_r - 1)^3 \frac{h}{\lambda_0}}{\frac{2}{3}\varepsilon_r^2(\varepsilon_r - 1) + \frac{4}{15}\varepsilon_r} \tag{8.10}$$

which, in this case, amounts to 16 percent. As far as the existence of surface waves is concerned, this result principally agrees with the investigation in [51].

Due to the manufacturing process and for a direct comparison between computed and measured results, the ground plane size of the antenna in Fig. 8.6 was chosen as 150 mm square [52]. The performance improvement due to the EBG structure is demonstrated in Figs. 8.7, 8.8, and 8.9. These results were acquired from simulations using Ensemble® 5.0.

Fig. 8.7 depicts the gain performance. Some improvement in bandwidth is observed but only very little in gain. It is expected that a difference in gain levels will become more noticeable with the use of a more realistic (smaller) ground plane. The improvement in axial ratio is shown in Fig. 8.8. Fig. 8.9 demonstrates through measurements that the return loss bandwidth is increased by the EBG structure. However, the measured return loss is only 13 dB compared to a computed value of 20 dB. The main source of this discrepancy is attributed to the coaxial connector soldered to the antenna through the substrate. The pin diameter was assumed to be 0.5 mm, which was not available at the time of measurement. A connector with a diameter of 1.1 mm had to be used instead.

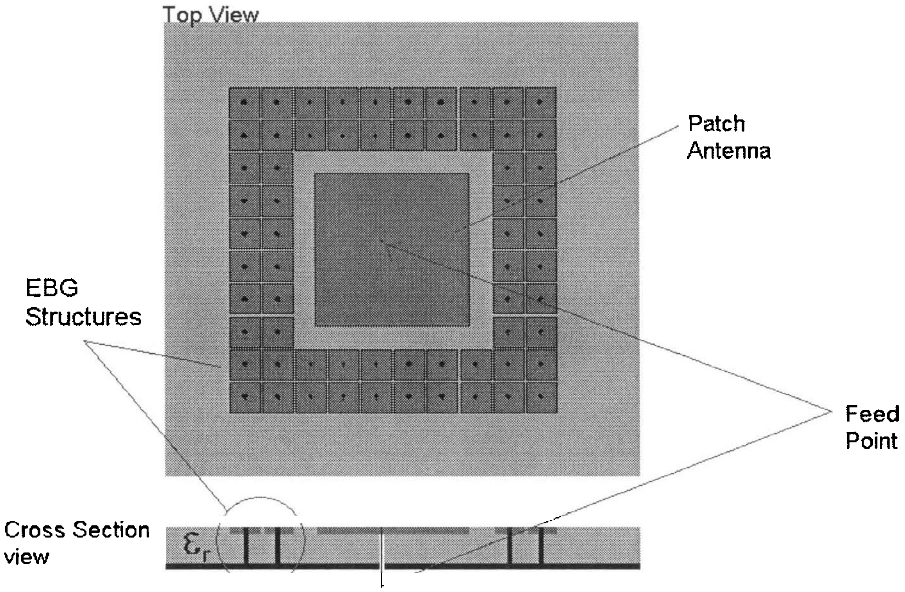

Figure 8.6 Schematic of the patch antenna with EBGs.

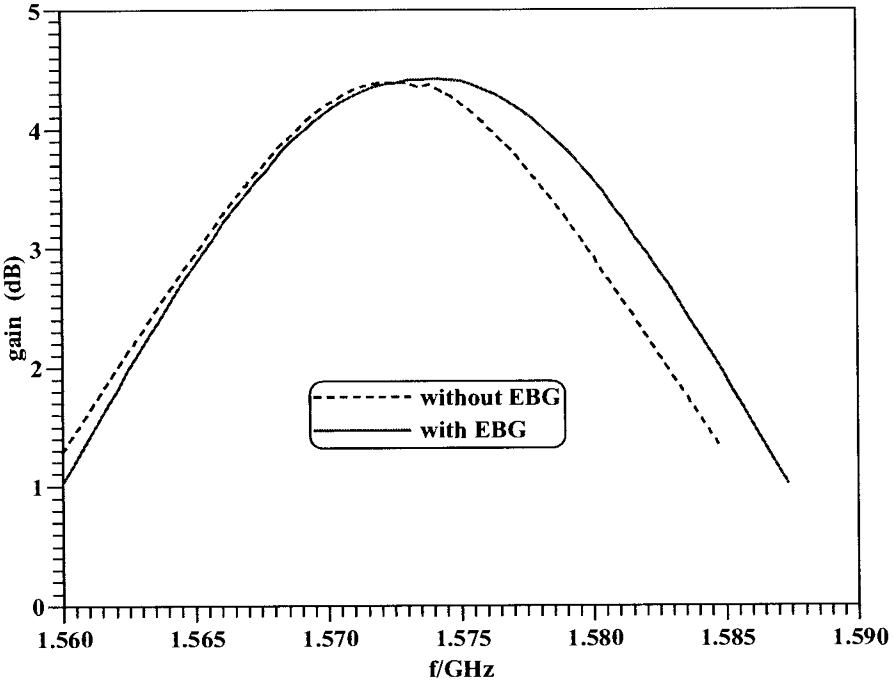

Figure 8.7 Gain of the antenna

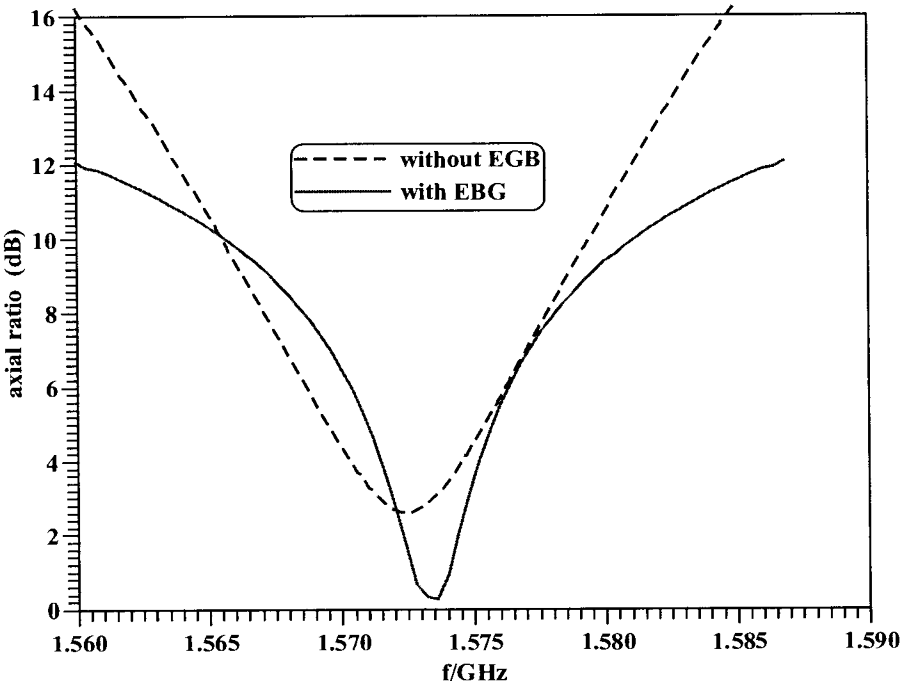

Figure 8.8 Axial ratio of the antenna

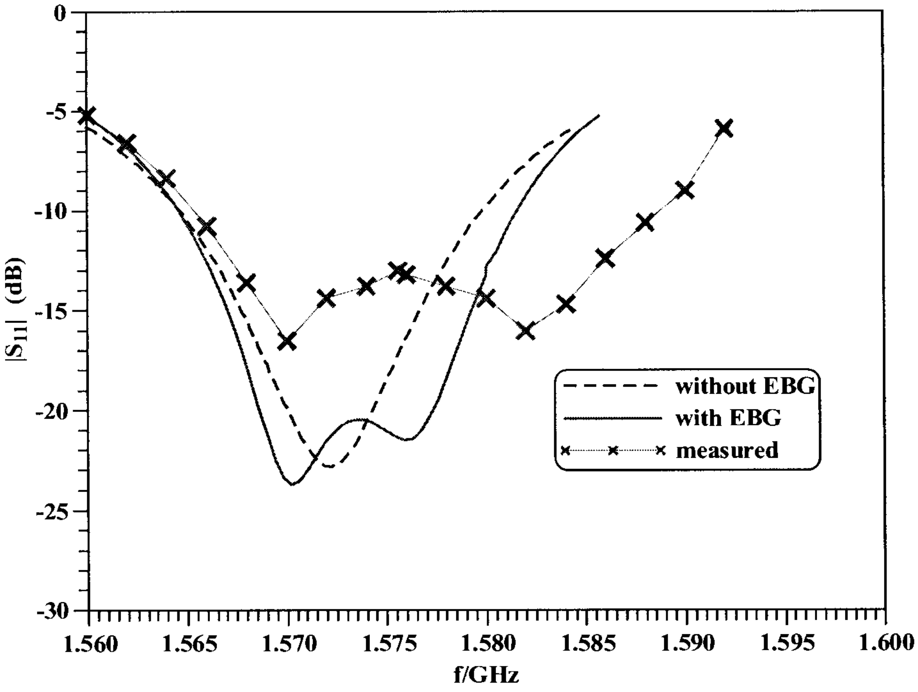

Figure 8.9 Return loss of the antenna

8.4 Conclusions

The simple and improved equivalent-circuit model presents a viable approach for the analysis and design of EBG structures formed by via-holed patches. The first stop- and passbands are correctly predicted as verified by comparison with independent numerical codes. A prototype antenna design based on this model is shown to have superior computed axial-ratio and measured return-loss-bandwidth performance compared to a patch antenna without EBG configurations.

Chapter-IX

9 Conclusions

9.1 Discussion

Any microwave problem involves electromagnetics and the application of Maxwell's equations for its solution. But analytical solutions for complex microwave structures are difficult to obtain. Numerical techniques are very accurate for the analysis of electromagnetic problems and, therefore, can be used very effectively as analysis tools [53]. In order to synthesize or initially design a microwave component or system, however, numerical methods are often limited to trial-and-error approaches.

Design methods, which combine numerical techniques and optimization, require extensive computer resources, both in terms of memory and CPU time, to converge iteratively to a solution [55]. This is due to the fact that numerical methods do not consider the traditional physics of a component or system. Therefore, design methods employing the physics of a component permit more effective designs with respect to both topology and time.

This thesis focuses on the development of appropriate circuit models and strategies for the design and prototyping of passive microwave components. The basic circuit models and optimal topologies are derived from the basic physics of a particular component. The functionality of a passive microwave component is achieved through coupling between its various segments. This interaction has been modeled as coupling between two transmission lines, two resonators or as coupling between a transmission line and a resonator. In this synthesis method, the structure of the microwave component has been divided into various forms of coupling structures, and each kind of coupling is analyzed from general coupling theory.

In this thesis, a generalized coupling theory for proximity coupling is developed which takes into account the influence of external RF fields in addition to coupling between various segments of a microwave component. All other cases of proximity coupling can be modeled as a special case of this general theory. The C- and Π-mode coupling can be analyzed by assuming zero external fields [1]. If the coupled lines are symmetric, this analysis becomes the well-known even- and odd-mode analysis. Aperture coupling theory [4] is effectively used to derive scattering parameters by considering scattered fields and field averaging over the aperture. Based on these principles, components have been designed with the goal of miniaturization and broadband performance.

By mixing stripline and microstrip technologies, a coupler has been developed which achieves both miniaturization and power handling capability. Whereas a standard proximity coupler at UHF and VHF bands yields relatively large component size due to the required quarter wavelength coupling section [14], the new design developed in this thesis reduces the component size to less than one fifth of a wavelength. The coupling between the stripline and the microstrip line is achieved through apertures in the common ground plane.

One of the important apertures in the design of couplers, filters and antenna feed systems is the cross slot. Its analysis and initial design, however, is hampered by the lack of expressions for its electric and magnetic polarizabilities [15]. In this thesis, a novel analysis and initial design concept for cross-slot couplers is presented. To facilitate a speedy design process, the measured data for the polarizabilities of the cross-slot have been curve fitted by a least squares method, and large cross-slots are analyzed by field averaging. This approach includes the effects of the orientation of the slot and allows coupling between asymmetric waveguides.

As another application in waveguide technology, a new design of single channel waveguide rotary joints for high power applications is presented. In order to obtain correct signal phase conditions along the ring and at the same time, reduce component size by reducing the diameter of the rotary joint, tapered ridged waveguide sections are introduced.

A new LTCC filter configuration is proposed. It is based on capacitively coupled elements and improves the stopband behavior of other state-of-the-art designs. Attenuation poles on either side of the passband can be achieved through source-to-load bypass coupling of two stripline impedance resonators. The simplified analysis introduced in this thesis permits the design engineer to perform a fast initial design of this class of LTCC filters.

In high-density RF circuits, it is important to estimate the influence of the discontinuities so that RF noise can be controlled [12]. In this thesis, analytical expressions for the capacitance of signal tapping pads are derived using a quasi-static analysis. A new lowpass filter design is proposed, which combines the signal tapping pads with lumped inductors.

Finally, equivalent-circuit methods are developed for electromagnetic band-gap structures formed by via-holed patches [44]. This method allows a quick design of desired pass- and stopbands and correctly predicts the first stopband, which can be used to improve the performance of printed-circuit antennas.

9.2 Future Work

The basic models and approaches developed in this thesis can be extended to a large variety of passive microwave components including antennas. They can be effectively used as building blocks in synthesis tools for the effective and quick design of individual components. Two future applications of this work will make the design process even more effective.

First, the design procedures for individual components can be combined to form subsystems. This would require the use of full-wave field solvers at a later stage and, therefore, even further reduce the time frame for component design. Application examples are diplexers or multi-band filters in LTCC technology, multi-port coupler arrangements for feed systems or multi-channel rotary joints.

Secondly, since the design procedures developed in this thesis are straightforwardly implemented as computer codes, they can be combined with commercial software packages. This will not only reduce the time to input an initial design into the commercial package, but also to immediately generate a component whose performance is extremely close to the desired specification and can be fine-tuned/optimized in only a few steps. The need for such a combination of initial design strategies and full-wave solvers has only very recently been realized. It allows the design engineer to maintain some established design practices, which are available as closed-form expressions. Moreover, it allows the design strategies developed here to be directly linked to commercially available analysis and optimization packages.

Appendix

A.1 Capacitance Between Coupled Striplines

The capacitance between coupled striplines can be estimated by even and odd mode analysis of edge coupled striplines [6].

The even and odd mode impedances of an edge-coupled stripline can be written as

$$Z_e = \frac{30\pi}{\sqrt{\varepsilon_r}} \cdot \frac{K(k_e^{'})}{K(k_e)} \tag{A.1}$$

$$Z_o = \frac{30\pi}{\sqrt{\varepsilon_r}} \cdot \frac{K(k_o^{'})}{K(k_o)} \tag{A.2}$$

where

$$k_e = \tanh\left(\frac{\pi w}{2b}\right)\tanh\left(\frac{\pi(w+s)}{2b}\right) \tag{A.3}$$

$$k_o = \tanh\left(\frac{\pi w}{2b}\right)\coth\left(\frac{\pi(w+s)}{2b}\right) \tag{A.4}$$

$$k_e^{'} = \sqrt{1-k_e^2} \tag{A.5}$$

$$k_o^{'} = \sqrt{1-k_o^2} \tag{A.6}$$

and $K(\cdot)$ is the complete elliptic integral of the first kind. The even and odd mode capacitances per unit length can be written as

$$C_e = \frac{\sqrt{\varepsilon_r}}{cZ_e} \text{ and } C_o = \frac{\sqrt{\varepsilon_r}}{cZ_o} \tag{A.7}$$

The capacitance between the coupled lines per unit length is

$$C_{12} = \frac{C_o - C_e}{2} \tag{A.8}$$

The total capacitance between the edge-coupled lines is $C_{12} l_{eq}$, where l_{eq} is the total length of the edge-coupled lines including fringing fields.

A.2 Capacitance Between Offset Coupled Lines

The coupling between the offset parallel-coupled lines can be estimated by conformal mapping analysis [35]. The technique used to determine even and odd mode impedances is an approximate one. That is, the capacitance between strip and ground is separated into parallel-plate and fringing components. The fringe capacitances can be written as

$$C_{fo} = \frac{1}{\pi}\left(\frac{2}{1+s}\right)\log\left(\frac{1+a}{a(1-q)}\right) - \frac{1}{\pi}\left(\frac{2}{1-s}\right)\log(q) \tag{A.9}$$

$$C_{fe} = \frac{1}{\pi}\left(\frac{2}{1+s}\right)\log\left(\frac{1+a}{a(1-q)}\right) - \frac{1}{\pi}\left(\frac{2}{1-s}\right)\log(q) - \frac{2}{\pi}\log\left(\frac{1+aq}{aq}\right) \tag{A.10}$$

$$q = \left(\frac{s+1}{2}\right)\left[\frac{a + \frac{2s}{s+1}}{a + \frac{s+1}{2}}\right] \tag{A.11}$$

$$w_c = \frac{s}{\pi}\log\left(\frac{q}{a}\right) + \frac{1-s}{\pi}\log\left(\frac{1-q}{1+a}\right) \tag{A.12}$$

Note that quantities *w, s, w*$_c$ are normalized here to the substrate thickness *b* (c.f. Fig. 6.6). The value of ‘a’ can be calculated from equation (A.12)

The odd and even capacitances can be written as

$$C_o = \frac{4w}{1-s^2} + C_{fo} + C_f(a=\infty) \quad \text{(A.13)}$$

$$C_e = \frac{4w}{1-s^2} + C_{fe} + C_f(a=\infty) \quad \text{(A.14)}$$

$$C_f(a=\infty) = -\frac{1}{\pi}\left(\frac{2}{1+s}\log\left(\frac{1-s}{2}\right) + \frac{2}{1-s}\log\left(\frac{1+s}{2}\right)\right) \quad \text{(A.15)}$$

The capacitance between the offset coupled lines can be written as

$$C_x = \left(\frac{C_o - C_e}{2}\right)L_{eq} \quad \text{(A.16)}$$

where L_{eq} is the total length of coupled line including fringing field width.

Bibliography

[1] V.K.Tripathi, "Asymmetric coupled transmission lines in an inhomogeneous medium", *IEEE Trans. Microwave Theory Tech.,* Vol. 23, pp. 734-739, Sep. 1975.

[2] D.M. Pozar, *Microwave Engineering*, Wiley & Sons, New York, 1997.

[3] H.A.Wheeler, "Coupling holes between resonant cavities or waveguides evaluated in terms of volume ratios", *IEEE Trans. Microwave Theory Tech.,* Vol. 7, pp. 231-244, Mar. 1964.

[4] H.A.Bethe, "Theory of diffraction by small holes", *Physical Review*, Vol. 66, pp. 163-181, Oct. 1944.

[5] D.S.James, G.R.Painchaud and W.J.R. Hoefer, "Aperture coupling between microstrip and resonant cavities", *IEEE Trans. on Microwave Theory Tech.,* Vol. 25, , pp. 392 -398, May 1977.

[6] B.C. Wadell, *Transmission Line Design Handbook.* Artech House, 1991.

[7] K. Rambabu and A.T. Kalghatgi, "Design equations for broadband planar aperture coupler", *IEEE Microwave Guided Wave Lett.,* Vol. 8, pp. 308-309, Sep. 1998.

[8] K. Rambabu and J. Bornemann, "Design of a miniaturized stripline-to-microstrip-line coupler", 2002 *IEEE MTT-S Int. Microwave Symp.* Dig., Seattle, USA, June 2002 .

[9] K. Rambabu, K.S. Keerti, M. Ramesh and A.T. Kalghatgi, "Properties of various coupling apertures", *Microwave J.,* Vol. 43, pp. 120-126, Aug. 2000.

[10] R.E. Collin, *Field Theory of Guided Waves*, IEEE Press, 2nd Ed., 1991.

[11] J.S. Rao and B.N. Das, "Analysis of asymmetric stripline by conformal mapping", *IEEE Trans. Microwave Theory Tech.,* Vol. 27, pp. 299-303, April 1979.

[12] R.K. Hoffmann, *Handbook of Microwave Integrated Circuits*, Artech House, 1987.

[13] C.G. Montgomery, R.H. Dicke, and E.M. Purcell, *Principles of Microwave Circuits*, Vol. 8, MIT Rad. Lab. Series, McGraw-Hill, New York 1948.

[14] G. Matthaei, L. Young and E.M.T. Jones, *Microwave Filters, Impedance-Matching Networks, and Coupling Structures,* Artech House, Dedham 1980.

[15] Z. Jiang and Z. Shen, “Mode-matching analysis of large aperture coupling and its application to the design of waveguide directional couplers”, *IEE Proc.-Microw. Antennas Propag.,* Vol. 150, pp. 422-428, Dec. 2003.

[16] S.D. Targonski and D.M. Pozar, “Design of wideband circularly polarized aperture-coupled microstrip antennas”, *IEEE Trans. Antennas Propagat.,* Vol. 41, pp. 214-220, Feb 1993.

[17] A.E. Williams and A.E. Atia, "Dual-mode canonical waveguide filters", IEEE Trans. Microwave Theory Tech., Vol. 25, pp.1021-1026, Dec. 1977.

[18] W.A.G Voss, “Optimized crossed slot directional coupler”, *Microwave J.,* Vol. 6, pp. 83-87, May 1963.

[19] S.B. Cohn, “Determination of aperture parameters by electrolytic-tank measurements”, *Proc. IRE,* Vol. 39, pp. 1416-1421, Nov. 1951.

[20] S.B. Cohn, “The electric polarizability of apertures of arbitrary shape”, *Proc. IRE,* Vol. 40, pp. 1069-1071, Sep. 1952.

[21] K. Rambabu and J. Bornemann, “Analysis and design of profiled multi-aperture stripline-to-microstrip couplers”, *IEE Proc.-Microw. Antennas Propag.,* Vol. 150, pp. 484-488, Dec. 2003.

[22] R.E. Collins, *Foundations of Microwave Engineering*, McGraw-Hill, New York 1966.

[23] J. Uher, J. Bornemann, U. Rosenberg, *Waveguide Components for Antenna Feed Systems: Theory and CAD*, Artech House, Norwood 1993.

[24] R. Levy, “Improved single and multiaperture waveguide coupling theory, including explanation of mutual interactions”, *IEEE Trans. Microwave Theory Tech.,* Vol. 28, pp. 331-338, Apr. 1980.

[25] S. Boronski, “A multichannel waveguide rotating joint,” *Microwave J.*, Vol. 8, pp. 102-105, Jun.1965.

[26] K. Tomiyasu and S.B. Cohn, “The Transvar directional coupler,” *Proc. IRE*, Vol.41 pp. 922-926, July 1953.

[27] G.G. Macfarlane, “Surface impedance of an infinite parallel wire grid at oblique angles of incidence,” *Proc. IEE*, Pt. A, Vol.10, pp. 1523-1527, 1946.

[28] N. Marcuvitz, *Waveguide Handbook*. New York: McGraw-Hill, 1951.

[29] M. Ramesh, K. Rambabu, and K.S. Keerti, "Analysis of displaced asymmetrical ridge waveguides", in *Proc. 31st European Microwave Conf.*, Vol. 2, pp.197-200, London, UK, 2001.

[30] K. Lim, S. Pinel, M. Davis, A. Sutono, C.-H. Lee, D. Heo, A. Obatoynbo, J. Laskar, E.M. Tantzeris amd R. Tummala, "RF-system-on-package (SOP) for wireless communications", *IEEE Microwave Mag.*, Vol. 3, pp. 88-99, Mar. 2002.

[31] EPCOS news release, "World's smallest GSM front-end module in LTCC technology", Munich, Germany, July 2001.

[32] T. Ishizaki and T. Uwano, "A stepped impedance comb-line filter fabricated by using ceramic lamination technique", in *IEEE MTT-S Int. Microwave Symp. Dig.*, pp. 617 -620, San Diego, USA, May 1994.

[33] T. Ishizaki, M. Fujita, H. Kagata, T. Uwano and H. Miyake, " A very small dielectric planar filter for portable telephones", *IEEE Trans. Microwave Theory Tech.*, Vol. 42, pp. 2017-2022, Nov. 1994.

[34] L.K. Yeung and K.-L. Wu, "A compact second order LTCC bandpass filter with two finite transmission zeros", *IEEE Trans. Microwave Theory Tech.*, Vol. 51, pp. 337-341, Feb. 2003.

[35] J.P. Shelton, "Impedance of offset parallel-coupled strip transmission lines", *IEEE Trans. Microwave Theory Tech.*, Vol. 14, pp. 7-15, Jan. 1966.

[36] A. Farrar and A.T. Adams, "Computation of lumped microstrip capacitance by matrix methods—Rectangular sections and end effect", *IEEE Trans. Microwave Theory Tech.*, Vol. 19, pp. 495-497, May 1971.

[37] P. Benedek and P. Silvester, "Equivalent capacitance for microstrip gaps and steps", *IEEE Trans. Microwave Theory Tech.*, Vol. 20, pp. 729-733, Nov. 1972.

[38] P. Silvester and P. Benedek , "Microstrip discontinuity capacitances for right-angle bends, T-junctions and crossings *IEEE Trans. Microwave Theory Tech.*, Vol. 21, pp.341-346, May 1973.

[39] V. Radisic, Y. Qian, R. Coccioli and T. Itoh, "Novel 2-D photonic band-gap structures for microstrip lines," *IEEE Microwave Guided Wave Lett.*, Vol. 8, pp. 69-71, Feb. 1998.

[40] F.R. Yang, Y. Qian, R. Coccioli and T. Itoh, "Analysis and application of PBG structures for microwave circuits," *Electromagnetics*, Vol. 19, No. 3, pp. 241-254, May-June 1999.

[41] L. Zhang and N.G. Alexopoulos, "Finite-element-based techniques for the modeling of PBG materials," *Electromagnetics*, Vol. 19, No. 3, pp. 225-240, May-June 1999.

[42] M. Rahman and M.A. Stuchly, "Transmission line – periodic circuit representation of planar microwave photonic bandgap structures," *Microwave Opt. Techn. Lett.*, Vol. 30, No. 1, pp. 15-19, July 2001.

[43] M. Rahman and M.A. Stuchly, "Circularly polarized patch antenna with periodic structure," *IEE Proc.-Microw. Antennas Propag.*, Vol. 149, No. 3, pp. 141-146, June 2002.

[44] D.F. Sievenpiper, L. Zhang, F.J. Broas, N.G. Alexopoulos and E. Yablonovitch, "High-impedance electromagnetic surfaces with a forbidden frequency band", *IEEE Trans. Microwave Theory Tech.*, Vol. 47, pp. 2059-2074, Nov. 1999.

[45] I. J. Bahl, and P. Bhartia, *Microwave Solid State Circuit Design*, John Wiley, New York, 1998.

[46] K.C. Gupta, *Microstrip Lines and Slotlines,* 2nd ed., Artech House, Boston, 1996.

[47] E. Hammerstad, and O. Jensen: "Accurate models for microstrip computer-aided design", in *1980 IEEE MTT-S Int. Microwave Symp. Dig.*, pp. 407-409, 1980.

[48] S. Amari, J. Bornemann and R. Vahldieck, "Simple rules for truncation of periodic structures to achieve a prescribed bandgap attenuation level", in *XXVIth URSI General Assembly Abstracts*, p. 39, Toronto, Canada, Aug. 1999.

[49] J. Bornemann, S. Amari, and R. Vahldieck, "A flexible CIET analysis for the design of on-axis circular waveguide components", in *Proc. 2003 Asia Pacific Microwave Conf.*, pp. 1467-1470 Seoul, Korea, Nov. 2003.

[50] J.R. James and P.S. Hall (eds), *Handbook of Microstrip Antennas*, Vol. 1, IEE Series, 1989, ch. 8.

[51] D.M. Pozar, "Input impedance and mutual coupling of rectangular microstrip antennas," *IEEE Trans. Antennas Propagat.*, Vol. 30, pp. 1191-1196, Nov. 1982.

[52] A. Tennent, High Performance Front End GPS Module, ELEC 499 Project Report, University of Victoria, Victoria, Canada, Apr. 2002.

[53] B. Veidt, "Selecting 3-D electromagnetic software", *Microwave J.*, Vol. 41, pp. 121-137, Sep. 1998.

[54] Special Issue on Electromagnetics-Based Optimization of Microwave Components and Circuits, *IEEE Trans. Microwave Theory Tech.*, Vol. 52, Jan. 2004.

[55] Automated Circuit Optimization Using Electromagnetic Simulators, Workshop Notes, *IEEE MTT-S Int. Microwave Symp.*, Boston, USA, June 2000.

[56] L.B. Gravelle and P.F. Wilson, "EMI/EMC in printed circuit boards – A literature review", *IEEE Trans. on EMC*, Vol. 34, no. 2, pp. 109-116, May 1992.

[57] Y. Matsumoto, M. Takeuchi, K. Fujii, A. Sugiura and Y. Yamanaka, "A time-domain microwave oven model for the 2.4-GHz band", *IEEE Trans. on EMC*, Vol. 45, no. 3, pp. 561-566, Aug. 2003.

[58] H. Haase and J. Nitsch, "Generalized transmission-line theory for the treatment of nonuniform multiconductor transmission lines", in *Proc. ISTET'01 XI. Int. Symp. Theoretical Elec. Engr.*, 4p., Linz, Austria, Aug. 2001.

[59] C.J. Bouwkamp, "On Bethe's theory of diffraction by small holes", Philips Research Reports, Vol.5, pp. 321-332, Oct. 1950.